ADHESION QUALITY CONTROL OF LAMINATED SAFETY GLASS USING
ULTRASONIC VELOCITY AND ATTENUATION MEASUREMENTS

BY

THOMAS ALAN SUCHY

THESIS

Submitted in partial fulfillment of the requirements
for the degree of Master of Science in Systems and Entrepreneurial Engineering
in the Graduate College of the
University of Illinois at Urbana-Champaign, 2011

Urbana, Illinois

Adviser:

Professor Henrique Reis

ABSTRACT

Laminated safety glass (LSG) specimens were prepared by Ceralink Inc. using a novel Fastfuse[TM] radio frequency (RF) lamination technology in lieu of conventional autoclaving for the final stage in the lamination process. Two groups of LSG specimens were provided for experimental ultrasonic testing (UT) with the following layup: glass/copolymer/glass. Group 1 specimens contained an automotive grade polyvinyl butyral (PVB) interlayer and float glass outer layers. Six specimens with various combinations of RF lamination time and applied pressure were prepared for Group 1. Group 2 specimens contained identical float glass as Group 1, but an architectural grade PVB interlayer with a higher stiffness was used. The RF lamination time and cooling time under a constant pressure were varied between four specimens in Group 2.

An analytical model was developed using a quasi-static spring model (QSM) to simulate guided wave behavior in LSG for different levels of adhesion. Energy velocity and attenuation dispersion curves were traced to complement experimental UT. An analytical sensitivity analysis was performed to observe the effect glass and PVB stiffness have on the guided wave behavior in LSG. Ultrasonic energy velocity and attenuation measurements were carried out to characterize material layer properties and to estimate the adhesive bond strength in each LSG specimen. Preliminary energy velocity measurements were successful at evaluating the Rayleigh velocity of the laminated specimens, which was found to be directly related to the stiffness of the glass layers.

Additional energy velocity and attenuation measurements were performed, although conclusions were somewhat limited as many assumptions were made in the analytical models about material properties and surface roughness of each laminate constituent. Energy velocity measurements from Group 1 specimens exhibited similar trends and were all estimated to hold relatively low adhesion levels of approximately pummel number 3. Destructive pummel tests were performed and revealed actual adhesion levels between pummel number 1 and pummel number 2 for all specimens. Skewed assumptions from the analytical dispersion models likely led to the overestimates in the adhesion levels predicted from energy velocity measurements.

All of Group 1 specimens exhibited similar attenuation measurements, although higher adhesion levels were predicted, between pummel number 5 and pummel number 6. In addition to assumptions made in the analytical mode, increased error in adhesion level predictions from attenuation measurements was likely associated with additional modes of energy loss and general testing setup. Energy velocity and attenuation measurements performed on Group 2 specimens predicted a slight increase in adhesion from Group 1 specimens, although definitive conclusions could not be supported, as pummel testing was not performed and material properties were not disclosed. Overall, it was encouraging to find that UT was successful at predicting similar adhesion levels for all laminates in Group 1, which was supported with pummel testing results. Additional testing is recommended on a set of laminates with higher levels of adhesion and known material properties to investigate the integrity of this UT approach further.

In general, the adhesive bond strength of each specimen from Group 1 and 2 was found to be relatively low on the pummel scale. It is believed that greater RF lamination pressure is needed to allow adequate flow characteristics in the PVB interlayer to induce proper interfacial bonding. Proper bonding will allow the adhesive bond strength to increase accordingly. Once proper lamination parameters are discovered, Fastfuse^{TM} RF lamination shows great potential for the final stage in the lamination process for LSG. Lamination time is reduced from many hours to a few minutes, and up to 95% energy savings can be expected. Additional analytical and experimental work is recommended using this technology to help characterize the adhesive bond in LSG.

To my beloved family: Hans, Susan, Adam, and Melissa

ACKNOWLEDGMENTS

I would first and foremost like to express thanks to my thesis advisor and mentor, Professor Henrique Reis, for bringing me into his laboratory and giving me all the support and opportunities for which one could ask. I appreciate all of the advice you have provided me over the past few years. You have helped me grow as an academic and as an individual.

I would also like to express thanks to Ceralink Inc. for providing specimens and funding for research. Without your support, my thesis would not have been possible.

To the members of NDTE laboratory: I will always cherish the countless hours we spent together in the lab. I am thankful for the many riveting (and humorous) conversations we shared. It has been a pleasure getting to know all of you, and I hope we keep in touch.

Adam: I am not sure how I will get any work done without you starring me down from your desk. Also, the "Wheel of blame" may have been the best work ever accomplished in the lab.

Megan: Thanks to you, my memory card is full of cat pictures, and it will always be "Friday" in my mind.

Nathan: Never forget the summer of LabVIEW! It has been a pleasure working with you, and I will likely see you in the not so distant future.

Behzad: You really are the kindest and most genuine person in the world.

Alex: "He gathered clouds…"

My academic achievements could not have been possible without the loving support of my family. I cannot thank you enough for the blessed life you have given me, and I will always appreciate the sacrifices you have made to better my life.

Finally, I would like to thank my fiancée, Melissa, for all of the love and support you have given me over the years. You have always been there to vent and talk about research and keep me well grounded.

TABLE OF CONTENTS

LIST OF FIGURES

x

LIST OF TABLES

CHAPTER 1:

INTRODUCTION TO LAMINATED SAFETY GLASS

Laminated safety glass (LSG) is a ubiquitous composite material consisting of two or more glass plates adhered together by a viscoelastic copolymer interlayer such as polyvinyl butyral (PVB) or ethylene vinyl acetate (EVA) [1]. LSG is widely used in security, architectural and automotive industries as a transparent barrier providing safety from sudden impacts by absorbing energy while preventing penetration from intruding objects [2]. In addition to providing safety from impact, LSG is used for sound reduction, ultraviolet radiation protection and solar energy control [3]. Increased load bearing capacity and impact resistance make LSG superior to monolithic glass plates with identical thickness. Additionally, the adhesive bond between the copolymer interlayer and outer glass plates of LSG reduces the risk of injury by preventing glass shards from delaminating upon fracture. The performance of LSG is largely affected and controlled by the level of adhesion between the glass plates and copolymer interlayer [4]. When a laminate is struck by an external load, the copolymer interlayer absorbs kinetic energy through elastic deformation and transfers shear stresses between the outer glass plates [5]. Laminates with very high adhesion do not allow the copolymer interlayer to transfer shear stresses effectively, which reduces the impact resistance considerably. Therefore, laminates with too high adhesion act as monolithic glass plates when impacted by an external load. Conversely, when laminates with very low adhesion are impacted, large shards of glass are delaminated from the copolymer interlayer, resulting in high risk of injury [6]. As a result, it is imperative to find an optimal level of adhesion that will observe higher impact energy levels, while preventing large delaminations of fractured glass. The general tradeoff between impact resistance and adhesive bond strength in LSG is illustrated in Figure 1.1.
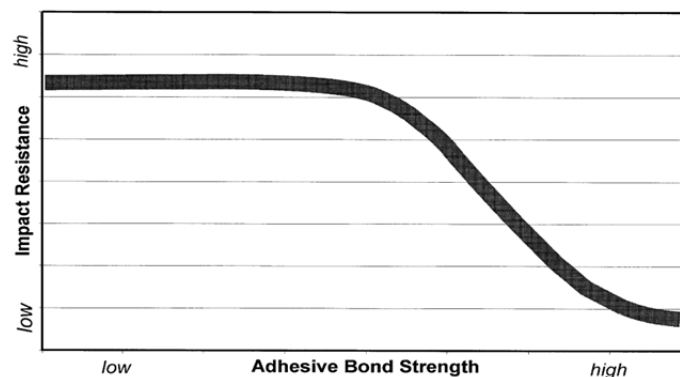
Figure 1.1: Relationship between impact resistance and adhesive bond strength in LSG. Figure extracted from [4].

In order to control and evaluate the adhesive bond within LSG, it is necessary to understand the surface characteristics and the intermolecular forces at the interface of the glass and copolymer interlayer. The topography of each LSG constituent (i.e. glass and copolymer) surface is rough on the microscale and characterized in terms of peaks and valleys, which presents non-uniform regions of contact at the interfaces. The adhesive bond strength is directly related to the amount of contacting regions at the interface of two surfaces [4, 7-10]. In addition to the surface topography and interfacial forces between glass and copolymer, the level of adhesion of LSG depends on many lamination processing variables such as pressure, time, heat, moisture content, and alkalinity [4, 11-14].

It is difficult to explicitly characterize the adhesion level in LSG since the adhesive bond is dependent on several material properties and lamina dimensions of both glass and copolymer layers. In addition, numerous variables exist in the lamination process, which are catered toward specific LSG applications. As a result, the adhesive bond in LSG can be very complex and variable. Over the span of the last century, many techniques have been used to describe the adhesive bond in LSG, although none are exclusively utilized. Destructive testing methods such as the pummel, compressive shear strength, peel, and tension tests are currently used, although limited quantitative data is extracted and results from each testing method are not directly comparable. Additionally, a certain percentage of specimens are damaged and wasted for each test. Therefore, an efficient and inexpensive method for determining the adhesive bond strength in LSG is essential to industry. As a result, a number of nondestructive testing (NDT) methods have been investigated to help characterize the integrity and adhesive bond in LSG without damaging any specimens. The most successful NDT methods use ultrasonic testing (UT) to describe the adhesive bond strength in LSG [15-18].

In Chapter 4, NDT UT is used to investigate the effectiveness of a novel Fastfuse[TM] RF lamination technology and to characterize the adhesive bond strength in LSG specimens. Automotive grade and architectural grade LSG specimens were provided by Ceralink Inc. for experimental energy velocity and attenuation UT measurements. A PVB film was sandwiched between standard float glass plates for each specimen group and will be the copolymer interlayer of concentration herein.

1.1   ADHESIVE BOND

The interfacial adhesive bond that unites glass and PVB surfaces is characterized by analyzing the surface topography of each LSG constituent and the intermolecular forces that bond the composite laminate. PVB film used in LSG has a very rough surface which is described by regions of peaks and valleys known as asperities [7]. Although glass surfaces appear very smooth to the naked eye, they are actually rough on the nanoscale and characterized similarly. The contact region between PVB and glass is variable due to surface texture, which affects the interfacial adhesive forces and bond of LSG [19]. An illustration of the surface roughness and bonds between glass and PVB is shown in Figure 1.2. In general, the adhesive bond strength goes down as surface roughness goes up [8, 9]. Consequently, surface topography and contact regions play a large role in the adhesive bond between two laminas. Various techniques characterizing surface roughness as well as the different types of intermolecular forces present at the interface of two surfaces are described in the following sections.
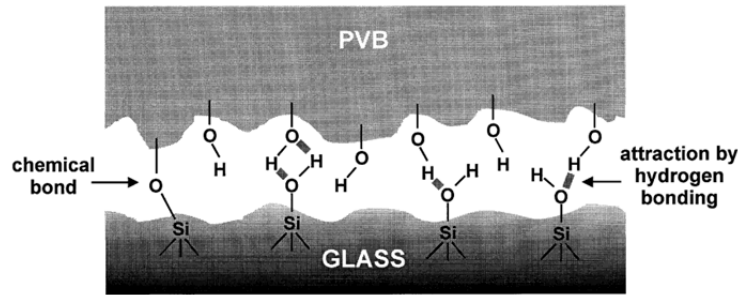
Figure 1.2: Illustration of surface roughness and intermolecular bonding at glass and PVB interface. Figure extracted from [4].

1.1.1   SURFACE CHARACTERIZATION

Material surface profiles are usually described in terms of roughness, waviness and error of form or lay [20], which are illustrated in Figure 1.3. Surface roughness is defined as closely spaced irregularities in height and width, attributed to material features intrinsic to production processes. Surface waviness is attributed to irregularities with greater spacing than defined for roughness and is usually a product of machining, heat treatment, or warping. Errors of form are described by gross deviations from the expected, or nominal, shape. Surface waviness and errors of form for plate glass and PVB film used in LSG are neglected for the purpose of this paper. Therefore, the surface profile of each LSG constituent is characterized by the surface roughness only. For further details on surface topography the reader is referred to Grzesik [21].

3
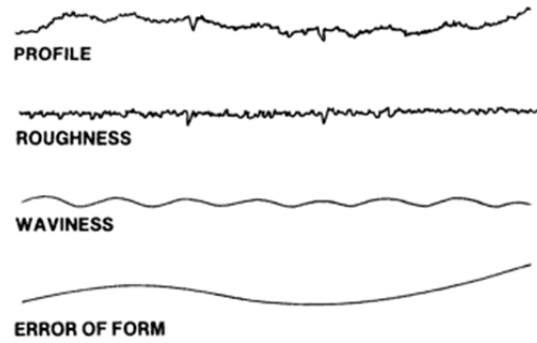
Figure 1.3: Three main components of surface texture: roughness, waviness and error of form. Figure extracted from [20].

Three methods commonly used to quantify material surface roughness include interferometer, stylus profilometer and atomic force microscopy (AFM) measurements, which are described herein. Profilometer and AFM measurements have been successfully employed by Huo [10] to help characterize float glass and PVB film surface roughness in LSG specimens. Surface roughness for float glass and PVB were characterized on the nanoscale and microscale, respectively. Resulting measurements are used to develop an analytical dispersion model in Chapter 3.

Many additional methods exist that help characterize topography of material surfaces such as X-ray photoemission spectroscopy (XPS), Auger electron spectroscopy (AES), dynamic secondary ion mass spectrometry (SIMS), energy dispersive X-ray fluorescence (EDAX) and hydrogen profiling by nuclear micro-analysis (NMA), although these methods are not commonly used on LSG. For a detailed description of these methods reference Lausmaa and Kasemo [22], where each technique was used to characterize titanium implant surface topography.

1.1.1.1 INTERFEROMETER

One of the most practical optical surface profilers is the (Michelson) interferometer, which does not require any surface contact and is able to scan a large surface area very quickly [23]. Furthermore, surface roughness can be measured down to the nanoscale with great precision. A simplified schematic of a typical interferometer is shown in Figure 1.4. Broad-bandwidth light is directed toward a half-silvered mirror set at a 45° angle and split into two paths. Path 1 is reflected from the test specimen surface and interferes with path 2, which is reflected from a reference mirror. Both paths recombine and produce an interference pattern that is collected by a

photodetector. Reflections from surface asperities cause phase shifts between the two light paths. The surface roughness (height) profile is characterized by differences in the fringe pattern of light and dark lines resulting from optical wave interference. Three-dimensional images can be created by constructing successive imaging arrays across a specimen surface. Although this method has many advantages in characterizing surface roughness, one should note that resulting measurements become increasingly inaccurate for surface roughness greater than 1.5 mm [24].
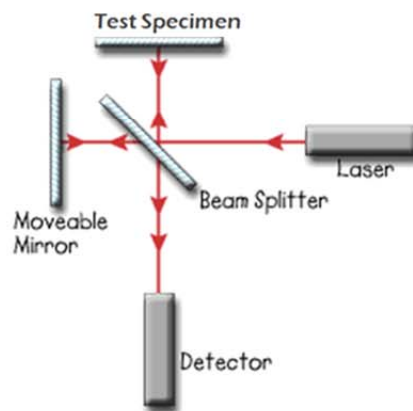
Figure 1.4: Schematic diagram of Michelson interferometer used for surface texture characterization. Figure extracted from [25].

1.1.1.2 STYLUS PROFILOMETER

A surface profilometer, or stylus profiler, is one of the most widely used contact measurement tools for characterizing surface roughness and analyzing surface topography [24]. A conventional stylus profilometer is presented in Figure 1.5.
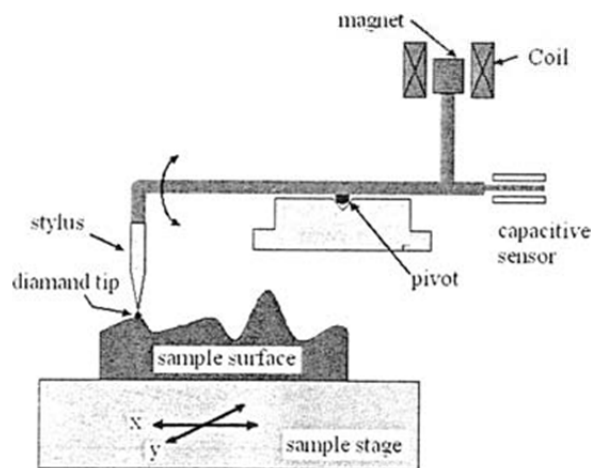
Figure 1.5: Schematic diagram of conventional stylus profilometer and sample testing setup for surface texture characterization. Figure extracted from [26].

Profilometer measurements are taken by dragging a diamond stylus with a radius of a few micrometers across a material surface with a load on the order of millinewton. The resulting vertical displacement of the stylus is recorded by a linear variable differential transducer. Vertical resolution varies from the microscale to the nanoscale, depending on the radius of the diamond stylus. Almost any material surface can be analyzed using a two-dimensional scan. To obtain a three-dimensional profile of a material surface, multiple parallel profilometer measurements are required. Therefore, this method is relatively more time intensive than optical profilers.

1.1.1.3 ATOMIC FORCE MICROSCOPY

Atomic force microscopy (AFM) is a very robust contact surface profiler that uses a high-resolution scanning microscope [9]. AFM measures the force of interaction between an extremely fine point ceramic or semiconductor tip and a specimen surface. A typical arrangement of an AFM setup is displayed in Figure 1.6. The tip is generally around $1 - 2$ μm in length with a diameter less than 10 nm and is located on the free end of a cantilever beam approximately 100 - 200 mm in length [24]. As the tip is scanned over a specimen and comes within a few angstroms of the specimen surface, repulsive van der Waals forces result, causing the ceramic tip to deflect upward. A laser light source is concentrated on a mirror at the tip of the cantilever beam, and the reflected light is measured by a position sensitive photodetector, creating a three-dimensional topographic surface profile. AFM is advantageous over other mechanical contact surface profilers given that the vertical surface roughness can be described with great precision on the nanoscale.
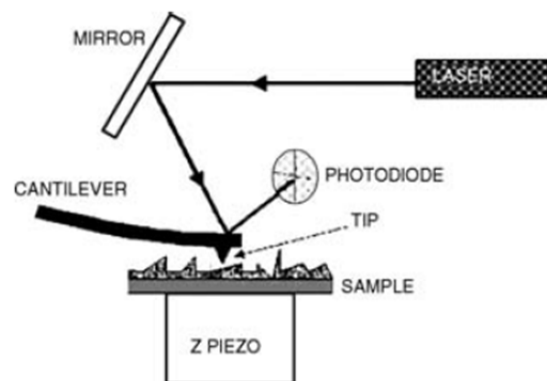
Figure 1.6: Schematic diagram of AFM testing equipment and setup used for surface texture characterization. Figure extracted from [27].

1.1.2   INTERFACIAL ADHESIVE FORCES

The adhesive bond in LSG is dependent on a variety of interfacial forces, including capillary/meniscus, van der Waals, electrostatic, and chemical bond [8, 9, and 28]. Additionally, the contact region between adjoining surfaces affects the adhesive bond due to random surface asperities. Figure 1.7 exemplifies the contact region as well as the intermolecular forces present at the interface of two surfaces.
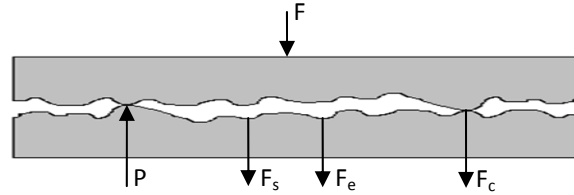
Figure 1.7: Intermolecular forces and contact asperities at the interface of two surfaces.

Under static loading, the resultant external force due to interfacial forces is found as follows,

$$F = P - F_s - F_e \dots\dots\dots\dots\dots\dots\dots\dots\dots\dots\dots\dots\dots\dots\dots\dots\dots\dots\dots\dots\dots(1.1)$$

where P is the asperity contact load, F_s are the intermolecular adhesive forces, and F_e are the electrostatic forces. Notice that the capillary forces are absent from Equation 1.1, as menisci do not form between asperities [8]. Adhesion exists when the attractive forces exceed the asperity contact load, which results in a negative external force, F. A brief description of the intermolecular forces present at the interface between two surfaces is provided in the following sections. In Chapter 3, micromechanical models and fracture mechanics principles are used to model the contact regions at the glass and PVB interface for LSG.

1.1.2.1 CAPILLARY/MENISCUS

The most dominant intermolecular adhesive force bonding two surfaces is believed to be capillary, or meniscus, force [9]. Meniscus forces arise from Laplace pressure differentials in trapped capillary liquid passages, which exert a surface tension force between contacting asperities. Excess moisture and high humidity environments lead to greater forces [8]. Due to the hygroscopic nature of PVB, meniscus forces are believed to be present in LSG at the glass and PVB interface. A novel meniscus surface model has been developed by Xue and Polycarpou [29] to characterize the capillary adhesive forces in microelectromechanical systems (MEMS). A similar model was developed by Tayebi and Polycarpou [8] that introduced surface roughness effects.

1.1.2.2 VAN DER WAALS

Usually a relatively weak force, van der Waals forces exist between all electrically neutral, polar and non-polar molecules. Originally derived from quantum mechanics principles by Fritz London [30], the attractive forces manifest from permanent electric dipoles. Due to this fixed distortion in electric distribution, time-varying (instantaneous) dipoles polarize neighboring atoms causing a dipole moment resulting in attractive forces. When the polarity between two neighboring atoms coincides, the total energy is at a minimum creating a van der Waals force. Note that van der Waals forces are present at all contacting surfaces since the instantaneous dipole moment exists in polar and non-polar atoms, while surface roughness and material properties dictate the strength of a force [28]. A special case of van der Waals force occurs when hydrogen atoms from one molecule interact with electronegative atoms of a different molecule, producing a stronger intermolecular bond. Electronegative atoms acquire electrons from the hydrogen atom, which produces an abnormally strong dipole-dipole attraction between hydrogen and other electronegative atoms [30]. Hydrogen bonds exist in LSG due to the highly polar molecular groups of each constituent. PVB is a copolymer consisting of a non-polar butyral group and a polar vinyl alcohol group, while glass consists of a polar silanol group. When the highly polar groups of PVB and glass are brought into close contact, hydrogen bonds form at the interface [4].

1.1.2.3 ELECTROSTATIC

Electrostatic forces develop from externally applied voltages across surface interfaces and/or when adjoining surfaces hold a certain electric charge causing an electric field across the interface [8]. Electrostatic forces are subdivided into two main categories described by the type of attraction. The electrostatic *image* force is dependent on particle size and follows classical Coulombic attraction. The other electrostatic force is the *electrical double layer* force, which tends to outweigh the electrostatic image force in multilayered systems. An interfacial contact potential arises between two dissimilar materials in close proximity to one another. The internal contact potential and the externally applied voltage are additive and create increased electric fields across multiple interfaces [28]. If the electric field across the interface of two surfaces is removed, electrostatic forces will diminish in time. Therefore, electrostatic forces are not likely present in LSG, as an absence of electric field across the glass/PVB interface exists.

1.1.2.4 CHEMICAL BOND

When a highly polar silanol group (e.g. glass) comes into close enough proximity with a similarly behaving vinyl alcohol group (e.g. PVB), a strong chemical bond emerges. Surface roughness plays a major role on whether the chemical bond will exist, where even relatively small surface asperities limit the chances for chemical bonding [4]. Consequently, surface asperities must be abridged to form a chemical bond between PVB and glass in LSG. As a result, specialized lamination processes are involved to eliminate excess asperities on the PVB surface, which are covered in the following sections.

1.2   LAMINATION PROCESS FOR LAMINATED SAFETY GLASS

The performance of LSG is based on a number of factors including the type and thickness of glass plates and copolymer interlayer as well as an assortment of lamination processing variables [4, 11-14]. An overview of a conventional lamination process used for LSG is briefly presented, followed by a description of a novel Fastfuse[TM] lamination technique using radio frequency (RF) waves. Details of specific lamination processing variables are elaborated on, as they play major roles in the adhesive bond strength in LSG.

1.2.1   CONVENTIONAL AUTOCLAVE LAMINATION

The first step in the lamination process of LSG is selecting the appropriate type of glass and copolymer interlayer for a specific application. Soda-lime glass is the most prevalent type of glass used for LSG products. Float glass is a special type of soda-lime glass that is produced by molding molten glass on top of molten tin, resulting in an extremely uniform and flat glass surface. A few different types of copolymer interlayers are commonly used in LSG. For applications requiring very high impact resistance (i.e. security, automotive and architectural applications), the most common copolymer interlayer used is PVB [31]. Over 90% of LSG products use a PVB interlayer due to its high toughness, tensile strength and modulus of elasticity [4]. Other types of copolymer interlayers include EVA and polyvinyl urethane (PU), which are more commonly used in the solar industry and for sound reduction [32]. LSG specimens provided for experimental testing contain standard float glass plates and PVB interlayers. Therefore for the remainder of this paper, float glass and PVB will be used to describe the outer glass plates and copolymer interlayer of LSG, respectively.

The Folio lamination process is most extensively used conventional lamination technique for LSG that uses a viscoelastic copolymer film for the interlayer. Four main stages in the lamination process are universally followed: glass and film preparation, assembly, deairing, and autoclaving under heat and pressure [1]. Glass preparation starts by forming and cutting proper dimensions, followed by a prelamination wash to eliminate all contaminants from the surface. The PVB film is stretched and cut to specified widths, and prewashed similarly to the glass. Large rolls of PVB film are wound and stored for lamination. The two LSG constituents are then assembled in a clean room by rolling the PVB film onto one glass plate. After the PVB is sandwiched with another glass plate, a deairing process is commenced to remove any air between the PVB and glass. All deairing processes use a combination of heat and pressure to eliminate trapped air and create an initial adhesive bond. Once the deairing process is complete, the laminate is put in an autoclave for the final lamination stage. In order to obtain the chemical bond described in the preceding section, the laminate is heated and pressurized sufficiently to allow the PVB film to flow and fill microscopic glass surface asperities. Assuming all other lamination variables are adequate, the general correlation between lamination temperature and adhesive bond strength (measured using compressive shear strength tests) is shown in Figure 1.8. Typical target temperatures range from 130 - 150 $^{\circ}$C, and sufficient pressure is recommended between 12 - 15 bar (174 - 218 psi) [33]. For a detailed description of conventional lamination processes, the reader is referred to Savineau and U.S. patent 7,704,342 B2 [1, 2].
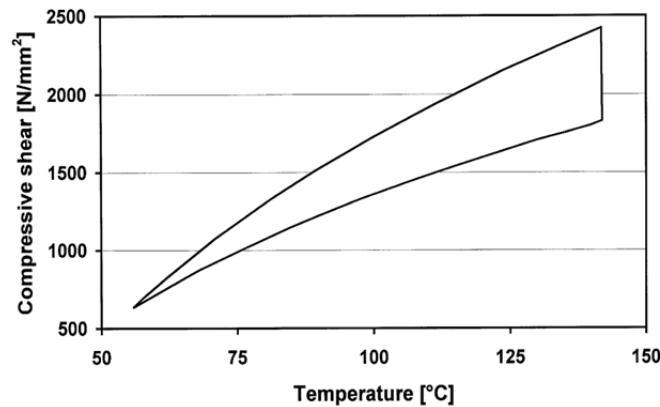
Figure 1.8: General correlation between lamination temperature and adhesive bond strength in LSG. Figure extracted from [4].

1.2.2 FASTFUSE[TM] LAMINATION

In 2006, Ceralink Inc. invented a novel Fastfuse[TM] lamination technology that uses RF microwaves to heat the copolymer interlayer in LSG in lieu of the final autoclaving stage used in conventional lamination processes. Glass/film preparation, assembly and deairing procedures are carried out similarly to conventional lamination methods. Then, Fastfuse[TM] technology uses RF energy to heat PVB film, while applying adequate pressure to the laminate, until proper flow characteristics are achieved. Fastfuse[TM] RF lamination reduces lamination time from hours to minutes, while providing 95% energy savings compared to conventional autoclaving [34]. LSG specimens using the novel Fastfuse[TM] RF lamination technology were provided by Ceralink Inc. for experimental UT, which is covered in Chapter 4.

1.2.3 LAMINATION PROCESSING VARIABLES

Many variables exist in the lamination process of LSG that affect the adhesive bond between glass plates and the PVB interlayer. Two lamination variables that heavily influence the adhesive bond in LSG are moisture content of the PVB film and water quality in the prelamination washing process [11]. The reader is referred to [1, 2, 33, 35, 36] for additional lamination factors and environmental effects contributing to variations in the adhesive bond strength of LSG.

PVB is hygroscopic material due to the highly polar vinyl alcohol groups of which it is comprised. As a result, PVB is not only attracted to the highly polar silanol groups of float glass but also the highly polar water compound. Therefore, PVB and water molecules compete for available bonding sites on the glass surface [12]. The general affect water content has on the adhesive bond strength in LSG is shown in Figure 1.9.
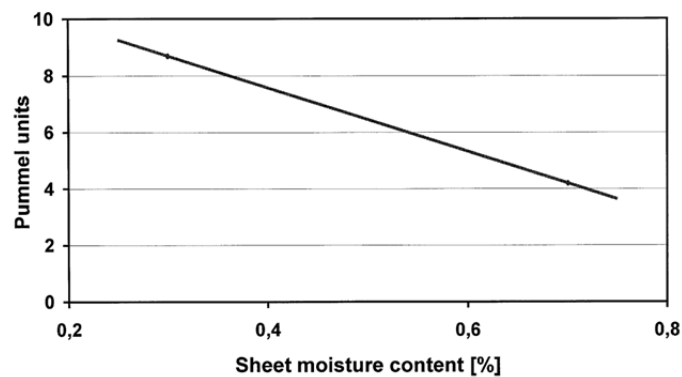
Figure 1.9: General relationship between adhesive bond strength and sheet moisture content in LSG. Figure extracted from [4].

Since PVB must go through a prelamination washing cycle, sheet moisture content can reach levels up to 2%. Consequently, the PVB film must go through a thorough drying stage to reach the desired moisture content of 0.3 - 0.5% moisture content [13]. Additionally, edges of laminated specimens must be sealed upon lamination to reduce moisture ingression from high relative humidity environments. A correlation between relative humidity and sheet moisture content is provided in Figure 1.10.
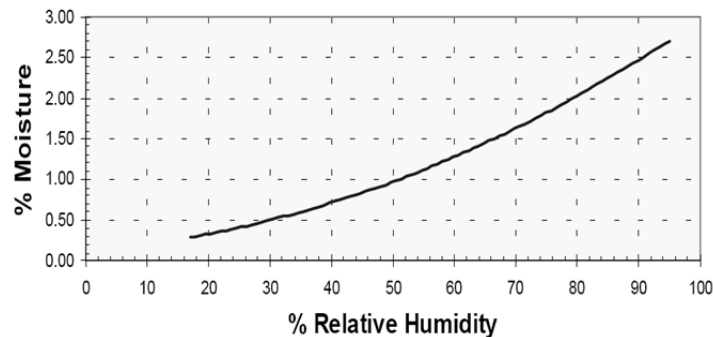
Figure 1.10: General relationship between sheet moisture content and relative humidity in LSG with typical PVB interlayer. Figure extracted from [13].

In addition to monitoring the amount of moisture in the PVB film, the water quality used in the prelamination wash process is also of importance. Intermolecular bonding between glass and PVB can be significantly influenced by residual salts leftover from the wash process. Ionic particles attract water molecules creating higher moisture at the glass/PVB interface [4]. Figure 1.11 exhibits the tendency of the adhesive bond to diminish with increased alkalinity, or conductivity. Therefore, distilled water is generally used in the prewash process. Refer to Huntsberger [14] for a detailed parametric experimental study on the influence of adhesion lowering salts and diffusion of water on the adhesive bond strength of LSG.
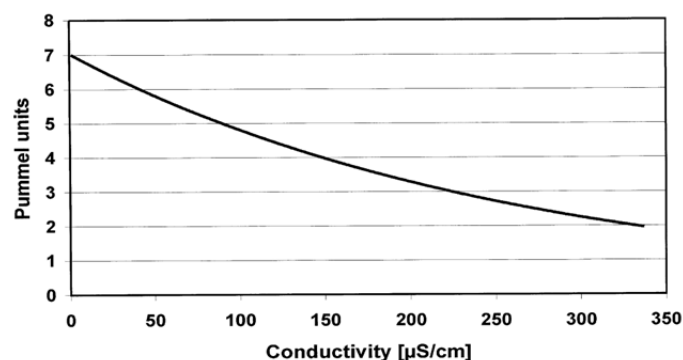
Figure 1.11: General relationship between adhesive bond strength and conductivity of water used in prelamination washing process of LSG. Figure extracted from [4].

12

1.3 ADHESION TESTING METHODS FOR LAMINATED SAFETY GLASS

As discussed in preceding sections, the adhesive bond strength in LSG is highly dependent on intermolecular forces and contacting asperities at the glass/PVB interface as well as specific lamination processing variables. Furthermore, the overall performance of LSG is largely affected by the strength of the adhesive bond between laminas. As a result, some basic destructive testing methods have been developed to help characterize the adhesive bond between glass and PVB. In addition, many nondestructive testing (NDT) techniques have been investigated and show potential for adhesion level monitoring for adhesively bonded joints such as LSG.

1.3.1 DESTRUCTIVE TESTING METHODS

The adhesive bond strength in LSG is currently evaluated using a small number of destructive testing methods such as the pummel test, compressive shear strength test, peel test, and tension test [4, 11, 37, 38]. Although each technique exhibits unique benefits (as well as drawbacks), the LSG industry has not settled on one standardized testing method. Generally speaking, multiple tests are performed with one or more methods to ensure adequate information is provided about the adhesion level of LSG. Inherent drawbacks common to each method include cumbersome testing procedures/analyses in addition to the destruction of a certain percentage of specimens. Consequently, superfluous specimens are manufactured and wasted, costing the LSG industries significant time and money.

Perhaps the most extensively used method for characterizing the adhesive bond in LSG is the pummel test. The pummel test is carried out by positioning a LSG sample on a steel plate and cooling it to -18 ^{o}C. Generally, a one pound hammer is used to strike the sample [4]. The amount of glass remaining intact with the PVB interlayer dictates the strength of the adhesive bond. Pummel test results are visually analyzed and rated on an arbitrary scale from 1 to 10, which has been defined by the LSG industry [11]. Results are moderately subjective and vary from operator to operator. Therefore, additional tests are usually used to supplement pummel test results.

Another widely used destructive method is the compressive shear strength (CSS) test. A general testing setup for the CSS test is displayed in Figure 1.12. A LSG specimen is placed at a 45$^\text{o}$ angle and exposed to a vertical compressive load. The holding fixture is arranged on spherical supports to ensure absolute vertical loading [37]. The compressive load is increased until failure occurs at the glass/PVB interface. The resulting failure load is used to quantify the adhesive bond strength of LSG. Although CSS tests provide more objective data than pummel tests, results are highly dependent on laminate thickness and material properties.
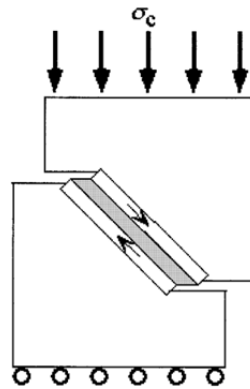
Figure 1.12: Schematic diagram of compressive shear strength test used to quantify the adhesive bond strength in LSG. Figure extracted from [37].

A general relationship between the pummel scale and CSS data for similar specimens is provided in Figure 1.13 [4]. Note that this is only a general trend and cannot be used to correlate results between testing methods.
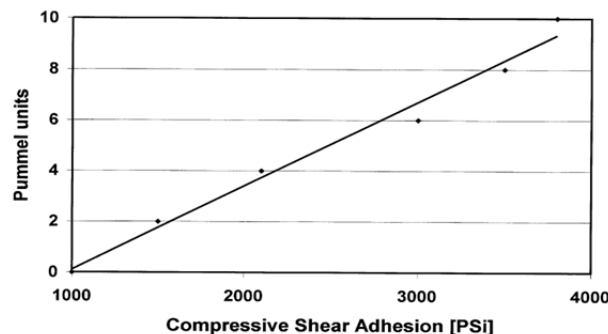
Figure 1.13: General relationship between pummel scale and CSS data from adhesive bond strength measurement in LSG. Figure extracted from [4].

The destructive peel test is also used quite often to characterize the adhesive bond in LSG. Special laminate samples are prepared with a PVB layer sandwiched between one glass plate and a thin metal sheet. The PVB interlayer is then peeled away from the glass plate at a 90$^\text{o}$ angle [14]. The adhesive bond strength is correlated to the average force per unit width required to peel

14

the PVB interlayer away from the glass layer. Peel test results are difficult to relate directly to adhesive bond strength since the mechanism of failure is not comparable [38]. Therefore, peel test data is used qualitatively along with empirical results from supplementary testing. Similarly to the CSS tests, resulting data is also relative to the dimensions and material properties of the glass and PVB layers.

Tension adhesion tests have been used to obtain quantitative data on the adhesive bond strength of LSG and are often used to supplement pummel and peel tests [38]. Typical LSG samples are used with small cracks in both glass plates along the width of the laminate as seen in Figure 1.14. A tensile load is applied to the laminate and the displacement rate is monitored. Resulting load-displacement curves can be related to supplementary results to obtain empirical data on the adhesive bond strength. The dimensions of the glass and PVB layers used for the tension test considerably affect the resulting load-displacement curve in tension tests. Therefore, quantitative data is difficult to standardize directly.
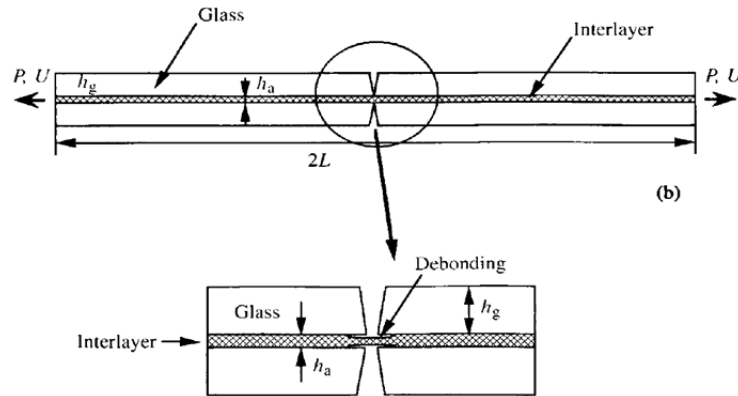
Figure 1.14: (a) Typical testing setup for tension adhesion test used to describe the adhesive bond strength in LSG, and (b) region of debonding resulting from tension adhesion test. Figure extracted from [38].

1.3.2 NONDESTRUCTIVE TESTING METHODS

In recent years, modern computing technology has enabled many nondestructive testing (NDT) methods to become increasingly efficient as a whole, as specimens are not damaged and testing procedures can be less time intensive than standardized destructive testing methods. The most widely investigated nondestructive testing method for evaluating the strength of adhesively bonded joints is ultrasonic testing (UT), although a standardized method has not yet been adopted [15-18]. Research on adhesive lap joints and bonds with metal/metal and metal/composite interfaces has been the major focus to date. A variety of UT techniques have

been considered, although methods that have shown most potential for evaluating adhesive bond strength use ultrasonic velocity and attenuation measurements with standard pulse-echo or pitch-catch arrangements. Recently, similar UT methods have been applied to assess the adhesive bond strength in LSG. Fundamental UT principles are described in Appendix A, while the reader is referred to [39] for an extensive literature review on various ultrasonic velocity and attenuation measurement techniques. A review of past work on the nondestructive evaluation of adhesive bond strength in laminated systems is presented herein. For information on general NDT UT methods using guided waves for prospective material characterization in plate-like structures, please see the following references: [15, 40-43]. Additionally, Chimenti [44] describes analytical and experimental work using guided plate waves for material characterization, along with a detailed literature review of related research and NDT methods.

UT is a broad field of NDT that uses guided mechanical stress waves and modern signal processing to inspect adhesive joints. Pulse-echo and through transmission arrangements have been successful at monitoring reflections from layer boundaries and imperfect interfaces [15-17, 19, 45-53]. Delaminations in adhesive bonds are determined by observing relatively large reflected (received) signal amplitudes resulting from vast differences in acoustic impedance between air and solid substrate [15].

Lavrentyev and Rokhlin [45] used a typical pulse-echo UT technique to assess the imperfect interface between two aluminum blocks with an aluminum substrate by analyzing reflected signals in the frequency domain via fast Fourier transform (FFT). Since the properties of all aluminum components were identical, impedance differences were eliminated, and resulting frequency shifts were attributed to variances in interfacial stiffness. Tattersall [46] reported inconclusive results regarding conventional pulse-echo UT for adhesive bond strength detection, as perfect and imperfect interfaces reflected ultrasonic waves similarly. Therefore, a novel technique was investigated using both amplitude and phase of the reflected signals. Gaseous contaminants (adverse product of lamination process) embedded in an adhesive polyethylene layer between aluminum alloy plates were described by increased reflected amplitudes and phase variations. Wooh and Wei [47] used a modified pulse-echo technique to sharpen the resolution for time domain signal analysis.

Oblique incidence UT has also been extensively used with a through transmission arrangement, where both sending and receiving transducers are located on the same side of the testing surface. This method is advantageous for thin plates and layered systems such as adhesive joints since reflected signals and multiple wave modes become separated in space as well as time [15]. Additionally, oblique incidence UT is believed to be more sensitive towards interfacial bond weakness [16, 48-52]. Pilarski and Rose [48] demonstrated an increased sensitivity for adhesive bond strength characterization using oblique incident transverse ultrasonic waves. Aluminum/epoxy joints were inspected with weak and strong bonds, and the reflected waves from the interfacial boundary were analyzed. Analytical and experimental values correctly predicted the bonding condition in each study. Pilarski et al [49] performed a follow-up study using a similar technique, and results were confirmed. Roklin and Marom [50] investigated the effect of solid/solid, rigid, and slip boundary conditions for adhesively bonded interfaces. Resulting amplitudes were found to be related to the strength of the joint, and the method showed potential for monitoring the adhesive curing process. Similar results were obtained on aluminum/epoxy joints by Pialucha [16]. Sun [51] demonstrated this technique on adhesively bonded aluminum plates using a variable surface damper to describe resonant frequencies over debonded areas. Delaminations were detected from variances in the resonant frequency as the damper was applied. Santos and Faia [54] used oblique incidence with immersion transducers at various incident angles on adhesive lap joints. Resulting attenuation was compared with that of a single plate specimen and to theoretical dispersion curves to observe any variances. Dominant wave modes were successfully evaluated by correlating attenuation and the presence of bond or disbond. Contrary to results discovered from [16, 48-52], Cawley and Kinloch [53] reported constructive correlations between velocity and attenuation measurements and amount of disbond at aluminum/epoxy interfaces for both normal and oblique incident UT setups, where normal incident results exhibited greater energy and better resolution than oblique incidence.

Additional NDT UT techniques have been used to evaluate adhesive bond strengths, but the amount of research performed is more limited. A technique using a laser to generate ultrasonic waves has been investigated by Heller et al [55]. 2-D FFT data were used to characterize the adhesive bond between aluminum plates. Resulting behavior was consistent with analytical spring models developed to simulate guided wave behavior in laminated specimens.

Acoustic isolation values of LSG have been successfully predicted by Baenas et al [56], using simulated models of impedance coupling between glass and polymer interlayer. Results were somewhat limited as many inputs were estimated for the given simulations.

Another NDT technique derived from typical UT testing techniques was developed for more robust signal analysis. The acousto-ultrasonic (AU) method measures variations in stress wave propagation to assess mechanical properties of materials and laminated systems such as adhesively bonded joints [40, 57-61]. Broad-band ultrasonic pulses are used to excite an array of frequencies, which travel through a specimen and are received similarly as acoustic emission sensors. A multitude of stress wave factors can be extracted to characterize the received AU signal, giving AU testing certain advantages over standard UT such as analysis of rise-time, signal strength and ring down counts [40, 57]. Refer to Vary [62] for a detailed description of the AU approach.

A concise overview of the AU approach is provided by Reis and Vary [40] in addition to an experimental investigation using a through transmission, obliquely incident AU technique to assess porosity levels in advanced polymer composites. Correlations between preferred SWF measurements (power spectral density) and actual porosity levels were in good agreement. Lower SWF measurements corresponded to higher porosity, as significant energy loss was associated with stress wave scattering and leakage from increased voids (porosity). Using a through transmission AU approach, Wegman [57] empirically derived a relationship between AU stress waves and the adhesive bond strength in metal-to-metal bonded joints. The average AU signal strength was compared to destructive peel strength tests on identical specimens. Lower AU signal strength corresponded to higher average peel strength values, which was attributed to more energy being absorbed by the attenuative bond layer. Similar techniques were demonstrated on adhesively bonded lap joints by the following authors: [58-60]. The adhesive bond strength between rubber and steel plates was evaluated by Reis and Krautz [61] using two stress wave factor (SWF) approaches. Each SWF was related to the signal energy in either the time or frequency domain. Specimens with various levels of adhesion were evaluated and compared to peel test specimen data. Increases in SWF corresponded to increases in adhesion.

Overall, a large assortment of NDT UT techniques has been investigated for assessing the strength of adhesively bonded joints, showing potential for further investigation. Due to previous success using oblique incident UT experimental setups, a few authors [10, 16, 19, 63] have applied this technique on LSG specimens. Pialucha [16] monitored the reflection coefficient from normal and oblique incident ultrasonic waves at glass/epoxy interfaces to assess curing age of the interfacial bond. Normal incident measurements were unable to discern variations in interfacial bond age, while certain oblique angles were very sensitive to small interfacial changes at the interface of glass and epoxy. Hou and Reis [10, 19, 63] used ultrasonic guided wave energy velocity and attenuation measurements in accordance with an analytical spring model to assess the adhesive bond strength in LSG. LSG specimens with various levels of adhesion were inspected with NDT UT and destructive pummel testing. Measurements of one particular partial wave mode at an appropriate frequency were compared to a dispersion model simulating guided wave behavior in LSG. Higher energy velocity measurements corresponded to lower laminate adhesion, while higher attenuation measurements corresponded to higher laminate adhesion. Comparisons between predicted adhesion levels and pummel test results were in good agreement, showing potential for UT as a method for evaluating adhesive bond strength in LSG.

Additionally, David and Wittberg [64] used electron spectroscopy for chemical analyses (ESCA) to estimate the adhesive bond in LSG. The thickness of a residual PVB layer left of the glass surface post peel test was directly proportional to the adhesive bond strength.

The adhesive bond strength in LSG was evaluated using the AU approach in two separate studies by Chica [65] and Slowinski [66]. The AU approach showed good potential in each study by correlating calculated stress wave parameters with adhesive bond strengths. Results were confirmed with destructive pummel tests. Reis and Chung [67] investigated the effectiveness of the AU approach for online quality control estimates of the adhesive bond strength of LSG. Specific AU wave parameters, deemed stress wave factors, were extracted and related to adhesive bond strengths with up to 95% confidence.

CHAPTER 2:

GUIDED WAVE PROPAGATION IN THIN PLATES

It is important to understand the fundamental properties of acoustic wave propagation before introducing the concept of guided acoustic waves in thin plates. Therefore, it is necessary to begin by introducing bulk wave propagation in solid media, which refers to wave propagation in an infinite elastic solid material [68]. Geometrical constraints are then imposed on solid media to introduce the concept of dispersion and guided wave behavior in thin plates. All material layers are assumed isotropic for the purpose of this paper.

2.1   WAVE PROPAGATION IN INFINITE ELASTIC SOLID MEDIA

Acoustic waves are described by time-varying deformations or vibrations between neighboring particles. Assuming that all displacements are continuous in the direction of propagation, solid materials are able to support longitudinal and shear bulk wave modes. Longitudinal wave mode particles oscillate in the same direction as the propagated wave. They are also referred to as compressional waves because the oscillating particles move about their equilibrium through sequences of compression and rarefaction, where the medium experiences only a volume change. Conversely, shear wave mode particles oscillate transversely to the direction of propagation, where the medium does not change volume. Instead, the medium for shear wave modes is rotational. The particle motion for longitudinal and shear wave modes is displayed in Figure 2.1.
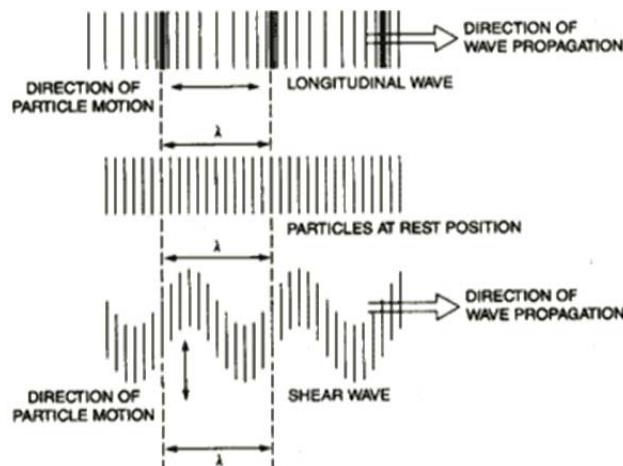
Figure 2.1: Particle motion for longitudinal and shear wave modes. Figure extracted from [68].

Note that only solids (as opposed to fluids) can propagate shear wave modes, which transfer shear stresses on the particles in motion in the transverse direction of propagation [70]. Acoustic wave propagation in *solid* media is the focus for the remainder of this paper.

Acoustic wave propagation in infinite elastic media is characterized using the acoustic wave equation by relating three main properties: density, displacement, and pressure. These properties are related by Euler's equation of motion, Navier's equation of motion, and the Hemholtz decomposition [70]. Each fundamental equation is derived to appreciate important characteristics of solid media and how they are related to elastic particle motion. The development of the wave equation has been simplified here to concentrate on the final outcome. A rectangular coordinate system will be used. For a more complete derivation including cylindrical coordinates, reference Graff [70]. Two important parameters described by the wave equation, which will be elaborated on, are acoustic wave velocity and attenuation.

First, Euler's equation is derived from Newton's second law by summing the forces in each principle direction and equating these forces to the mass and acceleration of the element in respective directions. A diagram of the stresses acting on a representative small element is shown in Figure 2.2 using a Cartesian coordinate system.
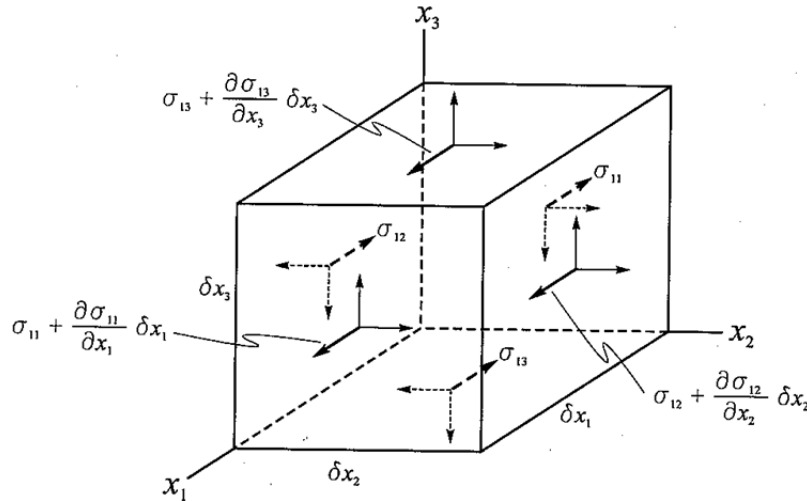
Figure 2.2: Schematic of the stress components acting on a small element. Figure extracted from [71].

The sum of the forces in the x_1 direction is given by,

$$\Sigma F_{x_1} = \left(\frac{\partial \sigma_{11}}{\partial x_1} \frac{\partial \sigma_{12}}{\partial x_2} \frac{\partial \sigma_{13}}{\partial x_3}\right) \delta x_1 \delta x_2 \delta x_3 \quad \ldots\ldots\ldots\ldots\ldots\ldots\ldots\ldots\ldots\ldots(2.1)$$

21

Thus, Newton's second law of motion in the x_1 direction, $F_{x1} = ma_1$, is given by,

$$\left(\frac{\partial \sigma_{11}}{\partial x_1} \frac{\partial \sigma_{12}}{\partial x_2} \frac{\partial \sigma_{13}}{\partial x_3}\right) \delta x_1 \delta x_2 \delta x_3 = \rho \delta x_1 \delta x_2 \delta x_3 \times \frac{d^2 u_1}{dt^2} \quad \text{.................(2.2)}$$

where $\rho \delta x_1 \delta x_2 \delta x_3$ is the element mass and $\frac{d^2 u_1}{dt^2}$ is its acceleration in the x_1-direction. The variables ρ and u_i are the density and particle displacements, respectively. The forces in the x_2 and x_3 directions are found similarly [70]. Assuming small displacements and velocities, Euler's equation is reduced to:

$$\rho \frac{\partial^2 u}{\partial t^2} = \nabla \cdot \sigma \quad \text{...(2.3)}$$

where u is the displacement vector, σ is the stress tensor, and ∇ is the three-dimensional differential operator. The stress tensor is necessary since the elastic motion in solids is directional.

Next, the stresses and strains of the small element shown in Figure 2.2 are related through the use of Hooke's law:

$$\sigma = \lambda I \nabla \cdot u + \mu (\nabla u + u \nabla) \quad \text{.........................(2.4)}$$

where I is the identity matrix, and λ and μ are the elastic Lamè constants. For elastic media, the Lamè constants are considered real [72]. If Equations 2.3 and 2.4 are equated, Navier's equation of motion is obtained:

$$\rho \frac{\partial^2 u}{\partial t^2} = (\lambda + \mu) \nabla \nabla \cdot u + \mu \nabla^2 u \quad \text{.........................(2.5)}$$

where ∇^2 is the three-dimensional Laplacian.

Now, by using the Hemholtz decomposition, longitudinal waves can be described by a scalar function, $\Phi = A_L e^{j(k_L x - \omega t)}$, while shear waves are described by a vector function, $H = A_S e^{j(k_S x - \omega t)}$. The resulting coupled expression takes the following form,

$$u = \nabla \Phi + \nabla \times H \quad \text{...(2.6)}$$

where $\nabla \Phi$ represents longitudinal motion and $\nabla \times H$ represents shear motion. In the Hemholtz decomposition relations above, A_i is the wave amplitude, k_i is the wavenumber, and ω is the angular frequency [10]. These parameters are related to each other and to the wavelength, λ, through the following equations:

$$\lambda = \frac{2\pi}{|k|} \quad \text{..(2.7)}$$

and

$$c = \frac{\omega}{|k|} \quad\quad\quad\quad\quad\quad\quad\quad\quad\quad\quad\quad\quad\quad\quad\quad\quad\quad\quad\quad\quad\quad\quad\text{(2.8)}$$

Finally, by plugging Equation 2.6 into Equation 2.5 and simplifying, the wave equations for longitudinal and shear wave propagation are given by,

$$\frac{\partial^2 \mathbf{\Phi}}{\partial t^2} = c_L^2 \nabla^2 \mathbf{\Phi} \quad\quad\quad\quad\quad\quad\quad\quad\quad\quad\quad\quad\quad\quad\quad\quad\quad\quad\quad\quad\quad\text{(2.9)}$$

and

$$\frac{\partial^2 \mathbf{H}}{\partial t^2} = c_S^2 \nabla^2 \mathbf{H} \quad\quad\quad\quad\quad\quad\quad\quad\quad\quad\quad\quad\quad\quad\quad\quad\quad\quad\quad\quad\text{(2.10)}$$

where c_L and c_S are the longitudinal and shear wave velocities, respectively. For an elastic lossless isotropic media, these velocities are given by,

$$c_L = \sqrt{\frac{\lambda + 2\mu}{\rho_o}} \quad\quad\quad\quad\quad\quad\quad\quad\quad\quad\quad\quad\quad\quad\quad\quad\quad\quad\quad\text{(2.11)}$$

and

$$c_S = \sqrt{\frac{\mu}{\rho_o}} \quad\quad\quad\quad\quad\quad\quad\quad\quad\quad\quad\quad\quad\quad\quad\quad\quad\quad\quad\quad\text{(2.12)}$$

The Lamè constants, λ and μ, are related to the elastic and bulk moduli as follows,

$$E = \frac{\mu(3\lambda + 2\mu)}{\lambda + \mu} \quad\quad\quad\quad\quad\quad\quad\quad\quad\quad\quad\quad\quad\quad\quad\quad\quad\quad\text{(2.13)}$$

and

$$K = \frac{3\lambda + 2\mu}{3} \quad\quad\quad\quad\quad\quad\quad\quad\quad\quad\quad\quad\quad\quad\quad\quad\quad\quad\quad\text{(2.14)}$$

respectively [72]. Note that generally the longitudinal wave velocity is approximately twice that of the shear wave velocity: $c_L \approx 2c_S$ [68]. The longitudinal and shear wave velocities are material dependent and remain constant for all frequencies of propagation in infinite elastic solid media. For a complete derivation of the acoustic wave equation, the reader is encouraged to reference Graff [70].

Since the Lamè constants are real for elastic media, the velocities are also real, but the wavenumber may still be complex. The real part of the wavenumber corresponds to plane wave propagation, while the imaginary component describes wave attenuation due to material absorption [41]. Thus far, it has been assumed that waves propagate in a lossless elastic medium with real solutions to the wave equation, although real applications must consider energy loss.

Complex solutions to the wave equation correspond to evanescent waves, which occur in bounded media such as a waveguide and characterized as standing waves in the complex near field [73]. Material damping is modeled by viscoelastic propagation with attenuation, which is covered in Section 2.2.2 [72].

2.2   GUIDED WAVE PROPAGATION IN DISPERSIVE MEDIA

Now that the wave equation has been derived for bulk substances and important wave characteristics defined, it is of interest to constrain the solid media with boundary conditions and introduce the concept of guided wave propagation. In general, if the transverse dimensions of a solid are close to a wavelength, λ, guided waves exists [41].

Two important concepts are discussed in the following sections: velocity and attenuation. Bulk waves and guided waves propagate very differently due to boundary conditions. In elastic isotropic bulk substances, wave velocity and attenuation are considered constant. In contrast, velocity and attenuation vary with frequency and thickness of the waveguide for guided wave propagation. This dependency is referred to as dispersion [41]. Dispersion arises in anisotropic media as well, where wave velocity is a function of direction. For the purpose of this paper, elastic wave propagation is only considered in isotropic media and dispersion is a result of structural geometry. Dayal and Kinra [74] proposed a study on dispersive plate waves in anisotropic media.

2.2.1   VELOCITY IN DISPERSIVE SOLID MEDIA

In dispersive media, the wave velocity is not only dependent on the material but on the thickness of the waveguide and the frequency of propagation. This requires two separate terms for velocity measurement: phase and group velocity. Figure 2.3 gives a visual representation of phase and group velocity.

The phase velocity for lossless media is defined as the rate at which individual wave crests travel within a wave packet, which is given by,

$$c_p = \frac{\omega}{k}$$ ………………………………………………………………….(2.15)

where ω and k are the angular frequency and wavenumber, respectively [75].

Note that the speed is directly proportional to the angular velocity. The phase velocity is also proportional to frequency and thickness of the media through the following relation: $c \propto f * t$. In dispersive media, the wave packet travels at a different velocity than the wave crests, leading to the concept of group velocity [75]. The group velocity is defined as the speed of transmission of information and/or energy in a wave packet [41]. The group velocity is found by taking the derivative of phase velocity (dispersion curve), as shown below.

$$c_g = \frac{\partial \omega}{\partial k} \quad \dots\dots\dots\dots\dots\dots\dots\dots\dots\dots\dots\dots\dots\dots\dots\dots\dots\dots\dots\dots\dots\dots\dots\dots(2.16)$$

Note that this concept only applies to dispersive media without attenuation. The velocity of a wave packet with attenuation is found from the energy velocity and discussed in the subsequent section.
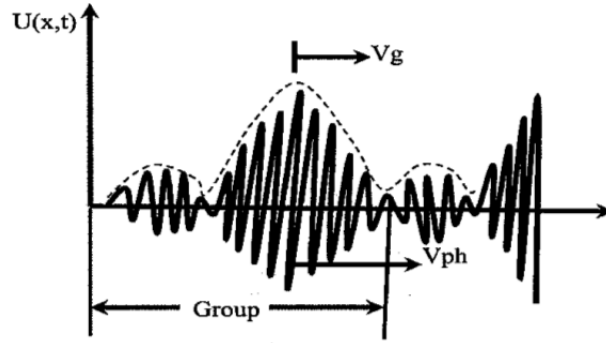
Figure 2.3: Schematic showing phase and group velocities of typical ultrasonic waveform. Figure extracted from [10].

2.2.2   ATTENUATION IN DISPERSIVE MEDIA

The main mechanisms for attenuation in guided waves are absorption and leakage. Boundary conditions have been the major focus of waveguides thus far; therefore the attenuation mechanism of leakage will be the focus. When a waveguide is embedded in another medium, some energy from the propagated guided wave leaks out of the waveguide into the surrounding medium [76]. The amplitude of the guided wave is reduced, as some energy escapes the waveguide. Figure 2.4 illustrates an attenuated guided wave as a result of energy leakage.
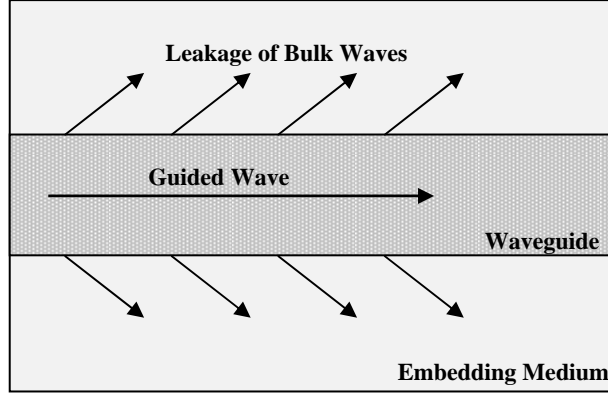
Figure 2.4: Schematic of an attenuated guided wave and energy leakage into surrounding medium.

The amount of energy that leaks into surrounding media is dependent on frequency, geometry, and the acoustic impedance mismatch between the waveguide and embedding medium. Figure 2.4 is an example of a leaky attenuated signal due to a minor change in surface impedance. As the impedance mismatch of waveguide and surrounding medium becomes larger, the inputted signal becomes less attenuated, as more energy is reflected back into the waveguide at the interface [77]. For a detailed discussion on acoustic impedance and transmission and reflection of acoustic wave energy at solid interfaces, refer to Kinsler et al [68].

A general solution to the wave equation describing the displacement for longitudinal and shear wave propagation is given in Equation 2.6. The wavenumber becomes complex for attenuative systems, where the real exponential term describes harmonic wave propagation while the imaginary exponential characterizes the attenuation [75]. As a result of the additional imaginary terms, new equations are derived to describe the phase velocity and attenuation in terms of updated material constants given by,

$$c_L \ or \ c_S = \frac{\omega}{|k_{re}|+i|k_{im}|} = \frac{c_P}{1+{i\kappa}/{2\pi}} \quad \dots\dots\dots\dots\dots\dots\dots\dots\dots\dots\dots\dots(2.17)$$

The longitudinal, $c_{p,L}$, and shear, $c_{p,S}$, wave velocities are given by the following complex quantities,

$$c_{p,L} = c_{L,re} - \kappa_L \frac{c_{L,im}}{2\pi} \quad \dots\dots\dots\dots\dots\dots\dots\dots\dots\dots\dots\dots\dots\dots(2.18)$$

and

$$c_{p,S} = c_{S,re} - \kappa_S \frac{c_{S,im}}{2\pi}\dots\dots\dots\dots\dots\dots\dots\dots\dots\dots\dots\dots\dots\dots\dots(2.19)$$

where κ_L and κ_S describe longitudinal and shear wave attenuation , respectively.

26

The attenuation is represented by the imaginary component with units of Nepers per wavelength and can be described in terms of wave amplitude as follows,

$$\alpha = \frac{20}{L} \log \frac{A_o}{A_1}$$ ....(2.20)

where A_o and A_1 are reference and observed amplitudes and L is the distance between observations. See Appendix A for details.

In solid media, longitudinal and shear waves propagate from the leaking energy of the waveguide. The remaining guided energy travels down the waveguide at different phase speeds depending on the frequency of propagation, and the speed of the entire wave packet for an attenuated signal can no longer be calculated by the group velocity [41]. It is found through the following equation for energy velocity by relating power flow and energy density:

$$c_e = \frac{\iint (P_z) dT dS}{\iint (TED) dT dS}$$ ....(2.21)

where P_z is the power flow density in the axial direction, S is the cross-section normal to the propagated energy, T is the period of the wave, and TED is the total energy density [78]. These concepts require a firm understanding of the displacement field which is not covered. For a detailed analysis see Ervin [78].

2.3   PLATE WAVES

The overall geometry of a waveguide can take many forms including thin plates, long round cylinders, long rectangular rods, and various others. For the purpose of this paper, only guided wave behavior in thin plates will be discussed herein. Many types of waves exist in plates including Rayleigh, Stonely, Love and Lamb waves [75]. Each type of wave has distinct particle motion and propagation characteristics. Each plate wave is described, followed by a brief introduction to the free plate problem used to characterize guided wave behavior in plate waveguides.

The first type of plate wave discussed is the Rayleigh wave, which travels along solid surfaces in semi-infinite half-space and penetrates to a depth of approximately one wavelength. Rayleigh waves are produced when longitudinal waves interact with solid media at oblique incidence greater than the second critical angle (see Appendix C) [68]. Longitudinal and shear motion

27

superimpose to create elliptical particle motion, normal to the major axis as seen in Figure 2.5. The velocity of Rayleigh waves is non-dispersive (i.e. not dependent on frequency) and travels at roughly 90% of a shear wave. A physical example of a Rayleigh wave is a tremor felt from an earthquake.
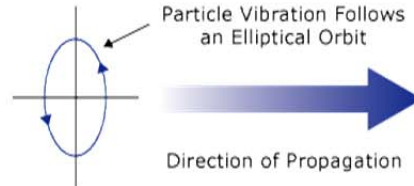
Figure 2.5: Elliptical particle motion and wave path for Rayleigh (surface) waves. Figure extracted from [69].

Stonely waves are essentially Rayleigh waves traveling at the interface of two semi-infinite half-spaces in contact with continuity of traction and displacement [41]. Shear wave velocities and elastic moduli of each semi-infinite half-space are required to be nearly identical for Stonely waves to exist [79].

Love waves are horizontally polarized shear waves (SH) that are present at a surface of semi-infinite half-space. Particle motion is transverse to the propagation direction as seen in Figure 2.6. Love waves are a special type of lamb wave but are decoupled from the bulk elastic motion [41]. The free plate problem used to describe elastic wave motion in dispersive plates excludes Love wave modes, as the displacement in the x_2 direction is assumed zero.
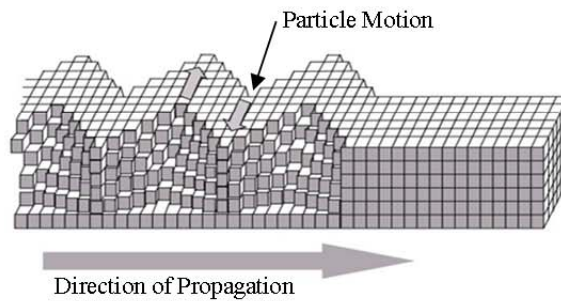
Figure 2.6: Transverse particle motion normal to the propagation direction in Love waves. Figure extracted from [80].

The final type of plate wave discussed is the lamb wave, which can be subdivided into two separate wave modes: Symmetric and antisymmetric (asymmetric). Particle motion is in-plane for symmetrical and normal to the plane of the plate for antisymmetric wave modes.

28

Symmetrical lamb waves are commonly referred to as "extensional" modes, since waves go through regions of compression and rarefaction about the median of a plane in the direction of wave propagation. Conversely, antisymmetric lamb waves are termed "flexural" modes due to the majority of wave motion transverse to the direction of propagation [41]. Plate surfaces tend to bend in the same transverse direction in antisymmetric lamb waves. Figure 2.7 illustrates lamb wave motion for both antisymmetric (asymmetric) and symmetric wave modes.
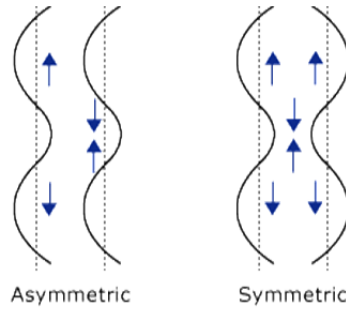
Figure 2.7: Schematic of asymmetric and symmetric lamb wave motion. Figure extracted from [69].

Assuming wavelengths of guided waves are significantly smaller than the width of an isotropic plate, a state of plane strain exists. The free plate problem is used to simplify analysis and is described by the Cartesian coordinate system established in Figure 2.8. A two-dimensional space exists for plane wave propagation, as the wave modes in the x_2 direction are decoupled from elastic bulk waves in the x_1-x_3 plane. Boundary conditions are introduced in the form of surface tractions ($t_i = \sigma_{ji} n_j$) with the top and bottom surfaces of the plate considered traction-free [70]. Solutions to the wave equation described in Equation 2.6 are used for the free plate problem with the assumption of plane strain.

Figure 2.8: Free plate problem in principle material coordinates.

In the subsequent chapter, a field matrix is derived using the free plate model to describe the relationship between stresses and displacements in plate waveguides. Then the free plate model is adjusted to account for multilayered systems using the global matrix method. For further details on the free plate problem, refer to Rose [41].

29

CHAPTER 3:

ANALYTICAL MODEL FOR LAMINATED SAFETY GLASS

An analytical model used to characterize guided wave propagation in multilayered systems, such as laminated safety glass (LSG), is described in this chapter. A solution to problems involving elastic wave propagation in multilayered plates is briefly described using the global matrix method. Additionally, a spring interface model is introduced and used to simulate adhesion between two layers (e.g. glass/PVB interface). Using the global matrix method and spring interface model in conjunction with an interactive windows program, Disperse v2.0.11, dispersion curves were constructed to model guided wave behavior in LSG specimens with different adhesion levels. Energy velocity and attenuation dispersion curves are compared with experimental nondestructive ultrasonic testing (UT) results (covered in Chapter 4) to predict adhesion levels in LSG specimens. Therefore, mode shape analysis, displacement profiles and simulated signals are analyzed to better understand the partial wave behavior within multilayered plates, and specific wave modes are initially selected for UT.

3.1 WAVE PROPAGATION IN MULTILAYERED PLATES

Wave propagation in multilayered plates is described using the global matrix method by combining field matrices of longitudinal and shear waves for thin monolithic plates into one large global matrix system. First, boundary conditions at the interface of adjoining layers are matched and partial wave modes within multilayered systems are described. The cross section of a thin multilayered system, such as LSG, is shown below in Figure 3.1.
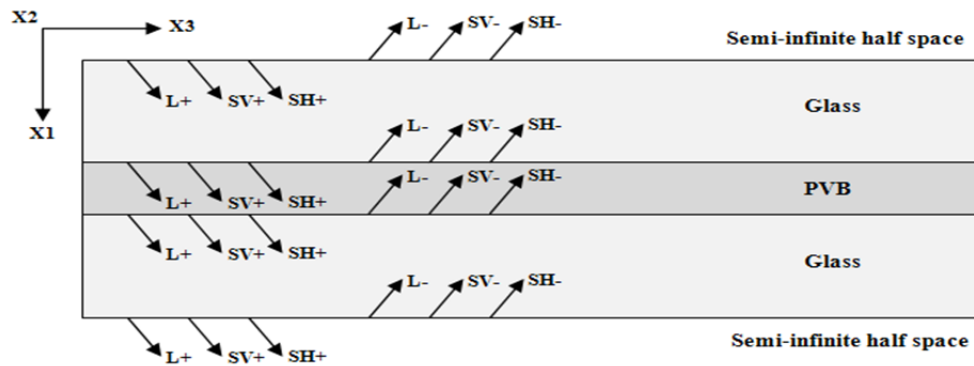
Figure 3.1: Multilayered system (e.g. LSG) showing the interaction of partial waves between neighboring layers to make up guided waves.

As seen in Figure 3.1, boundaries at the interface between layers create geometrical constraints in the transverse, x_1, direction, and each wave mode forms a traveling composite wave consisting of longitudinal (L) and shear (S) wave components within each layer. The positive and negative signs correspond to partial waves arriving on top and bottom of a layer, respectively. Two types of shear waves are present in multilayered plates. Shear vertical (SV) wave modes are displaced in the x_1-direction, while shear horizontal (SH) wave mode displacement occurs entirely in the x_2-direction. Following the free plate problem described in the preceding chapter, isotropy in the x_2 direction is assumed and a state of plane strain exists [41]. Therefore, the models presented in this section neglect shear horizontal (SH) wave modes since they are decoupled from the other lamb type waves.

The field equations for each layer are alike and described by the following invariant factor,

$$F = e^{(\xi x_3 - \omega t)} \quad \text{...(3.1)}$$

where ξ is the wavenumber component in the x_3 direction and declared the *plate wavenumber.* All displacement and stress equations retain the same frequency and plate wavenumber in adjoining layers since waves traveling in the x_3 direction share the same frequency and spatial properties at the interface [81]. The displacements, u_i, and stresses, σ_{ij}, of longitudinal and shear waves for each layer in multilayered plates are found from the following set of field equations:

Longitudinal Bulk Waves:

$$u_1 = \pm \zeta_1 A_{L\pm} F e^{\pm i \zeta_1 x}$$

$$u_3 = \xi A_{L\pm} F e^{\pm i \zeta_1 x}$$

$$\sigma_{11} = i\rho(\omega^2 - 2c_2^2 \xi^2) A_{L\pm} F e^{\pm i \zeta_1 x}$$

$$\sigma_{22} = i\rho\omega^2 \left(1 - 2 \frac{c_2^2}{c_1^2} \right) A_{L\pm} F e^{\pm i \zeta_1 x} \quad \text{...................................(3.2)}$$

$$\sigma_{33} = i\rho(\omega^2 - 2c_2^2 \zeta_1{}^2) A_{L\pm} F e^{\pm i \zeta_1 x}$$

$$\sigma_{13} = 2i\rho c_2^2 \xi \zeta_1 A_{L\pm} F e^{\pm i \zeta_1 x}$$

$$\sigma_{12} = \sigma_{23} = 0$$

where $\zeta_1 = \left(\omega^2 / c_1^2 - \xi^2 \right)^{1/2}$ and c_1, c_2 are the longitudinal and shear wave velocities expressed

in Equations 2.11 and 2.12, respectively. To model attenuative systems, the wave velocities in Equations 2.18 and 2.19 are used.

Shear Bulk Waves:

$$u_1 = -\xi A_{S\pm} F e^{\pm i \zeta_2 x}$$

$$u_3 = \pm \zeta_2 A_{S\pm} F e^{\pm i \zeta_2 x}$$

$$\sigma_{11} = \mp 2i\rho c_2^2 \xi \zeta_2 A_{S\pm} F e^{\pm i \zeta_2 x}$$

$$\sigma_{22} = 0 \quad\text{...(3.3)}$$

$$\sigma_{33} = -\sigma_{11}$$

$$\sigma_{13} = i\rho(\omega^2 - 2c_2^2 \xi) A_{S\pm} F e^{\pm i \zeta_2 x}$$

$$\sigma_{12} = \sigma_{23} = 0$$

where $\zeta_2 = \left(\omega^2 / c_2^2 - \xi^2 \right)^{1/2}$.

The displacements and stresses are found by summing the partial wave contributions in each material layer. The field quantities can be used to describe multilayered systems by extracting only those in which continuity at the interfaces apply. As mentioned earlier, a state of plane strain is assumed for this model which reduces the necessary field quantities to: u_1, u_3, σ_{11}, and σ_{13}.

Using the following substitutions,

$$g_{\zeta 1} = e^{i \zeta_1 x_1} \quad\text{...(3.4)}$$

and

$$g_{\zeta 2} = e^{i \zeta_2 x_2} \quad\text{...(3.5)}$$

the field displacement and stresses are described in terms of a large field matrix, $[D]$, and an array of wave amplitudes for longitudinal and shear waves on top and bottom material layers.

$$\begin{bmatrix} u_1 \\ u_3 \\ \sigma_{11} \\ \sigma_{13} \end{bmatrix} = \begin{bmatrix} \zeta_1 g_{\zeta 1} & -\dfrac{\zeta_1}{g_{\zeta 1}} & -\xi g_{\zeta 2} & -\dfrac{\xi}{g_{\zeta 2}} \\ \xi g_{\zeta 1} & \dfrac{\xi}{g_{\zeta 1}} & \zeta_2 g_{\zeta 2} & -\dfrac{\zeta_2}{g_{\zeta 2}} \\ i\rho(\omega^2 - 2c_2^2\xi^2)g_{\zeta 1} & \dfrac{i\rho(\omega^2 - 2c_2^2\xi^2)}{g_{\zeta 1}} & -2i\rho c_2^2 \xi \zeta_2 g_{\zeta 2} & \dfrac{2i\rho c_2^2 \xi \zeta_2}{g_{\zeta 1}} \\ 2i\rho c_2^2 \xi \zeta_1 g_{\zeta 1} & \dfrac{-2i\rho c_2^2 \xi \zeta_1}{g_{\zeta 1}} & i\rho(\omega^2 - 2c_2^2\xi^2)g_{\zeta 2} & \dfrac{i\rho(\omega^2 - 2c_2^2\xi^2)}{g_{\zeta 2}} \end{bmatrix} \begin{bmatrix} A_{L+} \\ A_{L-} \\ A_{S+} \\ A_{S-} \end{bmatrix} \quad ....(3.6)$$

Once the displacements and stresses are characterized in each material layer, they can be combined into one large system. One method commonly used to describe elastic wave behavior in multilayered media is the global matrix method. Knopoff [82] originally developed this technique for homogenous systems using Laplace's development by minors. Randall [83] used a simplified model that separated frequency-dependent operations to reduce computing time for models on oceanic waves and structures. Schmidt and Jensen [84] have applied this method to obtain full wave solutions to elastic waves propagating in multilayered viscoelastic media.

The global matrix method assembles a single matrix (global matrix) representing the entire multilayered system. The global matrix consists of $4(n-1)$ equations for Lamb wave solutions, where *n* represents the number of layers. Note that the two semi-infinite half-spaces (see Figure 3.1) each count as a layer as well. Using the laminate layup shown in Figure 3.1 as an example, the global matrix of a typical 5-layered system is described. The global matrix is distributed into five columns representing each layer and four rows characterizing stresses and displacements for the respective layers. Continuity of stresses and displacements must hold true between adjoining layers. As a result, the field matrix from Equation 3.6 is represented in terms of top, [D$_t$], and bottom, [D$_b$], interfaces for each layer in the system. The resulting global matrix of the 5-layered system takes the following form,

$$[G] = \begin{bmatrix} [D_{1b}^-] & [-D_{2t}] & 0 & 0 & 0 \\ 0 & [D_{2b}] & [-D_{3t}] & 0 & 0 \\ 0 & 0 & [D_{3b}] & [-D_{4t}] & 0 \\ 0 & 0 & 0 & [D_{4b}] & [-D_{5t}^+] \end{bmatrix} \quad ....(3.7)$$

(Glass) (PVB) (Glass)

(Semi-infinite Half-space)

Each column possesses all positions and constituent coefficients describing the partial wave amplitudes (L± and SV±) in each layer. The exterior columns on the far left and far right represent the top and bottom semi-infinite half-spaces, respectively. The central column represents the PVB interlayer while the remaining two columns represent glass layers. Boundary conditions between neighboring layers are satisfied by multiplying the global matrix by respective partial wave amplitudes. The resulting characteristic equation is written as follows,

$$[G]\{A\} = 0 \quad \text{...}(3.8)$$

where $\{A\}$ is a vector of partial wave amplitudes and $[G]$ is the global matrix. The partial wave solution for multilayered systems depends on a specific combination of frequency, wavenumber and attenuation values and is satisfied when the determinant of the global matrix is zero [83].

Pavlakovic and Lowe [81] developed an interactive windows program, Disperse v2.0.11 that utilizes the global matrix method to calculate and trace dispersion curves for multilayered systems (e.g. LSG). Each wave mode is traced by converging to the roots of the characteristic equation (Equation 3.8). In the following section, a spring interface model is presented to simulate adhesion at the glass/PVB interface of LSG. Dispersion curve models are then produced to appreciate guided wave behavior in LSG.

3.2   SPRING INTERFACE MODEL

In LSG, the adhesion level at the interface of the outer glass plates and PVB interlayer is modeled using a quasi-static spring model (QSM) developed by Baik and Thompson [85]. The adhesive bond is modeled using a zero thickness layer of normal and transverse springs, where higher spring constants represent higher adhesion levels. The global matrix is modified to account for the additional spring layers, which is described by Pavlakovic and Lowe [81]. The five-layered system (plus two semi-infinite half spaces), simulating LSG, is illustrated in Figure 3.2. The stress field is assumed continuous across spring layers. Stresses are transferred directly from the glass outer layer to the PVB interlayer, which is consistent with a physical adhesive bond in LSG. Conversely, the displacements are discontinuous across the spring layer since the adhesion contact is modeled as an imperfect interface.
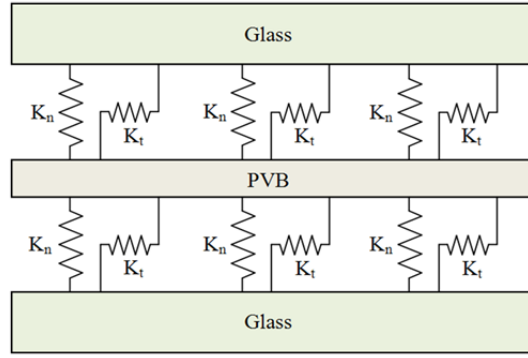
Figure 3.2: Spring model using normal and transverse spring layers to represent the adhesive bond in LSG.

As described in Chapter 1, the glass and PVB surfaces are rough and represented by regions of peaks and valleys. The interface stiffness (i.e. spring constants) is dependent on the area of contacting asperities and determined using fracture mechanics principles. The imperfect interface between glass and PVB can be very complex, although the contact regions have been successfully described by Huo [10]. Profilometer and atomic force microscopy measurements were used to characterize glass and PVB surfaces, and an edge-crack and center-penny-crack fracture mechanics model were used to describe the contacting region at the glass and PVB interface for LSG specimens with various levels of adhesion. Crack ratios were developed to describe random distribution of contacting regions at the glass and PVB interface. Smaller crack ratios corresponded to greater contact at the interface and therefore stronger adhesive bonds. Using various crack ratios and the QSM, spring constants were evaluated in terms of pummel number, representing different levels of adhesion. The pummel scale is a relative scale ranging from 1 (complete delamination) to 10 (rigid interface).

Similar models have been used in the past to complement NDT experimental results by the following authors: [10, 16, 19, 48-50, 52-54, 63]. Using numerical analysis of dispersion relations, Pilarski and Rose [52] characterized partial lamb wave behavior in three-layered asymmetric adhesive systems and selected suitable wave modes for interfacial weakness analysis. Alleyne and Cawley [86] described proper wave mode selection and appropriate excitation frequency using analytical dispersion models and UT on butt-welded steel plates. Xu and Datta [87] compared a similar spring model to a density model. Both models predicted exact solutions relatively well. As expected, increases in stiffness and/or density tended to lower the cutoff frequencies and velocities of partial wave modes.

3.3 DISPERSION CURVES AND WAVE MODE SELECTION FOR EXPERIMENTAL ANALYSIS

A preliminary analytical dispersion curve model is presented to simulate general guided wave behavior in LSG. The QSM was used to express the adhesive bond between glass and PVB with a zero thickness and zero mass layer of longitudinal and transverse springs. The two spring layers were added to the global matrix, and the displacements and stresses in each layer are described by partial wave amplitudes. The model layup for LSG is shown in Figure 3.2, which is embedded in two semi-infinite half-spaces.

Phase velocity, energy velocity and attenuation dispersion curves with various adhesion levels (pummel numbers) are presented and used to select appropriate partial wave modes for experimental UT (covered in Chapter 4). Material properties of the LSG constituents were not disclosed for experimental specimens. Therefore, a parametric study was employed to investigate the sensitivity of guided wave behavior in LSG to variations in laminate constituent material properties.

3.3.1 PRELIMINARY DISPERSION MODEL

Material properties for float glass and PVB constituents and spring constants for an assortment of pummel numbers (adhesion levels) were extracted from Huo [10] for this model and provided in Tables 3.1 and 3.2, respectively. In order to represent an extremely weak adhesive bond, spring constants for pummel number 1 were approximated using a power regression fit on the spring constant values for other given pummel number models (see Appendix B for details). Lamina thicknesses were measured from experimental specimens supplied for UT in Chapter 4. Phase velocity, energy velocity and attenuation dispersion curves are examined and potential wave modes are selected for UT purposes.

Table 3.1: Material properties of laminated safety glass constituents used for preliminary model.

	Thickness (mm)	Density (g/cm^3)	Young's Modulus (GPa)	Poisson's Ratio	Longitudinal Attenuation (Np/m)	Shear Attenuation (Np/m)
Float Glass	2.10	2.5	72	0.25	0	0
PVB	0.793	1.1	3.9	0.34	8.51	43.5

*values extracted from [10].

Table 3.2: Spring constants representing different levels of adhesion for preliminary spring model.

Pummel Number	Normal Spring Constant (N/m^3)	Transverse Spring Constant (N/m^3)
1	2.5315 E+11	8.8661 E+10
3	6.8785 E+11	2.4091 E+11
4	8.9754 E+11	3.1436 E+11
5	1.0778 E+12	3.7750 E+11
6	1.4933 E+12	5.2302 E+11
8	1.7010 E+12	5.9577 E+11

* Values extracted from [10]; Pummel 1 values estimated using a power regression fit (see Appendix B).

Symmetric and Antisymmetric wave modes propagate in multilayered plates and are represented by red and blue dispersion curves, respectively. Each dispersion curve model contains one fundamental wave mode for both symmetric and antisymmetric waves. Fundamental wave modes originate at zero frequency and are the only waves present over the entire frequency spectrum. As frequencies increase, higher order wave modes develop at various plate resonant frequencies, creating a more complex guided wave envelope. Modes are labeled alphanumerically in dispersion curve plots, where symmetric and antisymmetric waves are represented with *S* and *A*, respectively. Fundamental modes are labeled with "0" and each higher order mode is labeled incrementally (i.e. 1, 2, …n).

3.3.1.1 PHASE VELOCITY

Phase velocity dispersion curves for LSG specimens were initially traced to understand the dispersive nature of multilayered systems. The phase velocity dispersion curves for a pummel number 3 laminate are displayed in Figure 3.3. The symmetric and antisymmetric fundamental modes are labeled and originate at zero frequency. Frequencies above 1 MHz contain many overlapping wave modes, making the guided wave behavior in this region is very complex and unappealing for UT velocity measurements.
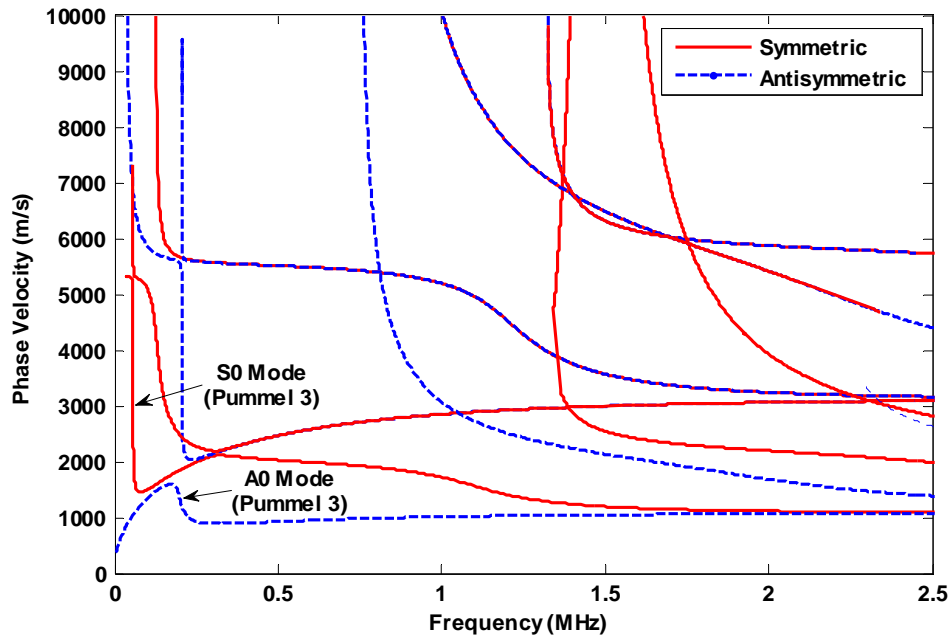
Figure 3.3: Symmetric (solid red curves) and antisymmetric (dashed blue curves) phase velocity dispersion curves for pummel number 3 dispersion model (See Tables 3.1 and 3.2 for material properties and spring constants).

Phase velocity dispersion curves are plotted in Figure 3.4 for laminates with pummel number 3 and pummel number 8, which correspond to relatively low and high adhesion levels, respectively. Frequencies above 1 MHz have been intentionally omitted as described above.
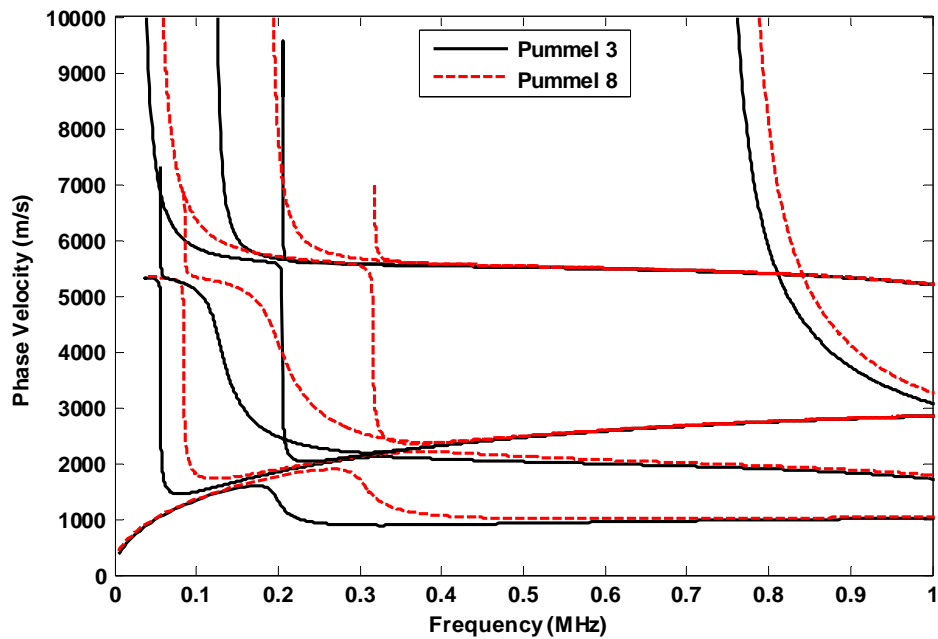
Figure 3.4: Phase velocity dispersion curves for pummel number 3 (solid black curves) and pummel number 8 (dashed red curves) dispersion models (See Tables 3.1 and 3.2 for material properties and spring constants).

Wave modes tend to originate at higher frequencies for laminates with higher pummel numbers. This phenomenon is explained through the concept of simply harmonic motion of a constant mass, m, on a spring. The angular frequency, ω, is directly related to the spring constant, k, as follows,

$$\omega = \sqrt{\frac{k}{m}} \quad \ldots\ldots\ldots\ldots\ldots\ldots\ldots\ldots\ldots\ldots\ldots\ldots\ldots\ldots\ldots\ldots\ldots\ldots\ldots\ldots(3.9)$$

Naturally, as the interface stiffness (i.e. spring constant) between glass and PVB interlayer increases, laminate resonant frequencies increase accordingly.

Phase velocities in dispersive media are very difficult to measure using UT. Therefore, energy velocity dispersion curves were calculated in Disperse using Equation 2.21 and traced from the phase velocity data points. In addition, attenuation dispersion curves are traced and used to compliment UT.

3.3.1.2 ENERGY VELOCITY

Generally speaking, glass has very little material attenuation and is modeled as a lossless medium. In contrast, the PVB interlayer in LSG is highly attenuative and absorbs/dissipates a great deal of energy. As a result, energy velocity dispersion curves were traced rather than group velocity. Energy velocity dispersion curves for pummel number 3 laminates are displayed in Figures 3.5. Recall, symmetric and antisymmetric wave modes are represented by red and blue curves, respectively. In addition, the bulk (Rayleigh) velocity is shown with a dotted line.

Energy velocity dispersion curves are useful aids for UT. Energy velocity measurements are performed in Chapter 4 and related to updated dispersion curve models to estimate the adhesion level of LSG specimens. For UT to be beneficial, one discernible wave mode must be separated from the rest of the wave envelope. Therefore, frequencies below 200 kHz are impractical for ultrasonic energy velocity measurements, as too many wave modes overlap creating a very complex waveform. The frequency band of 200 kHz to 600 kHz is investigated in the preliminary model to select a potential wave mode for UT energy velocity measurements. As seen in Figure 3.5, six wave modes exist in this frequency range: one fundamental wave mode and two higher order wave modes for both symmetric and antisymmetric waves.

39
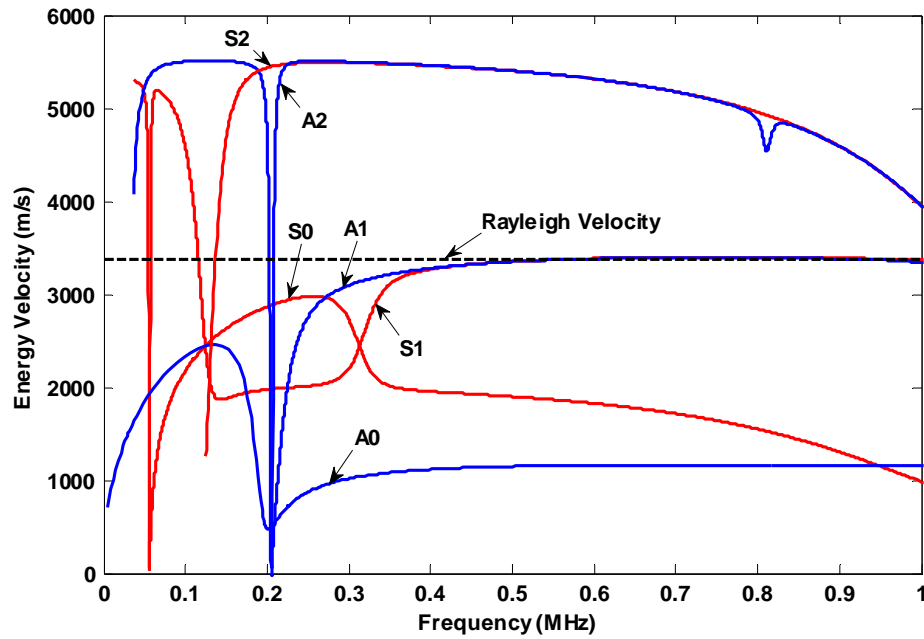
Figure 3.5: Symmetric (red curves) and antisymmetric (blue curves) energy velocity dispersion curves for pummel number 3 dispersion model (See Tables 3.1 and 3.2 for material properties and spring constants). The Rayleigh velocity is denoted by the dashed black line.

The guided wave envelope can be reduced further by eliminating the second order symmetric (S2) and antisymmetric (A2) wave modes by means of Snell's law. Refer to Appendix C for details on Snell's law. The displacement and power flow profiles for the remaining modes (A1, A0, S1, and S0) were examined in the frequency range of interest to settle on a suitable wave mode for UT. Figures 3.6 presents a profile view of the normalized displacement and power flow of the A0 mode with pummel number 3 spring constants in the frequency range of interest.

A large amount of displacement and energy must be present at the top surface of the laminates for piezoelectric ultrasonic transducers to detect a wave signal. As seen in Figure 3.6a, the fundamental antisymmetric (A0) wave mode has zero surface displacement in the outer glass layers. Additionally, all of the wave mode energy is concentrated in the PVB interlayer which is depicted by the power flow diagram in Figure 3.6b. Similar profiles exist for the A0 mode at all frequencies between 200 kHz and 600 kHz. As a result, the A0 mode is not expected to be detected using UT and is not used for experimental energy velocity measurements.

40
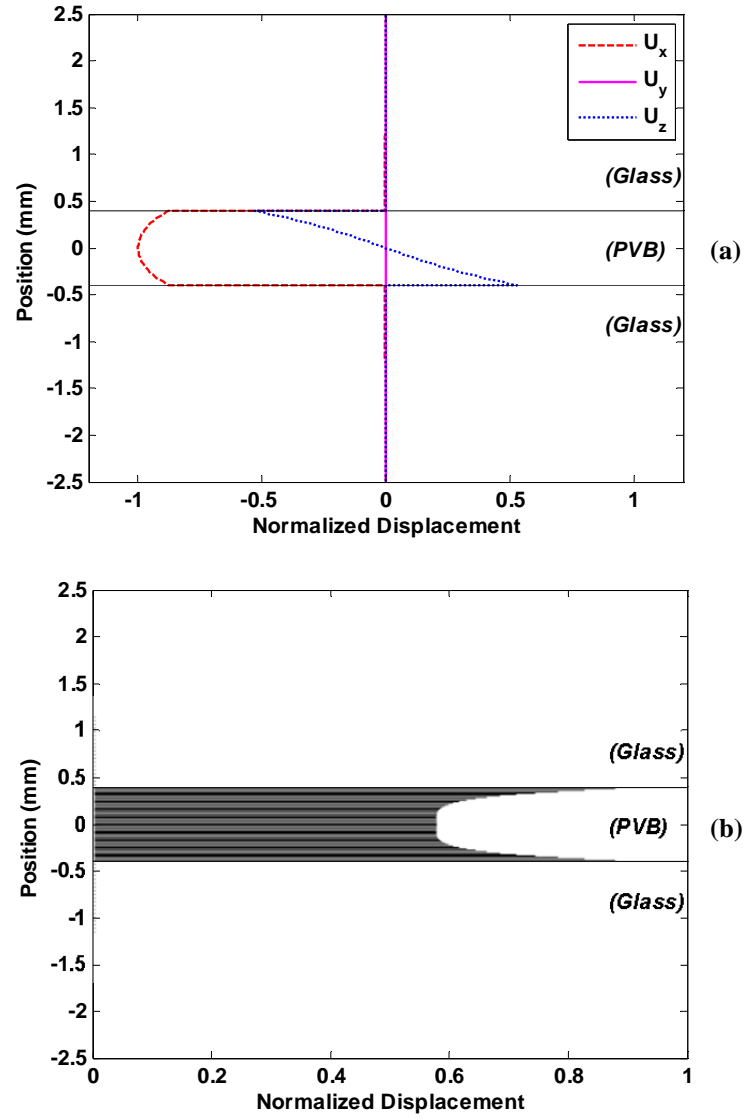
Figure 3.6: Normalized (a) displacement profile and (b) power flow of the A0 wave mode at 360 kHz for pummel number 3 dispersion model (See Tables 3.1 and 3.2 for material properties and spring constants).

The A1 wave mode shows ample surface displacement and power flow for UT energy velocity measurements, while the S0 and S1 wave modes experience energy fluctuations between the outer glass layers and PVB interlayer in the frequency range of interest. The normalized displacement profile and power flow of the A1 mode at 360 kHz are shown in Figure 3.7. Most of the energy is concentrated in the outer glass plates, which will be detected with piezoelectric transducers. The displacement and energy remain in the outer glass layers for the entirety of the A1 mode in the frequency range of interest. Therefore, the A1 mode shows excellent potential for UT energy velocity measurements.
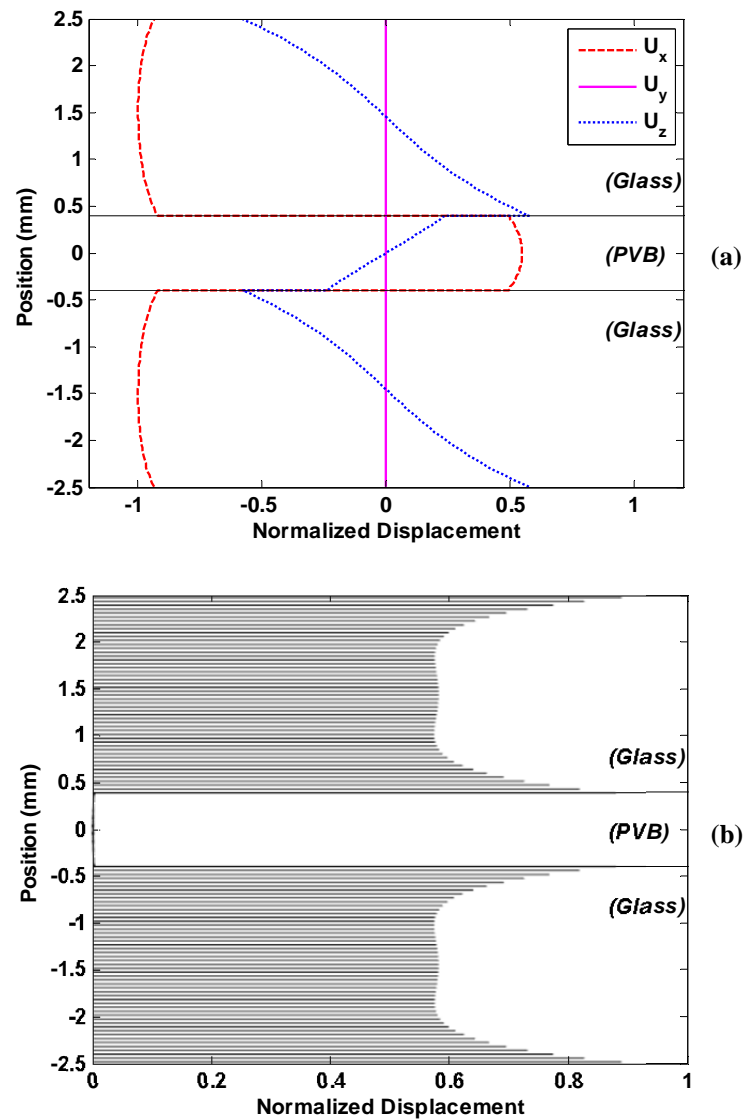
Figure 3.7: Normalized (a) displacement profile and (b) power flow of the A1 wave mode at 360 kHz for pummel number 3 dispersion model (See Tables 3.1 and 3.2 for material properties and spring constants).

The partial wave energy in the S0 and S1 modes is more complicated than the A1 mode in the frequency range of interest (200 kHz – 600 kHz). A useful tool Disperse offers is mode shape analysis, which provides a visual representation of partial wave mode motion. The S0 mode shape was examined at two critical frequencies and is plotted with pummel number 3 dispersion curves in Figure 3.8. The energy velocity of the S0 wave mode is highly dependent on the location of partial wave energy within LSG layers. As more of the energy is transmitted in the outer glass layers, energy velocity increases accordingly. Conversely, energy velocities are much lower when most of the wave energy is concentrated in the PVB interlayer. The bulk velocity of PVB is much lower than the bulk velocity of glass, which supports this occurrence.
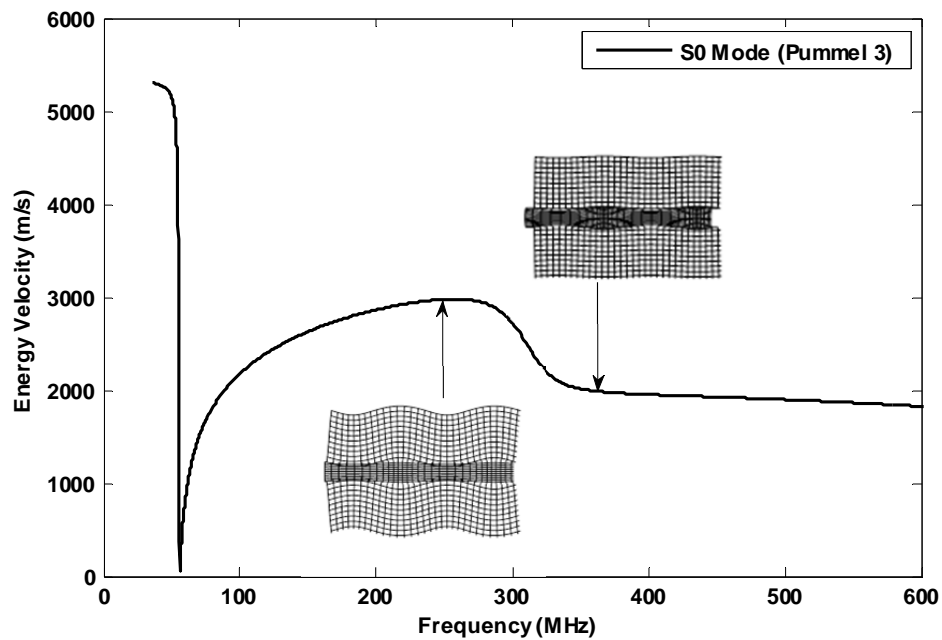
Figure 3.8: Mode shape behavior of the S0 wave mode in the frequency range of interest for pummel number 3 dispersion model (See Tables 3.1 and 3.2 for material properties and spring constants).

As seen in Figure 3.8, the S0 mode increases in energy velocity until it reaches a peak value around 260 kHz. Most of the energy present in the S0 wave mode is concentrated in the outer glass layers over these frequencies. At higher frequencies, the wave mode energy is transferred into the PVB interlayer. As a result, the S0 mode experiences a sharp drop in energy velocity between 260 kHz and 360 kHz.

43

To illustrate the transfer of energy over these frequencies, the normalized displacement and power flow profiles of the S0 wave mode are plotted in Figures 3.9 and 3.10 at 260 kHz and 360 kHz, respectively. Referring to Figure 3.9, the S0 wave mode shows sufficient surface displacement and power flow in the outer glass layers at 260 kHz, which is consistent with the partial wave mode shape shown in Figure 3.8. At higher frequencies, the surface displacement diminishes and most of the energy is concentrated in the PVB interlayer as seen in Figure 3.10. As a result, the S0 mode should only be detected in the frequency range of (approximately) 200 kHz to 360 kHz.
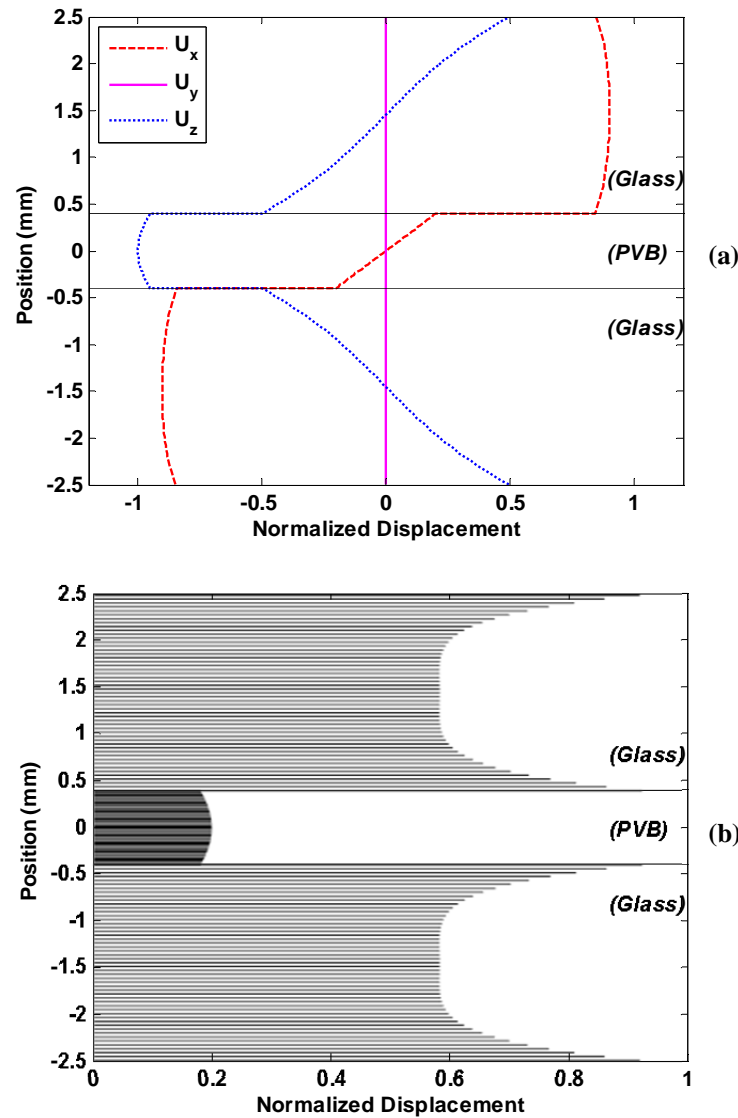
Figure 3.9: Normalized (a) displacement profile and (b) power flow of the S0 wave mode at 260 kHz for pummel number 3 dispersion model (See Tables 3.1 and 3.2 for material properties and spring constants).

44
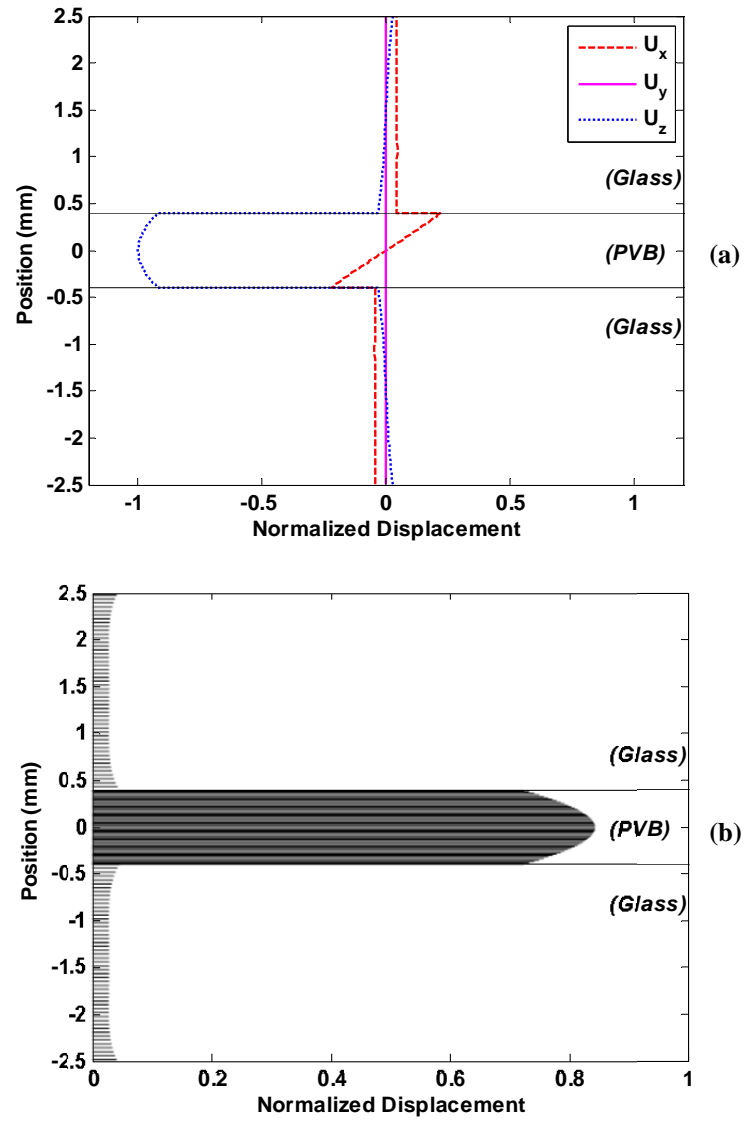
Figure 3.10: Normalized (a) displacement profile and (b) power flow of the S0 wave mode at 360 kHz for pummel number 3 dispersion model (See Tables 3.1 and 3.2 for material properties and spring constants).

A similar transfer of wave mode energy occurs in the S1 wave mode over the same frequency band. Instead, the energy of the S1 wave mode is concentrated in the PVB interlayer for lower frequencies and shifts to the outer glass plates at higher frequencies as seen in Figure 3.11. Once all of the energy is isolated in the outer glass layers, the S1 mode converges with the A1 mode and approaches the Rayleigh velocity.
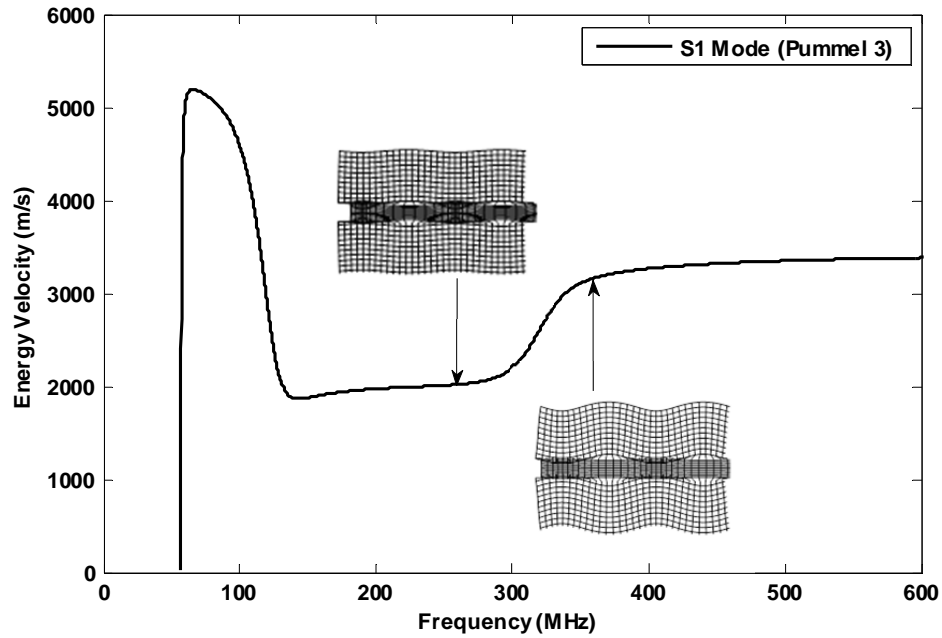
Figure 3.11: Mode shape behavior of the S0 wave mode in the frequency range of interest for pummel number 3 dispersion model (See Tables 3.1 and 3.2 for material properties and spring constants).

The normalized displacement and power flow profiles of the S1 wave mode at 260 kHz and 360 kHz are shown in Figures 3.12 and 3.13, respectively. As expected, very little surface displacement exists in the S1 wave mode at 260 kHz (Figure 3.12a), as most of the wave energy is concentrated in the PVB interlayer (Figure 3.12b). Conversely, ample surface displacement is present at 360 kHz (Figure 3.13a) with most of the energy flowing in the outer glass layers (Figure 3.13b).
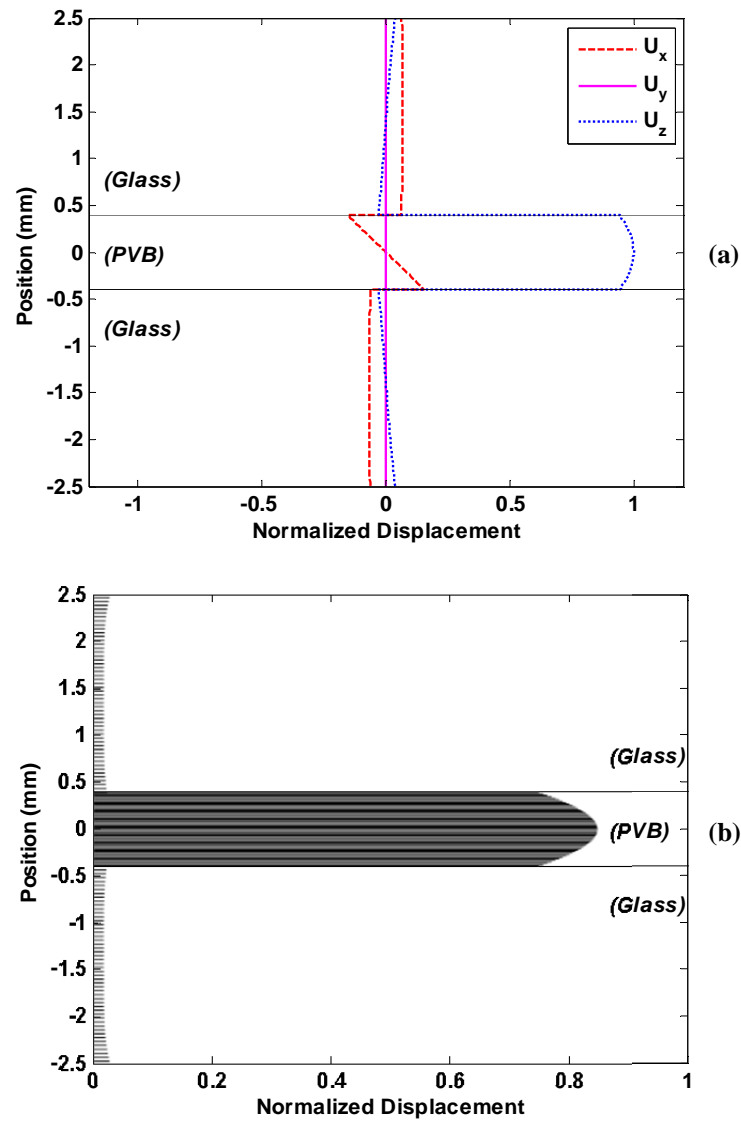
Figure 3.12: Normalized (a) displacement profile and (b) power flow of the S1 wave mode at 260 kHz for pummel number 3 dispersion model (See Tables 3.1 and 3.2 for material properties and spring constants).
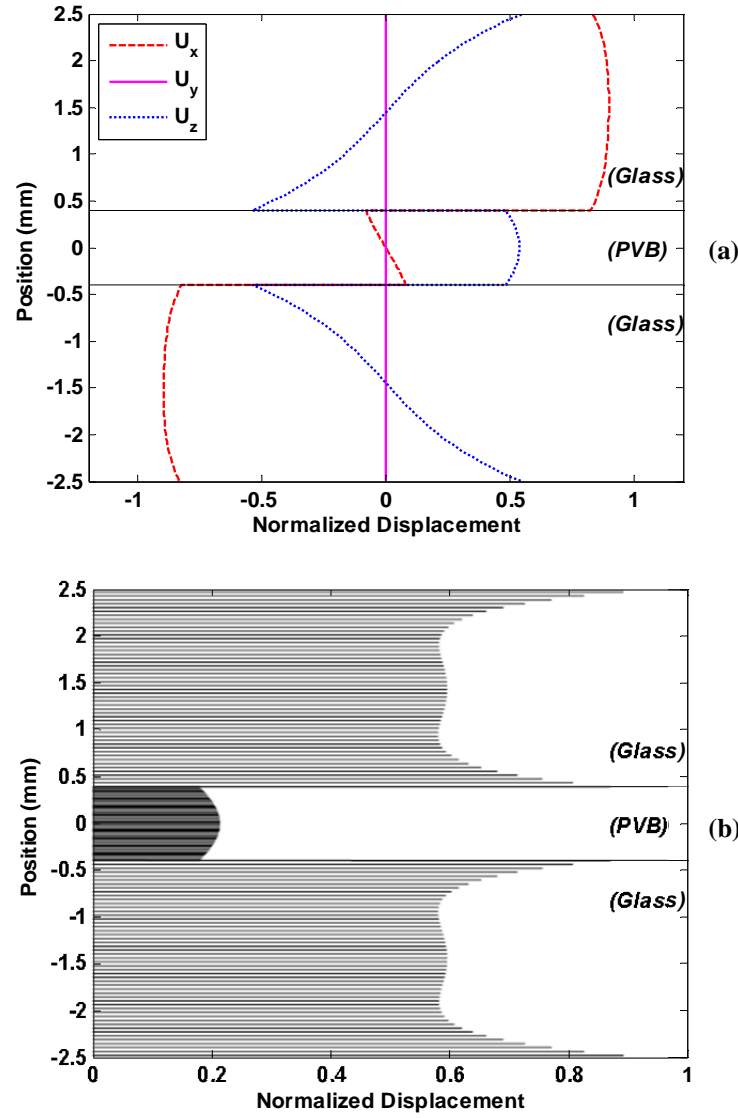
Figure 3.13: Normalized (a) displacement profile and (b) power flow of the S1 wave mode at 360 kHz for pummel number 3 dispersion model (See Tables 3.1 and 3.2 for material properties and spring constants).

Based off a preliminary analysis of energy velocity dispersion curves, three different wave modes (A1, S0 and S1) will likely be detected between 200 kHz and 600 kHz using UT. Energy velocity dispersion curve models representing very low adhesion (pummel number 3) and very high adhesion (pummel number 8) are plotted in Figure 3.14 for the A1, S0 and S1 wave modes. The two extreme cases of adhesion create a boundary envelope within which experimental results should fall. In Chapter 4, ultrasonic energy velocity measurements are compared to dispersion curve models with different pummel numbers to predict the adhesion level in LSG specimens.
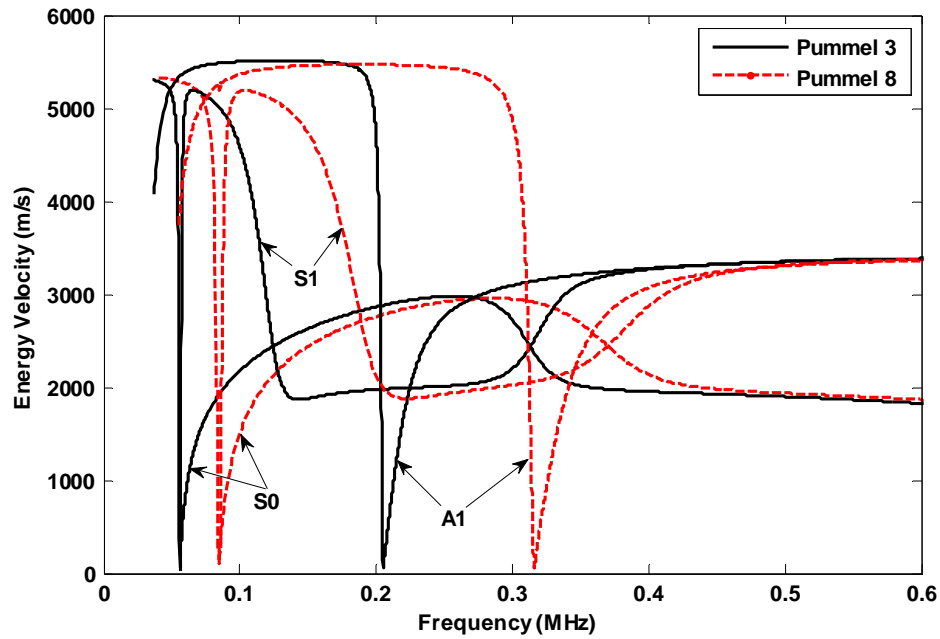
Figure 3.14: Energy velocity dispersion curves of the A1, S0 and S1 wave modes for pummel number 3 (solid black curves) and pummel number 8 (dashed red curves) dispersion models (See Tables 3.1 and 3.2 for material properties and spring constants).

The wave modes for pummel number 8 have shifted toward higher frequencies as expected. A frequency range between 250 kHz and 500 kHz shows good potential for UT energy velocity measurements, as most modes have separated out from one another and a large dynamic range of energy velocities is apparent from low to high adhesion models.

3.3.1.3 ATTENUATION

Attenuation dispersion curves are helpful at describing the energy loss of guided waves in LSG specimens as a function of frequency. The attenuation mechanism focused on in this section is caused by energy fluctuations between the outer glass layers and PVB interlayer of LSG. As energy is pumped from the outer glass layers to the highly damped PVB interlayer, energy loss attributed to absorption occurs. Modulation of energy between laminas is most prevalent at resonant frequencies of specific wave modes. Therefore, various wave modes were examined for significant attenuation spikes at resonant frequencies. The S2 wave mode shows most potential for UT attenuation measurements. Referring to Figure 3.15, the pummel number 3 dispersion model shows considerable attenuation at two resonant frequencies of the S2 wave mode.

49
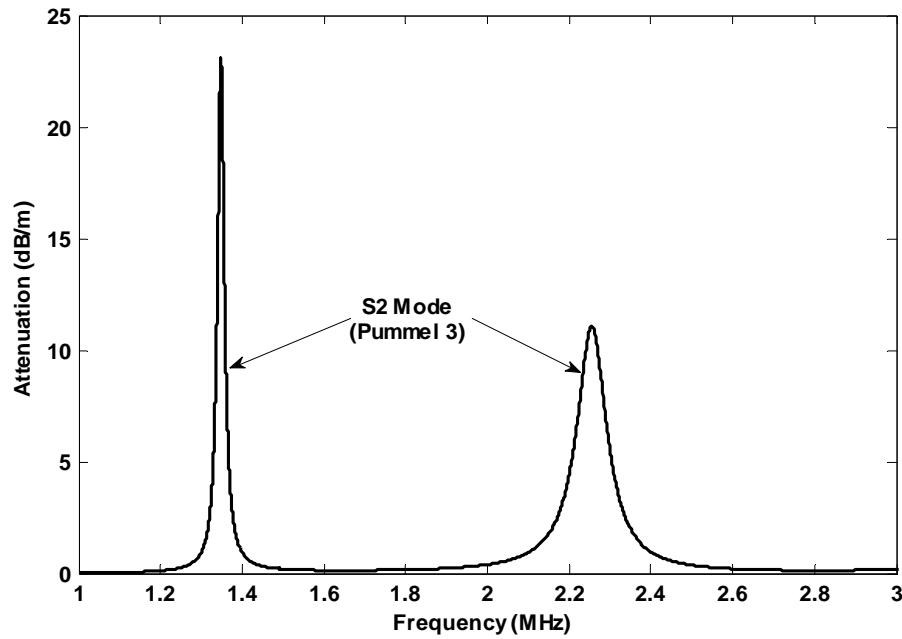
Figure 3.15: Attenuation dispersion curves of the S2 wave mode for pummel number 3 dispersion model (See Tables 3.1 and 3.2 for material properties and spring constants).

The amount of energy that is pumped into the attenuative interlayer is highly dependent on the level of adhesion (pummel number) at the glass and PVB interface. In the analytical dispersion models, higher pummel numbers hold stiffer spring constants. Consequently, a greater amount of energy is driven into the PVB interlayer resulting in greater attenuation. In contrast, lower pummel number dispersion models are less attenuative, since less energy is transferred to the PVB interlayer.

Attenuation dispersion curve models for LSG with pummel number 3 and pummel number 8 are displayed in Figure 3.16. As expected, pummel number 8 dispersion model experiences much higher attenuation at resonant frequencies. It has been shown that the amount of attenuation attributed to absorption in the PVB interlayer as opposed to attenuation due to energy leakage to surrounding layers is more prevalent at higher frequencies [74]. Therefore, the S2 wave mode shows reasonable potential for UT attenuation measurements with an excitation frequency comparable to the resonant frequency of 2.25 MHz.
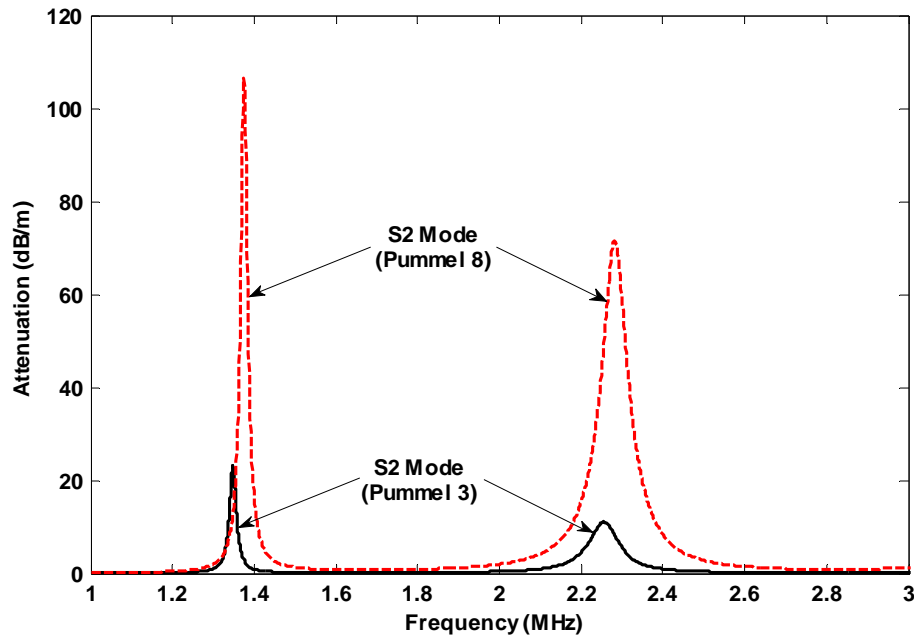
Figure 3.16: Attenuation dispersion curves of the S2 wave mode for pummel number 3 (solid black curve) and pummel number 8 (dashed red curve) models (See Tables 3.1 and 3.2 for material properties and spring constants).

3.3.2   SENSITIVITY ANALYSIS: ENERGY VELOCITY DISPERSION CURVES FOR VARIOUS MATERIAL PROPERTIES AND SPRING CONSTANTS

LSG specimens were provided by Ceralink Inc. for UT. The adhesion level and material properties of the glass and PVB interlayer were not disclosed. Dispersion curve models, as well as spring constant values, are highly dependent on material properties of glass and PVB. Therefore, different material parameters of glass and PVB were altered to examine the effect each variable had on the guided wave behavior in LSG. The thickness of the glass and PVB interlayer were measured and used for each model.

In general, the density and Poisson's ratio of float glass and PVB used in LSG have little variation compared to Young's modulus between different manufacturers. Therefore, density and Poisson's ratio are left unchanged and the stiffness of the float glass and PVB interlayer are investigated for this study. Changing the stiffness of laminate constituents requires an adjustment in spring constant values derived in the QSM. Consequently, dispersion curve models are very sensitive to deviations in stiffness for both glass and PVB. Various models are explored with modified Young's moduli to observe variations in energy velocity dispersion curves. In the

51

subsequent chapter, preliminary experimental UT energy velocity measurements are performed on the LSG specimens. Initial results are used to update the preliminary dispersion model by estimating new lamina stiffnesses.

The preliminary dispersion model (pummel number 3) described in the preceding section is used as a Reference Model for this study. Four adjusted dispersion models are prepared using QSM for pummel number 3 and compared to the Reference Model. Model 1 and Model 2 describe LSG with a 20% reduction and 20% increase in float glass stiffness, respectively. Young's modulus of the PVB interlayer is varied for the remaining two models. Model 3 has a 20% reduction in PVB stiffness, while Model 4 has a 20% increase in PVB stiffness. The variable parameters for each model are presented in Table 3.3. Apart from the adjusted lamina stiffnesses, each new model uses identical material parameters extracted from the preliminary Reference Model described in the previous section. Refer to Table 3.1 and 3.2 for material properties and spring constants used in the Reference Model.

Table 3.3: Modified Young's moduli for glass and PVB and spring constants for pummel number 3 dispersion models.

Model	E_g (GPa)	E_{PVB} (GPa)	K_n (N/m^3)	K_t (N/m^3)
Reference	72	3.9	6.8785 E+11	2.4091 E+11
1	57.6	3.9	6.7864 E+11	2.3769 E+11
2	86.4	3.9	6.9413 E+11	2.4312 E+11
3	72	3.12	5.5632 E+11	1.9485 E+11
4	72	4.68	8.1655 E+11	2.8599 E+11

Energy velocity dispersion curves of the S0, S1 and A1 wave modes are presented for each adjusted model (dotted curves) along with the preliminary Reference Model (solid curves) in Figures 3.17 - 3.20.

52
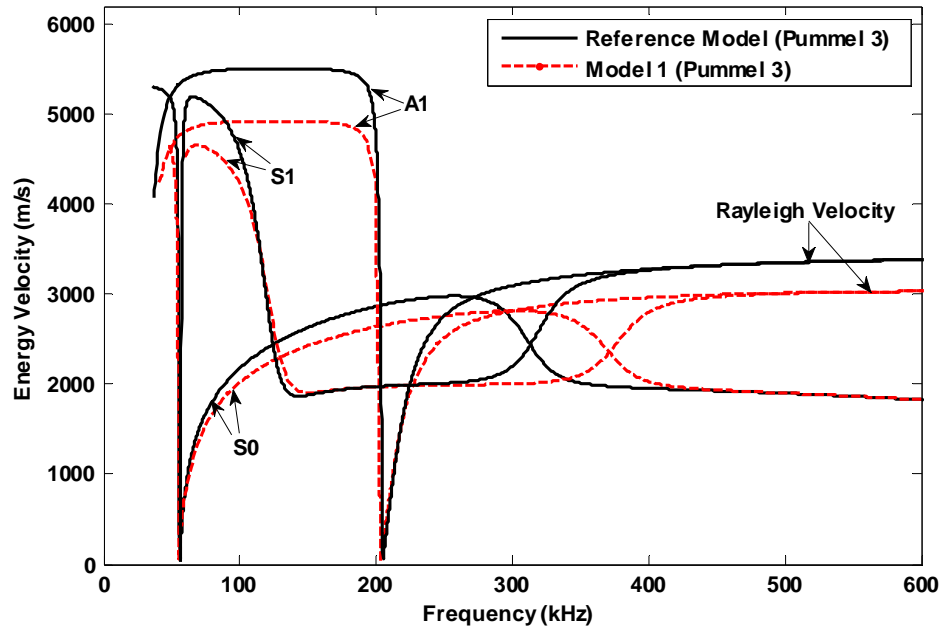
Figure 3.17: Energy velocity dispersion curves of Reference Model (solid black curves) and Model 1 (dashed red curves) adjusted for 20% *reduction* in glass stiffness (For material properties and spring constants, see Tables 3.1 and 3.2 for Reference Model and Tables 3.3 and 3.4 for Model 1). The Rayleigh velocity is shown for each model.
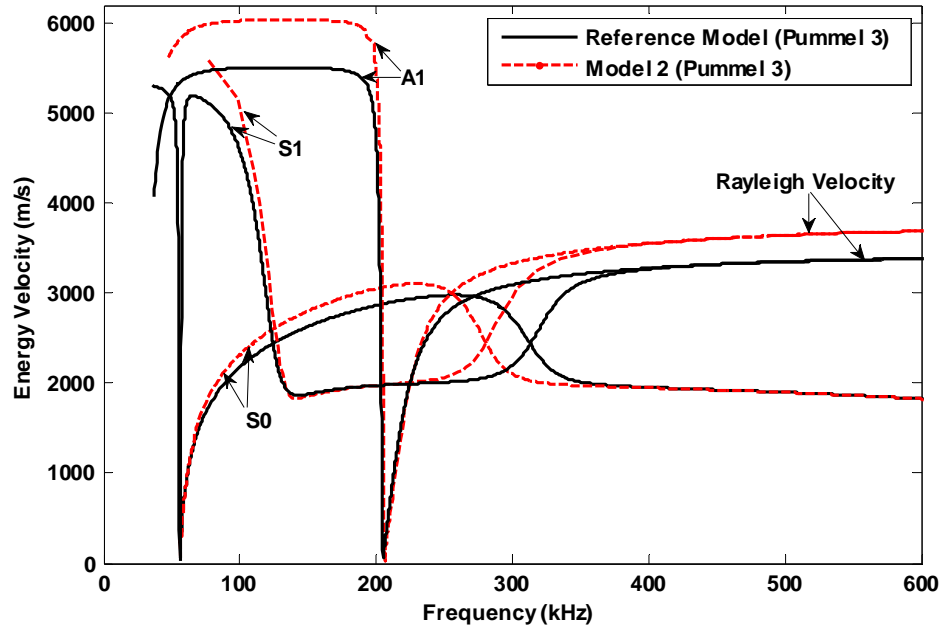
Figure 3.18: Energy velocity dispersion curves of Reference Model (solid curves) and Model 2 (dashed curves) adjusted for 20% *increase* in glass stiffness (For material properties and spring constants, see Tables 3.1 and 3.2 for Reference Model and Tables 3.3 and 3.4 for Model 2). The Rayleigh velocity is shown for each model.

A relationship exists between the adjusted float glass stiffness values in Models 1 and 2 and the resulting energy velocity curves. At higher frequencies (> 400 kHz), the A1 and S1 wave modes approach the Rayleigh or bulk velocity. These modes remain at this velocity for increasing frequencies where most of the energy is concentrated along the surface of the laminate (see Figure 3.7 and 3.13). As Young's modulus of float glass was varied, the Rayleigh velocity shifted toward higher and lower energy velocities as seen in Figures 3.17 and 3.18, respectively. The direct relationship between Young's modulus and bulk wave velocity is expressed in Equation 2.11 and 2.13. In addition to the shifted Rayleigh velocity, the S0 and S1 mode energy velocity curves exhibit a shift in frequency in the regions where the two wave modes modulate energy between the outer glass plates and the PVB interlayer. At the moment, this phenomenon is neglected but will be elaborated on in Chapter 4.

Models 3 and 4 demonstrate more drastic variations in resulting energy velocity dispersion curves. As seen in Figures 3.19 and 3.20, changes to the PVB interlayer stiffness resulted in dispersion curves shifting in energy velocity. The energy velocity of the S0 and S1 wave modes become faster or slower with increases or decreases in PVB stiffness, respectively. It is worth noting that the energy velocity only affects the S0 and S1 wave modes in regions where most of the wave energy is concentrated in the PVB interlayer. Recall Figures 3.10 and 3.12 for the power flow profiles of the S0 and S1 wave modes at such frequencies. Additionally, the region where the energy is transferred from the outer glass layers to the PVB interlayer shifts toward higher or lower frequencies for increases or decreases in PVB stiffness, respectively.

After carefully analyzing the four adjusted dispersion curve models, the A1 and S0 modes were selected for preliminary UT energy velocity measurements with an excitation frequency of 500 kHz. Resulting experimental energy velocities provide insight to the float glass and PVB interlayer stiffness in the LSG specimens. Updated dispersion curve models are then traced for different pummel numbers, and additional energy velocity and attenuation measurements are performed to help characterize the adhesive bond in each laminated specimen.
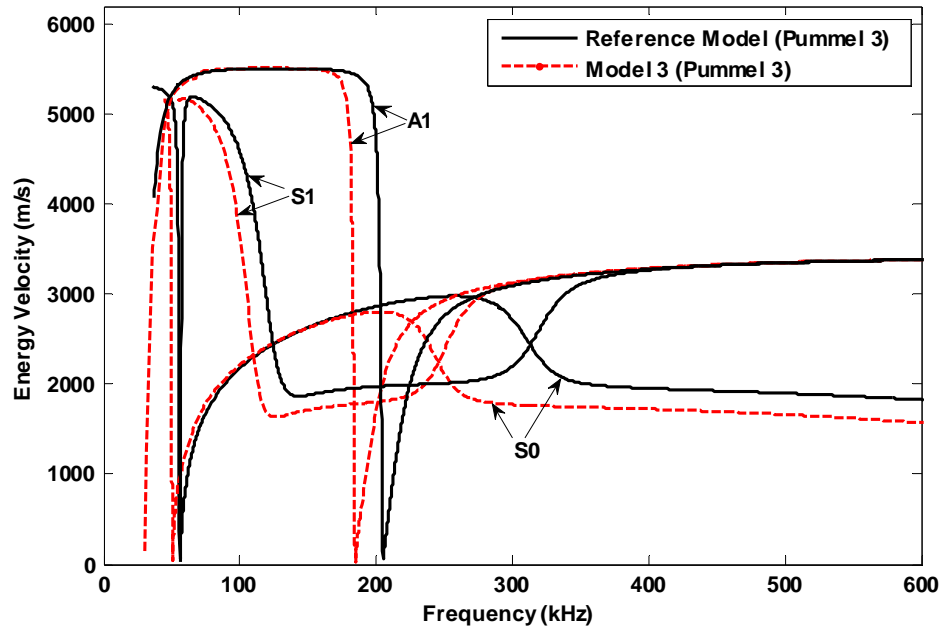
Figure 3.19: Energy velocity dispersion curves of Reference Model (solid curves) and Model 3 (dashed curves) adjusted for 20% *reduction* in PVB stiffness (For material properties and spring constants, see Tables 3.1 and 3.2 for Reference Model and Tables 3.3 and 3.4 for Model 3).
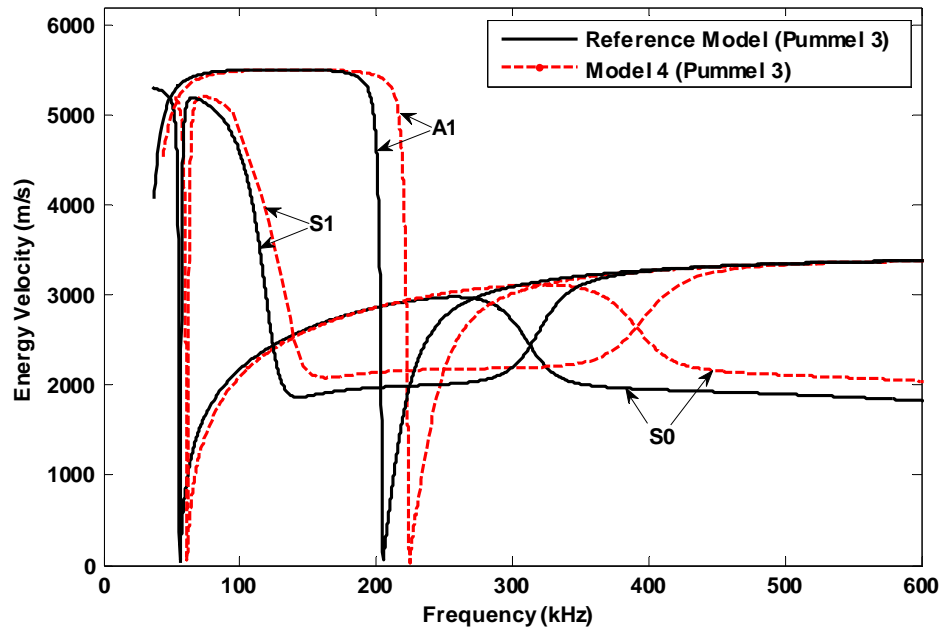
Figure 3.20: Energy velocity dispersion curves of the Reference Model (solid curves) and Model 4 (dashed curves) adjusted for 20% *increase* in PVB stiffness (For material properties and spring constants, see Tables 3.1 and 3.2 for Reference Model and Tables 3.3 and 3.4 for Model 4).

55

CHAPTER 4:

EXPERIMENTAL INVESTIGATION

Ultrasonic guided waves were used to examine laminated safety glass (LSG) specimens. Preliminary energy velocity measurements were used to estimate material properties of LSG constituents. Additional energy velocity and attenuation measurements were carried out and compared to revised analytical dispersion curve models with various pummel numbers. Correlations between revised analytical models and experimental measurements are discussed, and the adhesion level of each specimen is approximated.

4.1   SPECIMEN DESCRIPTIONS

Two groups of LSG specimens were prepared by Ceralink Inc. using a novel Fastfuse^{TM} radio frequency (RF) lamination technology. Specimens from each group contain a polyvinyl butyral (PVB) interlayer sandwiched between two float glass outer layers. Figure 4.1 illustrates the three-layered laminate system layup.
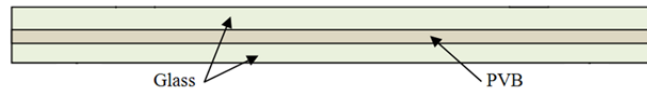
Figure 4.1: Layup of a three-layered laminated safety glass specimen.

All specimens contain identical float glass plates, while the PVB interlayer was varied between specimen groups. Group 1 specimens contain an automotive grade PVB interlayer, while Group 2 specimens contain a stiffer architectural grade PVB interlayer. Furthermore, different lamination processing variables were controlled for each group. Therefore, experimental results for each specimen group are analyzed independently.

4.1.1   SPECIMEN GROUP 1: AUTOMOTIVE GRADE PVB INTERLAYER

Six laminates with different lamination processing combinations were prepared for UT. Two variables were controlled during the lamination process for this study: RF lamination time and applied pressure during lamination. The RF lamination power was held constant for these specimens. Lamination processing parameters for each laminate in Group 1 are displayed in Table 4.1.

Table 4.1: Lamination processing variables for Specimen Group 1.

Specimen Label	Specimen #	RF Lamination Time (s)	Applied Pressure (psi)
A	1680_3	40	50
B	1681_3	55	50
C	1697_2	70	50
D	1694_2	40	100
E	1695_2	55	100
F	1696_2	70	100

4.1.2 SPECIMEN GROUP 2: ARCHITECTURAL GRADE PVB INTERLAYER

Specimens in Group 2 contain an architectural grade PVB interlayer with a higher elastic modulus than the automotive grade PVB interlayer from Group 1. Table 4.2 exhibits the lamination processing variables for Group 2. RF lamination time and cooling time under pressure were varied, while the RF lamination power and pressure were held constant.

Table 4.2: Lamination processing variables for Specimen Group 2.

Specimen Label	Specimen #	RF Lamination Time (s)	Cooling Time (min)
AA	1792	40	0
BB	1793	40	5
CC	1794	55	0
DD	1795	55	5

4.2 ENERGY VELOCITY MEASUREMENTS

Ultrasonic energy velocity measurements were performed on each laminate from specimen Groups 1 and 2, using the experimental setup and procedure described in the following section. As described in Chapter 3, material properties and adhesion levels of the laminated specimens were not disclosed. As a result, initial energy velocity measurements were performed on Group 1 specimens to determine the Rayleigh velocity of the laminates and energy velocity of the S0 wave mode. Partial wave energy velocities were compared to the reference dispersion curve model from Chapter 3 and used to approximate the stiffness of the outer float glass plates and PVB interlayer. A revised dispersion curve model was then developed. Additional energy velocity measurements were carried out and compared to the revised dispersion model to estimate the adhesion level of each laminated specimen.

Similar energy velocity measurements were performed on Group 2 specimens. The revised dispersion model for Group 1 specimens was adjusted for an increase in stiffness of the architectural PVB interlayer. Experimental results are divided into two sub-sections corresponding to each specimen group. Correlations between experimental energy velocity measurements and analytical dispersion curve models are discussed for each specimen group.

4.2.1 EXPERIMENTAL SETUP AND PROCEDURE

Energy velocity measurements were taken using an indirect through-transmission UT approach with sending and receiving transducers located on the same side of the specimen. An illustration of this arrangement, including the digital signal processing (DSP) equipment used for testing, is shown in Figure 4.2. The DSP hardware used for UT included: Ritec RPR-4000 pulser/receiver, Ritec RT-150 through load, Krohn-hite 3945 analog filter/amplifier, HP 54600A digital oscilloscope and an AD1200 analog-to-digital converter. The DSP equipment was connected via BNC connector cables. The entire system was controlled remotely with LabVIEW software, and collected data was analyzed using MATLAB software.
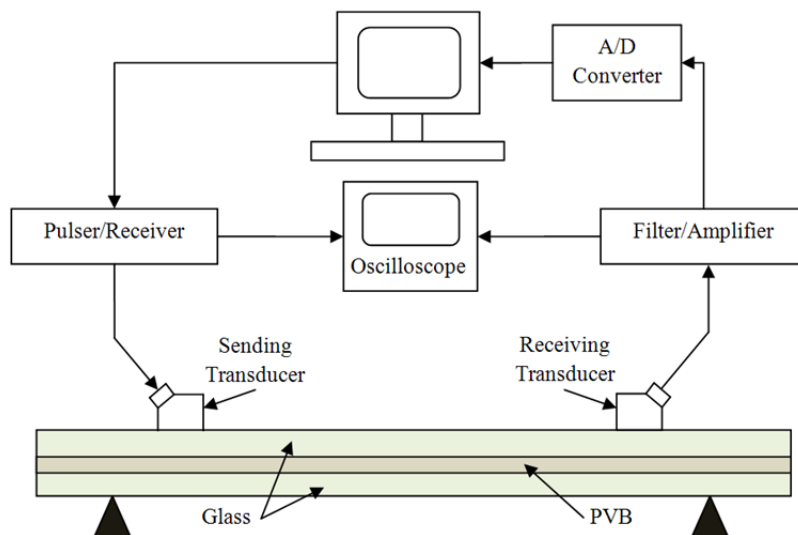
Figure 4.2: Schematic diagram of UT equipment and indirect through-transmission approach.

Before experimental testing was performed, an appropriate stand and transducer holder system were assembled to ensure consistent testing conditions. Shown in Figure 4.3, a stand constructed with only three points of contact near the outer edges of the specimen was used to support the laminated specimens for UT. Nominal contact between the stand and specimens ensured minimal energy leakage.

58

Figure 4.3: Laminated specimen supported by testing stand with three contact points.

Panametrics longitudinal angle beam transducers (model V413, 0.5/0.5x1.0) with a central frequency of 500 kHz were used for this experiment. They were designed to connect to accompanying Plexiglas angle beam wedges to allow for oblique angles of incidence from 0^0 to 60^0. As seen in Figure 4.4, the transducers and angle beam wedges are connected to custom made holders designed using Autodesk Inventor and molded using a Dimension sst1200 3D printer. The distance between transducers was controlled by connecting each of the custom holders to a metal bar, which is shown in Figure 4.5.
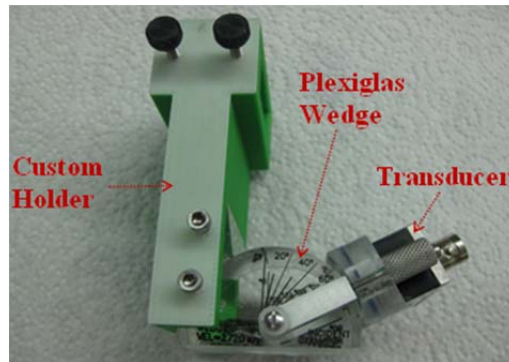
Figure 4.4: Ultrasonic transducer, angle beam wedge and transducer holder system.

Figure 4.5: Transducer holder system on bar used to control transducer separation distance.

For each test, a laminate was placed on the testing stand. Soundsafe ultrasonic couplant was applied at the interfaces of the transducers, angle beam wedges and laminates to ensure proper transfer of acoustic wave energy. The transducer holder system was placed on a laminate and the separation distance between the sending and receiving transducers was held constant for each test. A 60° angle of incidence was chosen to eliminate specific wave modes by means of Snell's law (see Appendix C for details). For each test, a weight was placed on top of the transducer holder system to maintain a constant saturation pressure between the angle beam wedge and laminate surface. Ultrasonic signals were sent from one transducer and received by the other. The entire energy velocity testing setup including stand, laminate, transducer holder system and weight is shown in Figure 4.6.
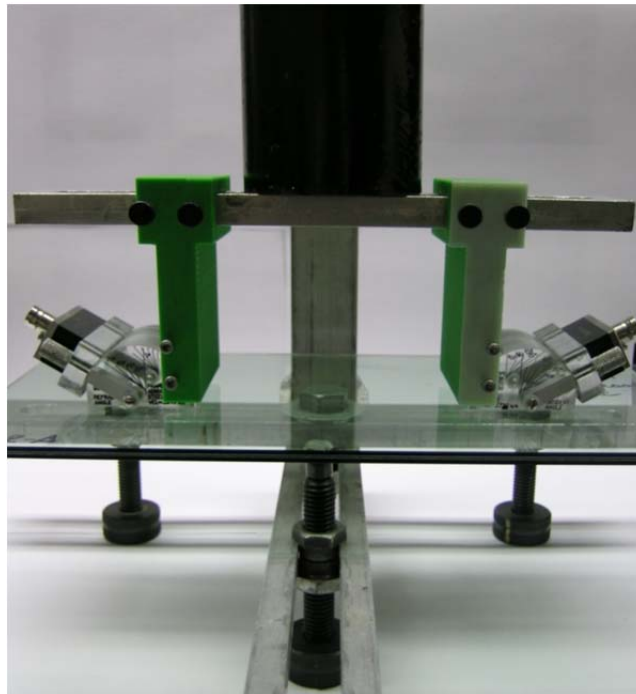
Figure 4.6: Ultrasonic testing setup for energy velocity measurements.

Due to the presence of partial wave mode interference in the LSG specimens, a threshold energy velocity method was used for UT, where only a distinct arrival time of one partial wave was necessary for energy velocity calculations. A reference signal was used to eliminate any system delay and to neglect the travel time through the Plexiglas wedges. The reference signal was acquired by collecting waveforms with the sending and receiving transducers (with angle beam wedges attached) applied face-to-face, as shown in Figure 4.7.

Figure 4.7: Face-to-face reference signal used for energy velocity measurements.

The time of flight of the reference signal (see Figure 4.8b) was subtracted from the time of flight of the original signal (see Figure 4.8a) to obtain the time of flight through only the laminates themselves (see Figure 4.8c).
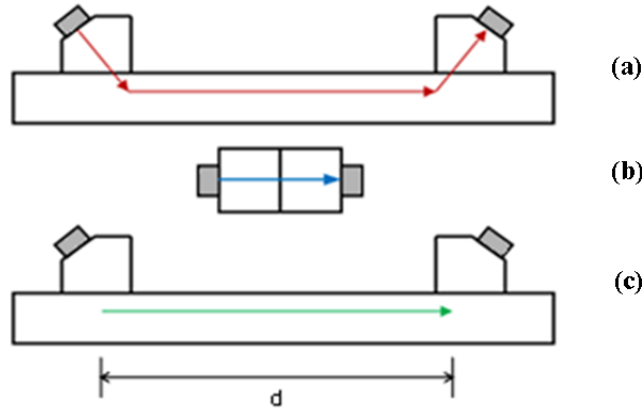
Figure 4.8: Acoustic wave path through (a) entire system, (b) reference and (c) laminate.

The arrival times of each waveform signal were determined by the first amplitude point exceeding a threshold limit. A specific percentage of the maximum peak waveform amplitude was designated the threshold limit in this study. Figure 4.9 illustrates a typical threshold limit set to 50% of the maximum waveform amplitude. The corresponding arrival times for a typical reference and laminate waveform are shown as well. The energy velocity is calculated from these arrival times as follows,

$$V = \frac{d}{(t - t_{ref})} \dots\dots\dots\dots\dots\dots\dots\dots\dots\dots\dots\dots\dots\dots\dots\dots\dots\dots\dots\dots(4.1)$$

where d represents the separation distance between sending and receiving transducers. The arrival times of the reference and laminate waveforms are denoted by t_{ref} and t, respectively.

61
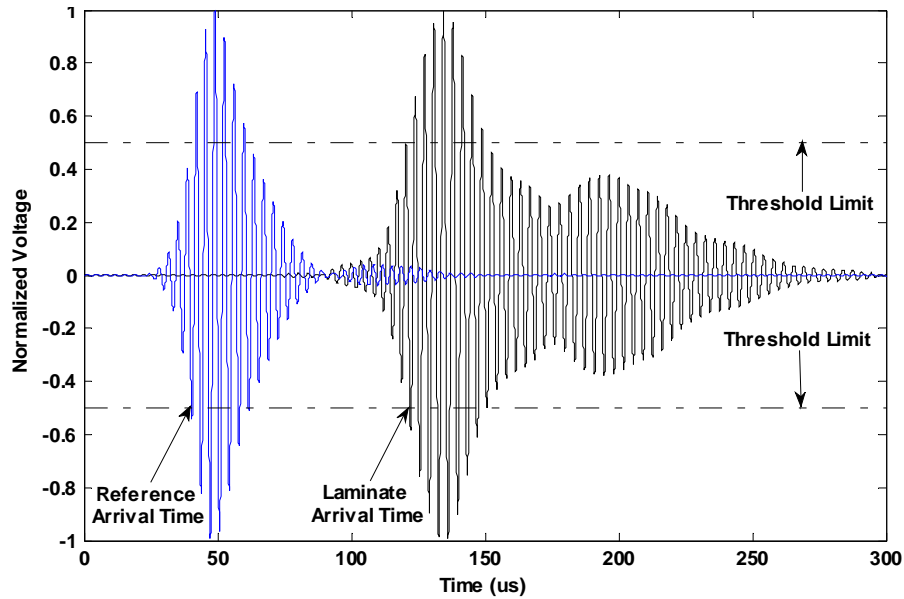
Figure 4.9: Typical normalized time signal waveform of a reference (blue waveform) and laminate (black waveform) measurement. Arrival times are denoted by the first data point exceeding the threshold limit (dashed black line).

Preliminary energy velocity measurements were taken to help characterize the material properties of the LSG specimens from Group 1. Specific UT parameters are presented in the following section. After initial UT, additional energy velocity measurements were taken on laminates from specimen Groups 1 and 2, which are displayed in Tables 4.1 and 4.2, respectively. The experimental setup and UT parameters remained unchanged for each group of specimens. A separation distance of 210 mm was held constant between sending and receiving transducers and a threshold limit was set to 30% of the maximum peak of the A1 wave mode. A 60° angle of incidence was used to eliminate the A2 and S2 wave modes from the energy velocity wave envelope. An iterative program was developed using LabVIEW software to test a range of excitation frequencies. Measurements were taken at 5 kHz increments from excitation frequencies of 250 kHz to 500 kHz (51 total iterations). A sliding 20 kHz Butterworth bandpass analog filter, centered about the respective excitation frequency, was applied to each test. One sine wave tone burst was used for each excitation pulse, which was averaged 20 times to eliminate any adverse system noise. A sampling frequency of 50 MHz was used, and 15,000 data points were collected for each iteration/test. Five independent tests were performed at each excitation frequency for each laminate. All other testing parameters were held constant for all tests. Experimental results are presented and adhesion levels of the LSG specimens from each group were estimated.

62

4.2.2   REVISED ANALYTICAL ENERGY VELOCITY DISPERSION MODEL

Laminated Specimen B was arbitrarily selected from Group 1 for initial UT. A separation distance of 220 mm between sending and receiving transducers was chosen to allow ample time for wave modes to separate. A 60° angle of incidence was used to eliminate the A2 and S2 wave from the energy velocity wave envelope. The peak threshold method was employed for this experiment to determine the energy velocity of the A1 and S0 wave modes at 500 kHz. The arrival time of each wave mode was denoted by the maximum data point in the respective wave envelopes. A total of 15,000 data points were collected with a sampling frequency of 50 MHz. A single sine wave tone burst was averaged 20 times and sent from the pulser/receiver. A 20 kHz Butterworth bandpass analog filter was centered around 500 kHz and applied to each test. Five independent energy velocity measurements were taken for the A1 and S0 wave modes for testing reliability. Results are discussed and an updated analytical dispersion model is presented.

To help visualize the expected ultrasonic waveform, a simulated signal was modeled using Disperse software. Figure 4.10 displays the simulated signals of the A1, S0 and S1 wave modes at 500 kHz for pummel number 3 dispersion model. The first envelope corresponds to the superposition of the A1 and S1 wave modes approaching the Rayleigh velocity. Most of the signal energy is concentrated in these modes and the arrival time is clearly noticeable. The second wave envelope is more complex. Although very little surface displacement and energy exist within the S0 mode at 500 kHz, the partial wave is still visible in the simulated signal (Figure 4.10b). The arrival time of the S0 mode is less distinguishable though, making the energy velocities more difficult to calculate with confidence.

The time signal waveform and corresponding amplitude spectrum of an initial experimental measurement are shown in Figure 4.11. The reference signal (blue waveform) was obtained from face-to-face measurements as described in the experimental procedure. Two main wave envelopes exist within the laminated specimen time signal (black waveform) as expected. Experimental signals are in good agreement with simulated ultrasonic signals modeled in Disperse.

63
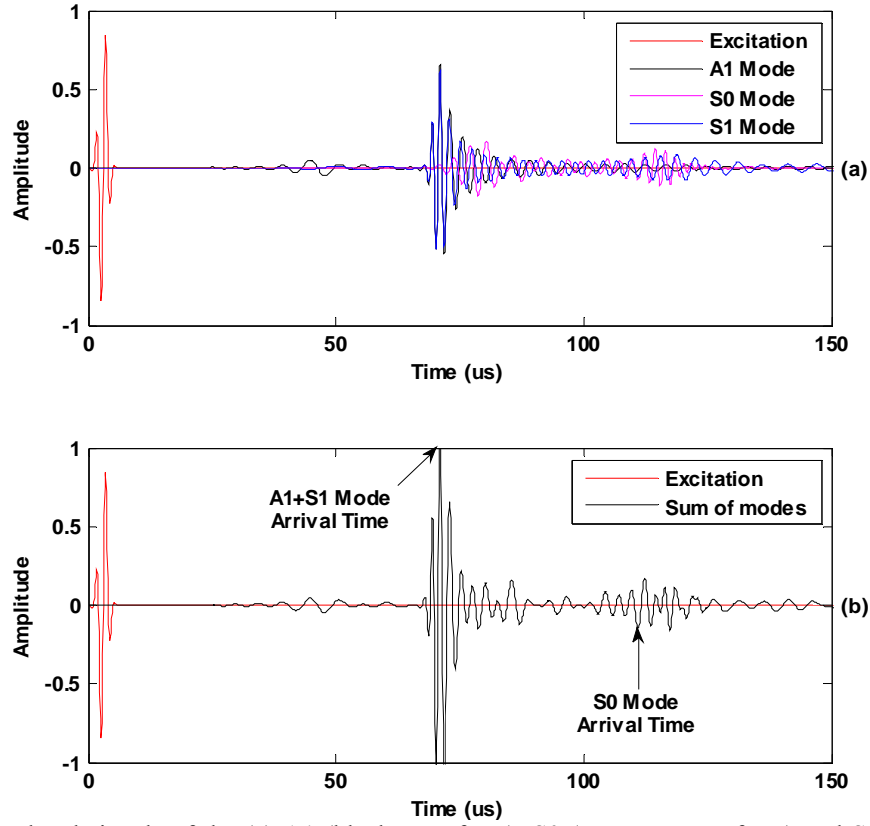
Figure 4.10: Simulated signals of the (a) A1 (black waveform), S0 (magenta waveform) and S1 (blue waveform) partial wave modes and (b) sum of A1, S0 and S1 wave modes for the pummel number 3 dispersion model at 500 kHz (See Tables 3.1 and 3.3 for material properties and spring constants).
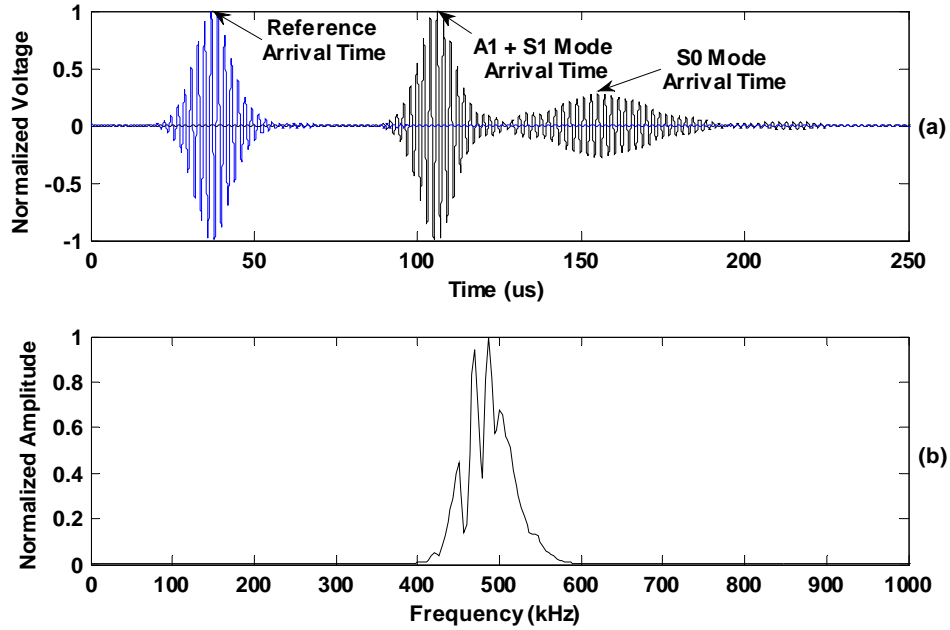
Figure 4.11: (a) Time signal of reference (blue) waveform and laminate (black) waveform and corresponding (b) amplitude spectrum of laminate signal.

The resulting energy velocities of the A1/S1 and S0 wave modes are plotted in Figures 4.12 and 4.13, respectively. The average of the five measurements along with error bars corresponding to two standard deviations (95% confidence interval) are shown as well.
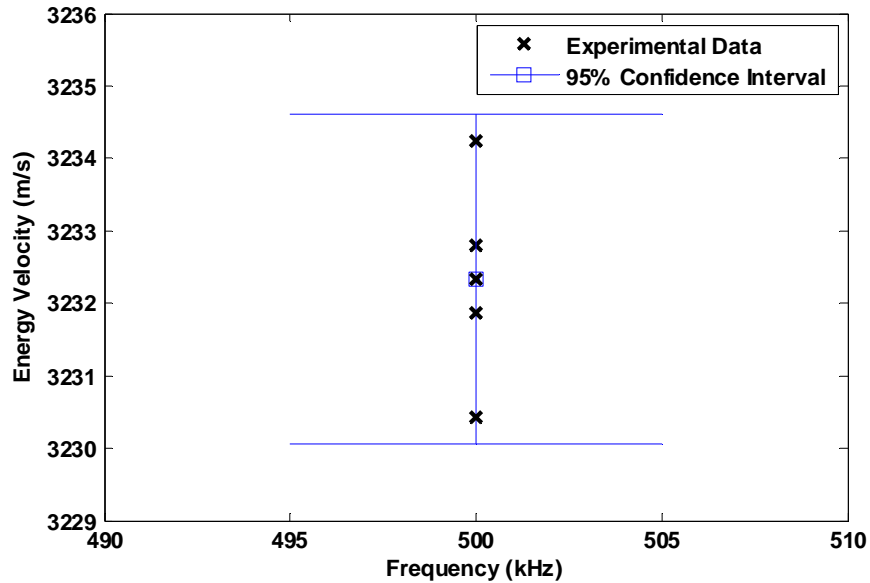
Figure 4.12: Five independent energy velocity measurements of the A1/S1 mode for Specimen B at 500 kHz. Error bars of 95% confidence are displayed with the experimental mean value.
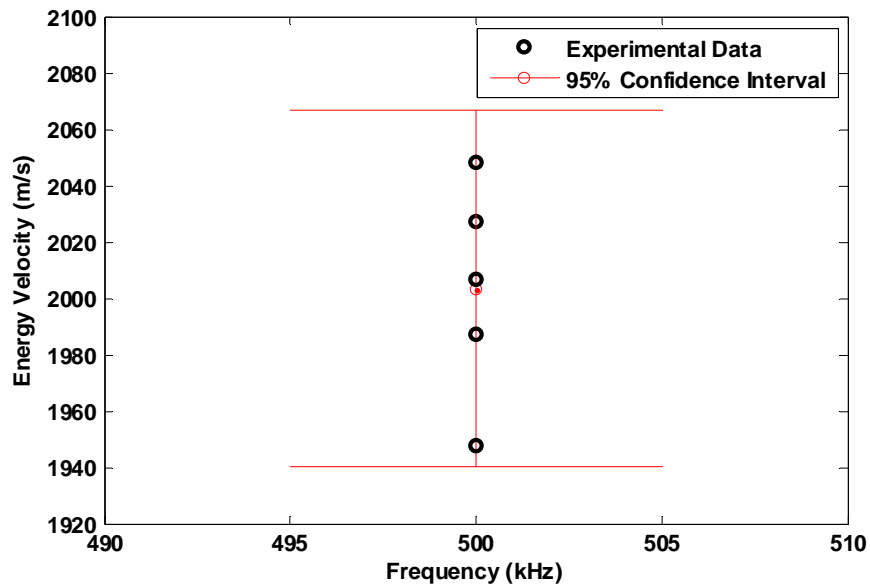
Figure 4.13: Five independent energy velocity measurements of the S0 mode for Specimen B at 500 kHz. Error bars of 95% confidence are displayed with the experimental mean value.

The five energy velocity measurements of the A1/S1 mode show very little variance and are believed to correspond to the Rayleigh velocity of the LSG specimens. Energy velocity measurements of the S0 mode show greater error between independent tests, which is likely due to wave interference with residual wave mode energy. In addition, the displacement and power flow at the glass surface is much lower in the S0 mode compared to the A1 and S1 modes at 500 kHz. Consequently, much less energy is detected in the S0 mode for UT and the arrival time is less discernable. Nevertheless, all measurements fall within the confidence bounds and assumed acceptable to estimate the energy velocity of the S0 mode.

Using the experimental mean energy velocity measurements from each wave mode, the preliminary dispersion curve model described in Chapter 3 was revised. Float glass stiffness was reduced by 7% to account for a drop in the bulk energy velocity. In addition, the PVB interlayer stiffness was increased by 10% to raise the energy velocity of the S0 wave mode. Updated material properties and spring constants for the revised dispersion model are displayed in Tables 4.3 and 4.4, respectively.

Table 4.3: Material properties and dimensions of laminated safety glass constituents in the revised dispersion model for specimen Group 1.

	Thickness (mm)	Density (g/cm^3)	Young's Modulus (GPa)	Poisson's Ratio	Longitudinal Attenuation (Np/m)	Shear Attenuation (Np/m)
Float Glass	2.10	2.5	67	0.25	0	0
PVB	0.793	1.1	4.3	0.34	8.51	43.5

Table 4.4: Spring constants representing different levels of adhesion in the revised dispersion model for specimen Group 1.

Pummel Number	Normal Spring Constant (N/m^3)	Transverse Spring Constant (N/m^3)
1	2.7634 E+11	9.6787 E+10
3	7.5086 E+11	2.6299 E+11
4	9.7984 E+11	3.4318 E+11
5	1.1766 E+12	4.1211 E+11
6	1.6302 E+12	5.7098 E+11
8	1.8570 E+12	6.5039 E+11

The experimental mean energy velocity measurements for the A1 and S0 wave modes are plotted with the revised dispersion curve model with pummel number 3 spring constants in Figure 4.14.
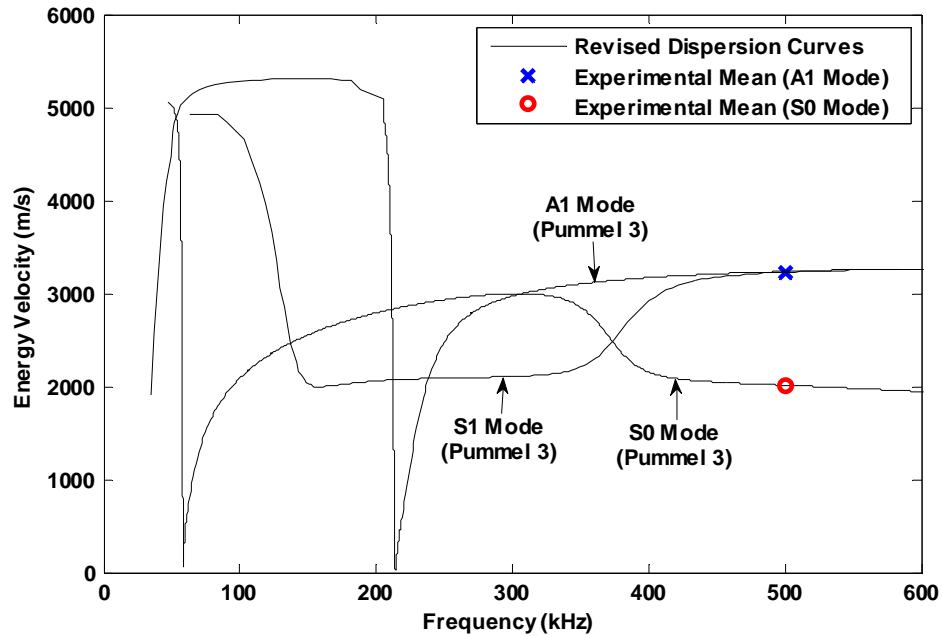
Figure 4.14: Revised dispersion curve model with pummel number 3 spring constants (See Tables 4.3 and 4.4 for material properties and spring constants) and experimental energy velocity measurements of the A1 and S0 wave modes for Specimen B.

After carefully studying the revised energy velocity dispersion curves, the first order antisymmetric (A1) wave mode was selected for additional UT. Although the energy velocity dispersion curve of the S0 mode appears faster than the A1 mode between 200 kHz and 300 kHz in the analytical model in Figure 4.14, the arrival time of the ultrasonic signal is dominated by the A1 wave mode. Supporting this phenomenon, a simulated ultrasonic signals for pummel number 3 dispersion model are presented in Figure 4.15 for the A1, S0 and S1 partial wave modes with an excitation frequency of 260 kHz. Theoretically, the S0 wave mode is traveling faster than the A1 wave mode around 260 kHz. Referring to Figure 4.15a, the A1 mode (black waveform) has less energy than the S0 mode (magenta waveform) but a faster arrival time. A similar trend was revealed for alternative pummel number models. Therefore, all experimental energy velocity measurements are expected to follow the A1 wave mode, if the threshold limit is set to a low percentage (e.g. 30%) of the maximum waveform amplitude.

67
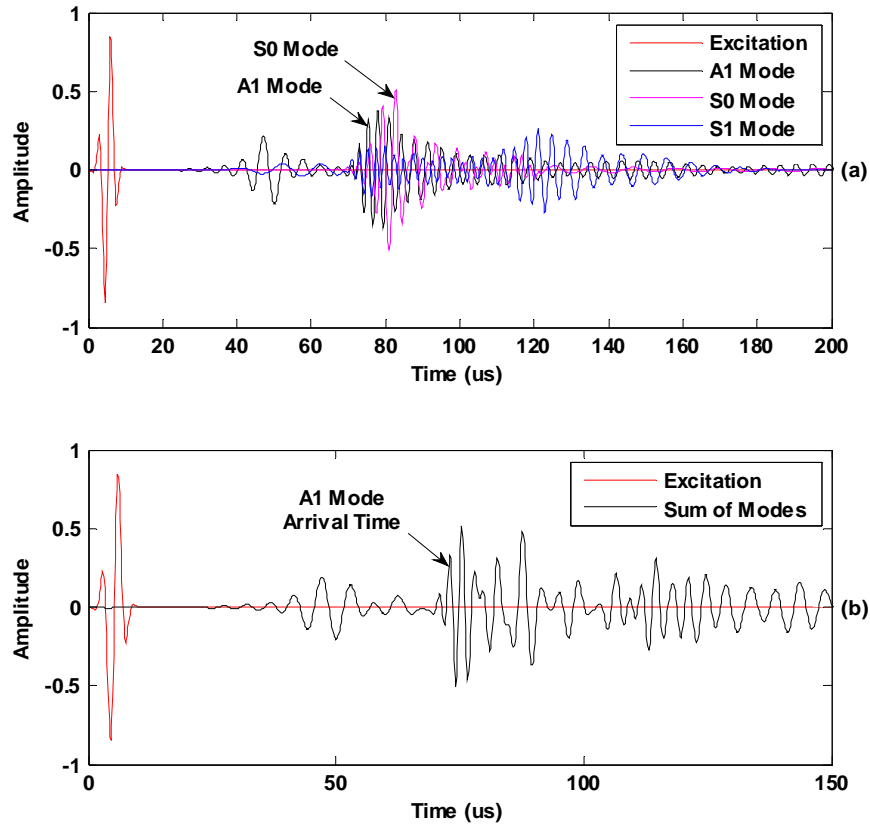
Figure 4.15: Simulated signals of the (a) A1 (black waveform), S0 (magenta waveform) and S1 (blue waveform) wave modes and (b) sum of A1, S0 and S1 wave modes for the pummel 3 dispersion model at 260 kHz (See Tables 4.3 and 4.4 for material properties and spring constants).

Energy velocity dispersion curves of the A1 wave mode for various pummel numbers (levels of adhesion) are presented in Figure 4.16. The frequency band of interest lies between 250 kHz and 500 kHz, as the A1 dispersion curve experiences a sharp drop in energy velocity in this range. The exact frequency location is highly dependent on the pummel number spring constants used in the analytical model as seen in Figure 4.16. As a result, the A1 wave mode shows good potential for determining the adhesion level of the laminated specimens in this region by matching experimental energy velocity data to the suitable pummel number model. In the succeeding section, additional energy velocity measurements were performed and related to the revised dispersion model.

68

Figure 4.16: Energy velocity dispersion curves of the A1 wave mode for different pummel number models (See Tables 4.3 and 4.4 for material properties and spring constants).

4.2.3 EXPERIMENTAL RESULTS

Experimental results are presented separately for specimen Groups 1 and 2, as the laminated specimens from each group contain different PVB interlayers as well as varying lamination processing combinations. Energy velocity measurements for Group 1 are compared to the revised analytical dispersion models from the preceding section, and laminate adhesion levels are estimated. After the first set of experimental UT was complete, destructive pummel tests were carried out on specimen twins from Group 1. The estimated adhesion levels from energy velocity measurements are compared to pummel test results to assess the integrity of the analytical dispersion model.

Recalling Figure 3.19 from the parametric study performed in Chapter 3, Group 2 energy velocity dispersion curves of the A1 wave mode are expected to shift toward higher frequencies due to increased PVB stiffness. The architectural grade PVB interlayer used for laminated specimens in Group 2 has an unknown increase in stiffness. Consequently, changes in energy velocity measurements may be attributed to an increase in PVB stiffness and/or an increase in laminate adhesion. As a result, experimental data from Group 1 and Group 2 are initially

69

compared to observe any differences in energy velocities. An estimated analytical dispersion model is then presented with an increase in PVB stiffness to account for the observed frequency shift. Conclusions from specimen Group 2 are more open-ended as additional laminate variables exist and supplementary pummel tests were not performed. A detailed discussion is presented with the resulting energy velocity measurements.

4.2.3.1 SPECIMEN GROUP 1: AUTOMOTIVE GRADE PVB INTERLAYER

A normalized reference waveform is presented in Figure 4.17a. The corresponding amplitude spectrum that describes the frequency content present within the waveform is shown in Figure 4.17b, which was calculated via fast Fourier transform (FFT). Similarly, the normalized laminate waveform and amplitude spectrum are shown in Figure 4.18. The first wave envelope in Figure 4.18a is the A1 wave mode. The S0 wave mode has much less energy and occurs later in time. Additional wave energy interferes with the S0 wave mode for each frequency iteration, although the S0 mode is not of significance for this study.
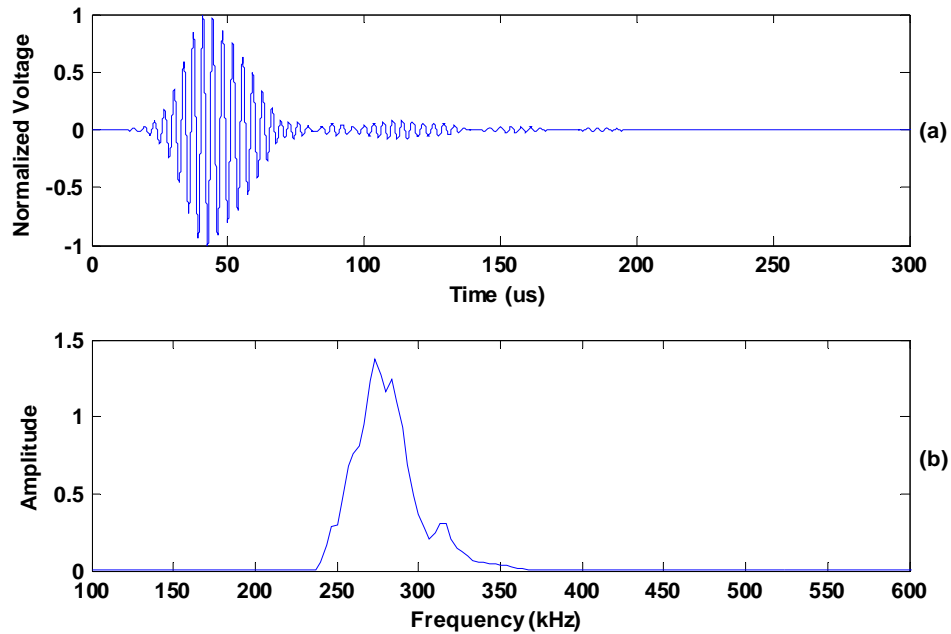
Figure 4.17: Ultrasonic reference signal (face-to-face) with an excitation frequency of 280 kHz in the (a) time domain and (b) frequency domain.
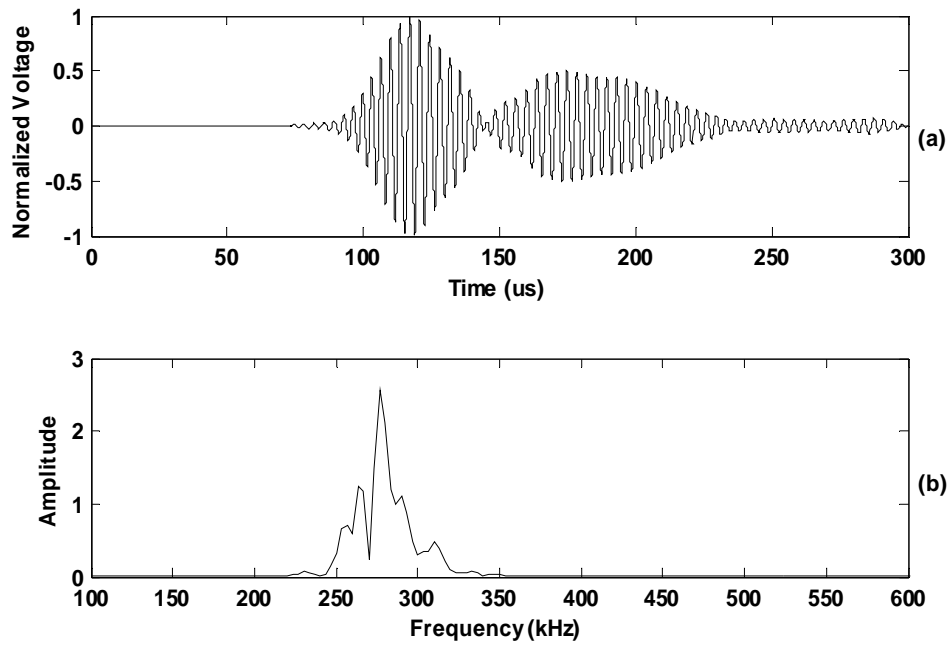
Figure 4.18: Ultrasonic signal through laminated Specimen B with an excitation frequency of 280 kHz and a separation distance of 210 mm between sending and receiving transducers in the (a) time domain and (b) frequency domain.

Arrival times of the A1 wave mode were used to calculate the energy velocity at each frequency iteration using Equation 4.1. Five independent energy velocity measurements for each specimen in Group 1 were averaged at each frequency iteration and plotted on top of pummel number 3 dispersion curves in Figure 4.19. All of the laminated specimens in Group 1 reveal similar energy velocity measurements over the entire frequency band of interest. Consequently, it is believed that all laminates in specimen Group 1 exhibit the same level of adhesion. Additionally, data from each specimen tends to follow the A1 wave mode as predicted from the simulated ultrasonic signal in Figure 4.15. Since a relatively low threshold limit was set, the arrival time of the A1 wave mode was detected as a result. The correlation between experimental measurements for Specimen B and the A1 wave mode of the revised dispersion curve model for pummel number 3 is noticeable in Figure 4.20.

71

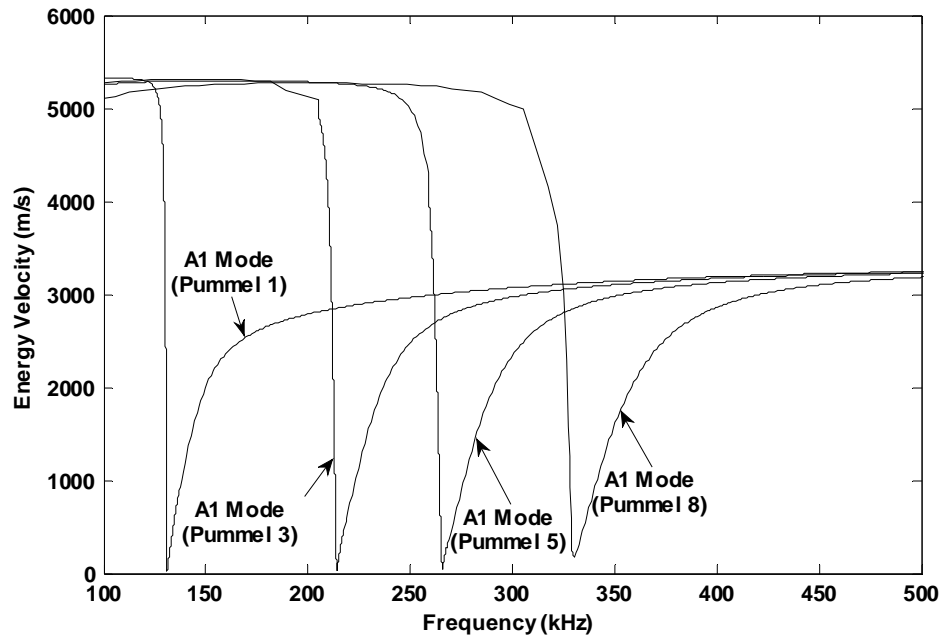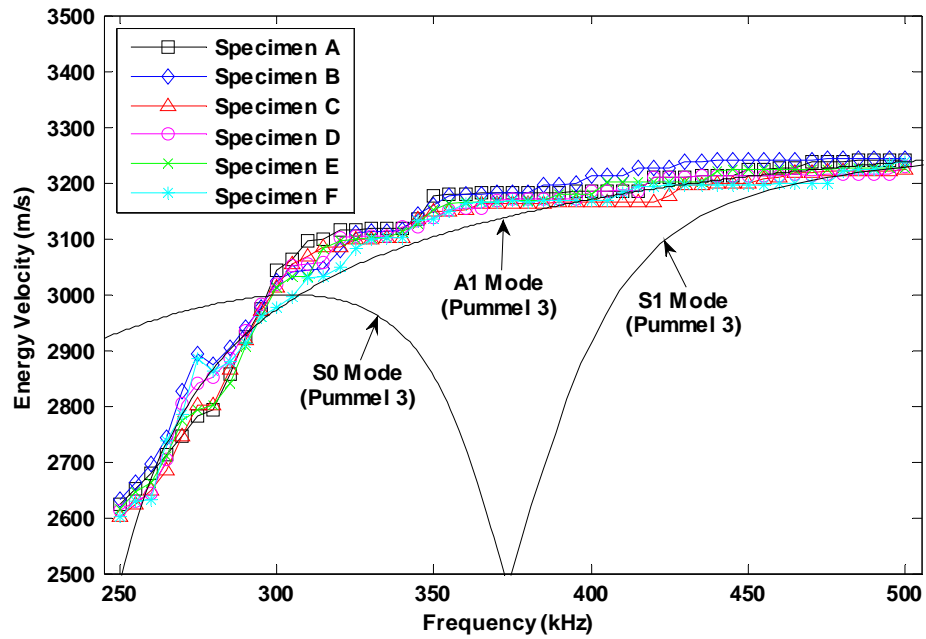**Figure 4.19:** Experimental mean energy velocity measurements for each specimen in Group 1 superimposed on revised analytical dispersion curve model with pummel number 3 spring constants (See Tables 4.3 and 4.4 for material properties and spring constants).
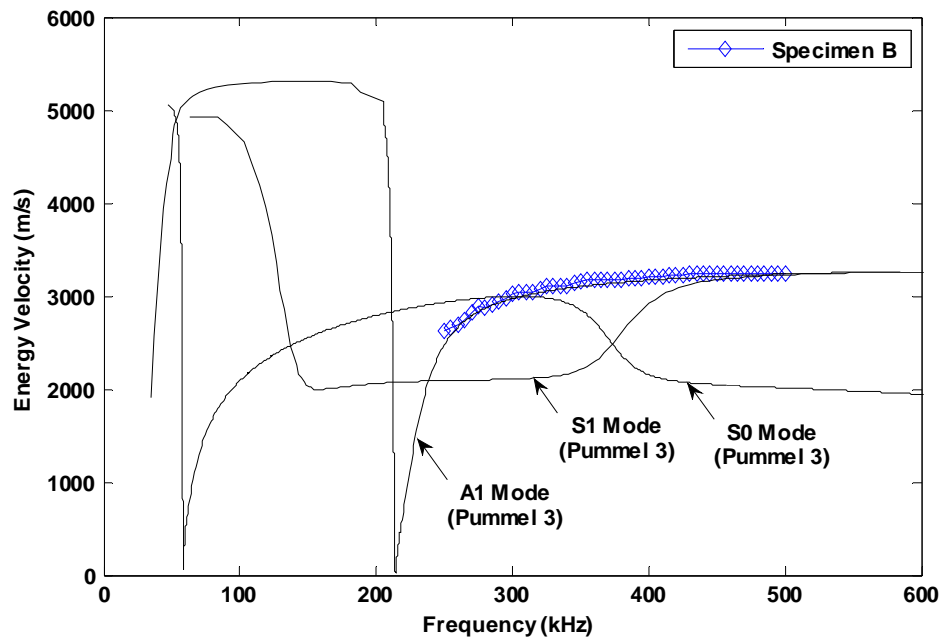
Figure 4.20: Experimental mean energy velocity measurements for laminated Specimen B from specimen Group 1 superimposed with revised analytical dispersion curve model with pummel number 3 spring constants (See Tables 4.3 and 4.4 for material properties and spring constants).

The experimental mean of the five independent measurements at each frequency iteration for Specimen B is plotted with 95% confidence intervals in Figure 4.21. Experimental measurements show nominal error at most frequencies. Measurements that approach the Rayleigh velocity are very accurate, since the A1 and S1 modes have completely converged into one wave envelope. Greater error occurred in regions where two wave modes converge or diverge from one another. Due to multiple wave modes interfering at lower frequencies, the arrival time of the A1 mode was likely distorted, creating discrepancies between independent measurements.
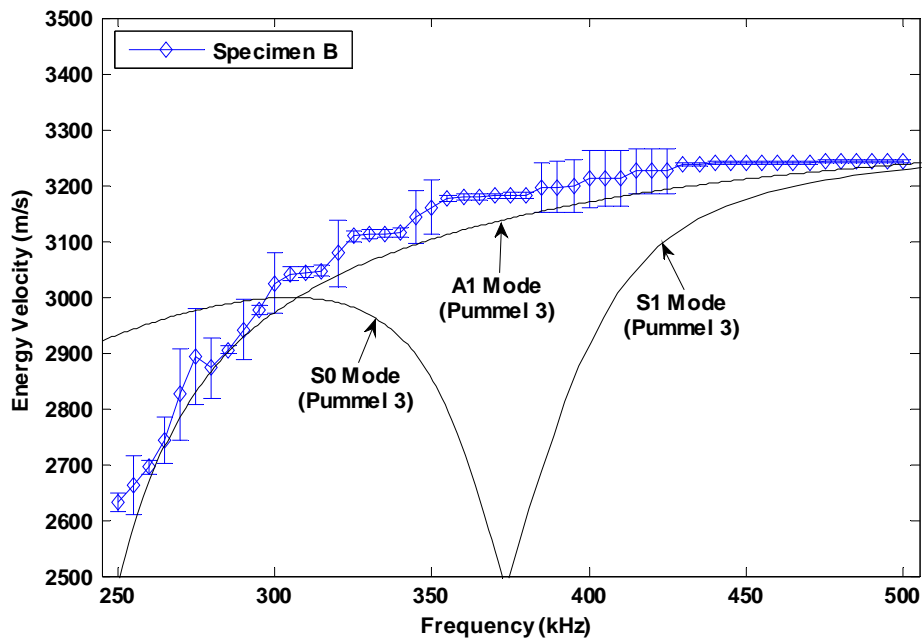
Figure 4.21: Experimental mean energy velocity measurements for laminated Specimen B from specimen Group 1 superimposed with revised analytical dispersion curve model with pummel number 3 spring constants (See Tables 4.3 and 4.4 for material properties and spring constants). Error bars with 95% confidence are presented for each frequency.

Since all energy velocity measurements were carried out under identical testing conditions, it was determined that all specimens contain the same level of adhesion. Furthermore, all measurements lie along the A1 wave mode of the pummel number 3 dispersion curve model. Based off ultrasonic energy velocity measurements in conjunction with an approximated dispersion curve model, all LSG specimens from Group 1 are believed to have adhesion levels around or just under pummel number 3.

73

After experimental testing was complete, destructive pummel tests (described in Chapter 1) were carried out on identical specimens from Group 1. It was encouraging to find that experimental energy velocity results matched the pummel test results relatively well. As expected, pummel tests revealed the same pummel number for all laminates in specimen Group 1. The resulting adhesion level of the laminates fell between pummel number 1 and 2. Therefore, the experimental results overestimated the adhesion level by approximately one to two pummel numbers. Analytical energy velocity dispersion curve models can be adjusted to match pummel test results by increasing the PVB interlayer stiffness and/or decreasing the PVB density. Too many variables already exist in the present model. Therefore making any adjustments to the further update analytical models lacks foundation and is out of the realm of this paper.

Since all of the laminated specimens revealed identical adhesion levels, no discernable relationship could be made on behalf of lamination processing variables and adhesion levels. At this time, it is believed that additional RF lamination pressure is needed to obtain higher adhesion levels for LSG specimens. If higher adhesion laminates are produced, a parametric study could be performed to discover how different lamination processing variables affect adhesion levels in LSG.

With limited knowledge of the laminated specimen characteristics, this study deemed quite successful in characterizing adhesion levels. Many assumptions were made in the development of the analytical dispersion curve models, which likely contributed as the main source of error in estimating the adhesive bond strength in LSG specimens. Additionally, pummel tests vary considerably from operator to operator making the pummel scale variable itself. The pummel scale only has resolution of around one half a pummel number, which takes a well-trained eye to discern. Supplemental testing is generally carried out to substantiate pummel tests for LSG. Overall, ultrasonic energy velocity measurements for specimen Group 1 show potential for estimating adhesion levels in LSG specimens.

4.2.3.2 SPECIMEN GROUP 2: ARCHITECTURAL GRADE PVB INTERLAYER

Experimental UT parameters remained unchanged for energy velocity measurements performed on Group 2 specimens. Review Table 4.2 for lamination processing variables for Group 2. Initially, resulting energy velocity measurements are compared to the analytical model developed for Group 1 specimens, to observe any changes in guided wave behavior. See Tables 4.3 and 4.4 for material properties and spring constants, respectively.

Normalized time signals and corresponding amplitude spectra are shown in Figures 4.22 and 4.23 for the reference and laminate waveforms, respectively. Similarly to Group 1 waveforms, the A1 wave mode corresponds to the first wave packet to arrive as seen in Figure 4.23a. Additional wave modes exist later in time but are more difficult to discern, as partial wave interference takes place. Again, these modes are not of interest for this study.
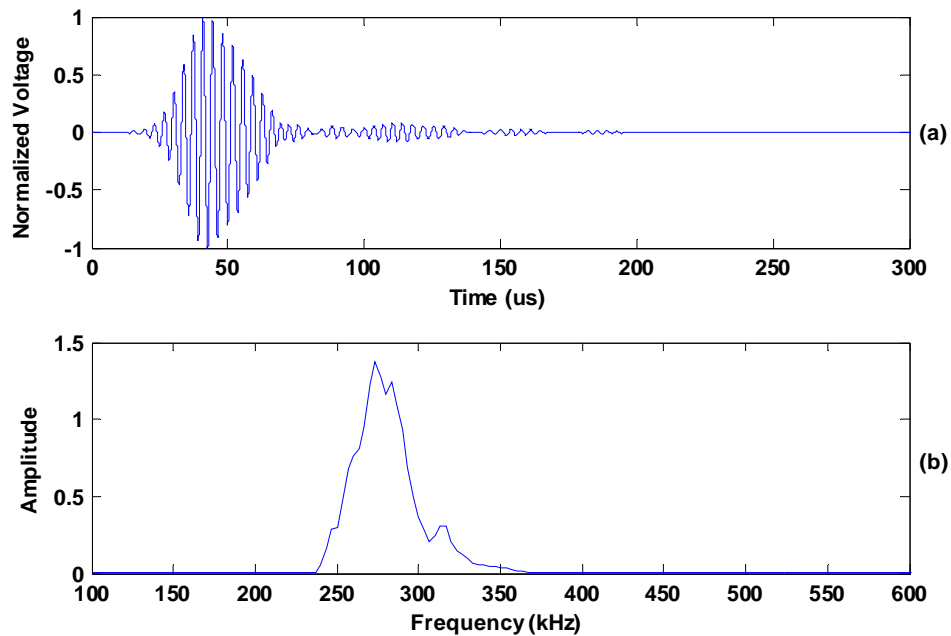
Figure 4.22: Ultrasonic reference signal (face-to-face) with an excitation frequency of 275 kHz in the (a) time domain and (b) frequency domain.
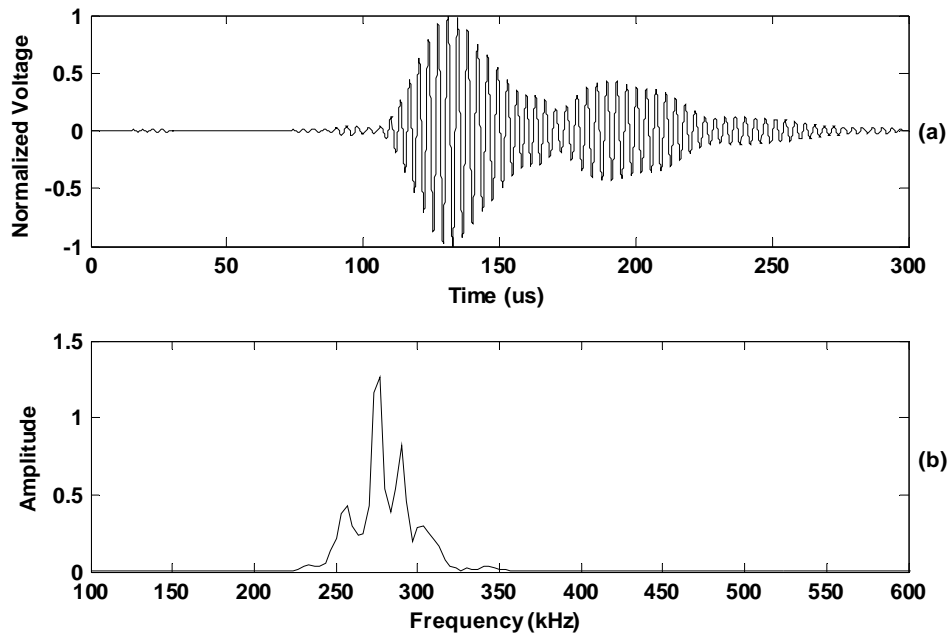
Figure 4.23: Ultrasonic signal through laminated Specimen DD with an excitation frequency of 275 kHz and a separation distance of 210 mm between sending and receiving transducers in the (a) time domain and (b) frequency domain.

Experimental mean energy velocity measurements for all laminates in specimen Group 2 are presented in Figure 4.24. The dispersion curve model developed for specimen Group 1 is also presented with pummel number 3 spring constants, in order to observe any variances in measurements between specimen groups. Similarly to Group 1 results, the experimental energy velocities for each laminate in Group 2 follow the A1 dispersion curve. In addition, differences in energy velocity measurements between each laminate are negligible. Therefore, all four laminates in Group 2 are believed to hold comparable adhesion levels. As expected, the energy velocity data shows a noticeable shift toward higher frequencies. It cannot be resolved whether the resulting shift is due to the increase in PVB stiffness and/or a stronger adhesive bond at the glass/PVB interface. To help characterize shift in frequency, experimental mean energy velocity measurements for laminated Specimen B from Group 1 and Specimen DD from Group 2 are presented in Figure 4.25. Since identical float glass was used for all laminates, it was encouraging to find similar Rayleigh velocities for specimens in Group 1 and 2. Furthermore, the initial energy velocity measurements used to predict the revised float glass stiffness were extremely consistent. Therefore, the float glass used for all LSG specimens has an estimated stiffness of 67 GPa.

76
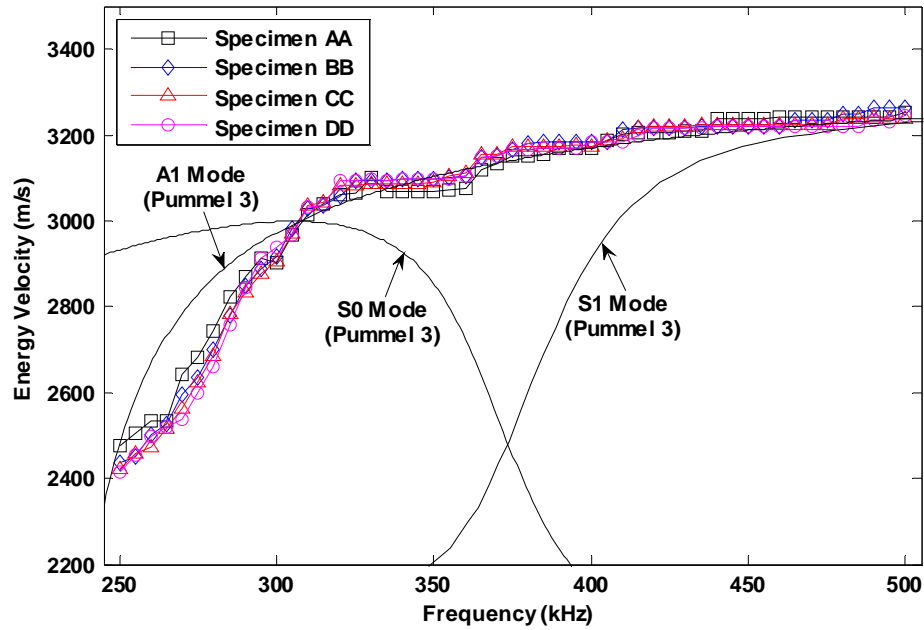
Figure 4.24: Experimental mean energy velocity measurements for all laminated specimens in Group 2. Analytical dispersion curve model from specimen Group 1 is presented with pummel number 3 spring constants (See Tables 4.3 and 4.4 for material properties and spring constants).
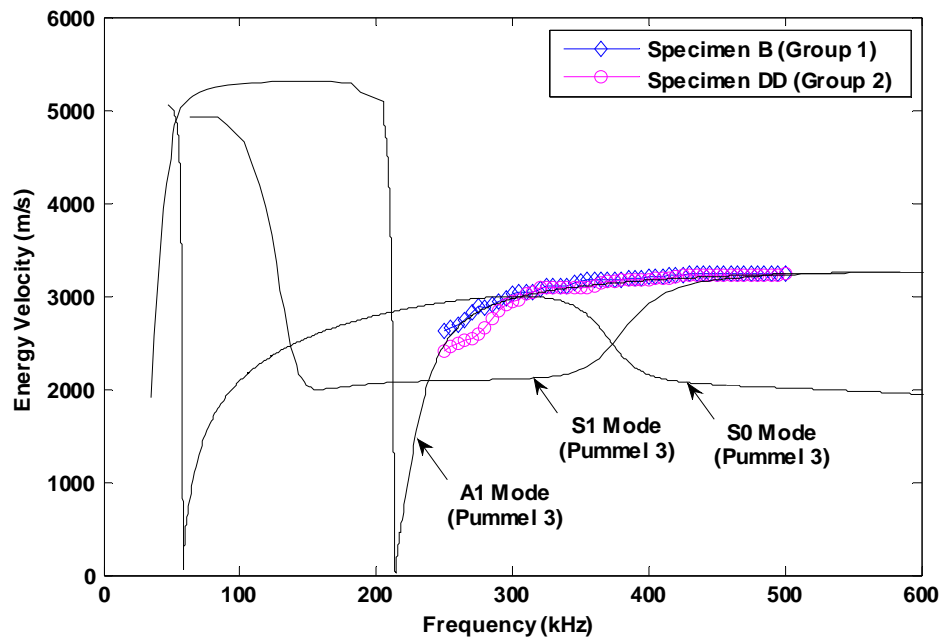
Figure 4.25: Experimental mean energy velocity measurements for laminated Specimen B and Specimen DD from specimen Groups 1 and 2, respectively. Analytical dispersion curve model from specimen Group 1 is presented with pummel number 3 spring constants (See Tables 4.3 and 4.4 for material properties and spring constants).

Architectural grade PVB is known to have an increased stiffness compared to automotive grade PVB, but information regarding material properties was not provided for either set of laminated specimens. Assuming the adhesion level did not increase for Group 2 specimens, a sensitivity analysis was performed and an updated energy velocity dispersion curve model was traced to determine how high the PVB interlayer stiffness would need to increase to match the experimental findings. Experimental energy velocity measurements for Group 2 specimens are compared to the updated dispersion model and laminate characteristics are discussed.

The resulting model requires a 20% increase in PVB stiffness to account for the shift in frequency of the energy velocity measurements. Updated material properties and resulting spring constants for the new model are displayed in Tables 4.5 and 4.6, respectively. Figure 4.26 displays the dispersion curve model from Group 1 (solid curves) in addition to the updated dispersion curve model with a 20% increase in PVB stiffness (dashed curves).

Table 4.5: Material properties and dimensions of laminated safety glass constituents in the updated dispersion model with a 20% increase in PVB stiffness for specimen Group 2.

	Thickness (mm)	Density (g/cm^3)	Young's Modulus (GPa)	Poisson's Ratio	Longitudinal Attenuation (Np/m)	Shear Attenuation (Np/m)
Float Glass	2.10	2.5	67	0.25	0	0
PVB	0.793	1.1	5.16	0.34	8.51	43.5

Table 4.6: Spring constants representing different levels of adhesion in the updated spring model with a 20% increase in PVB stiffness for specimen Group 2.

Pummel Number	Normal Spring Constant (N/m^3)	Transverse Spring Constant (N/m^3)
1*	3.2744 E+11	1.1468 E+10
3*	8.8970 E+11	3.1161 E+11
4*	1.1610 E+12	4.0664 E+11
5*	1.3942 E+12	4.8831 E+11
6*	1.9317 E+12	6.7655 E+11
8*	2.2003 E+12	7.7065 E+11
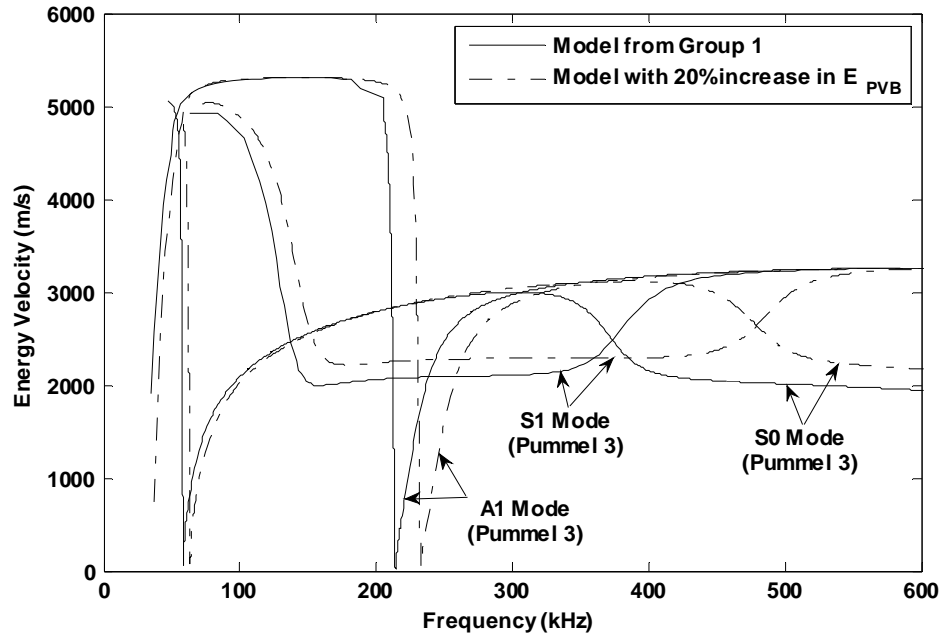
Figure 4.26: Revised dispersion curve model from specimen Group 1 (solid curves) and updated dispersion curve model with 20% increase in PVB stiffness for specimen Group 2 (dashed curves). Pummel number 3 spring constants were used for each specific model. (For material properties and spring constants, see Tables 4.3 and 4.4 for Group 1 model and Tables 4.5 and 4.6 for Group 2 model).

Experimental mean energy velocity measurements for laminated Specimen DD and updated dispersion curve model for Group 2 with increased PVB stiffness are displayed in Figure 4.27.
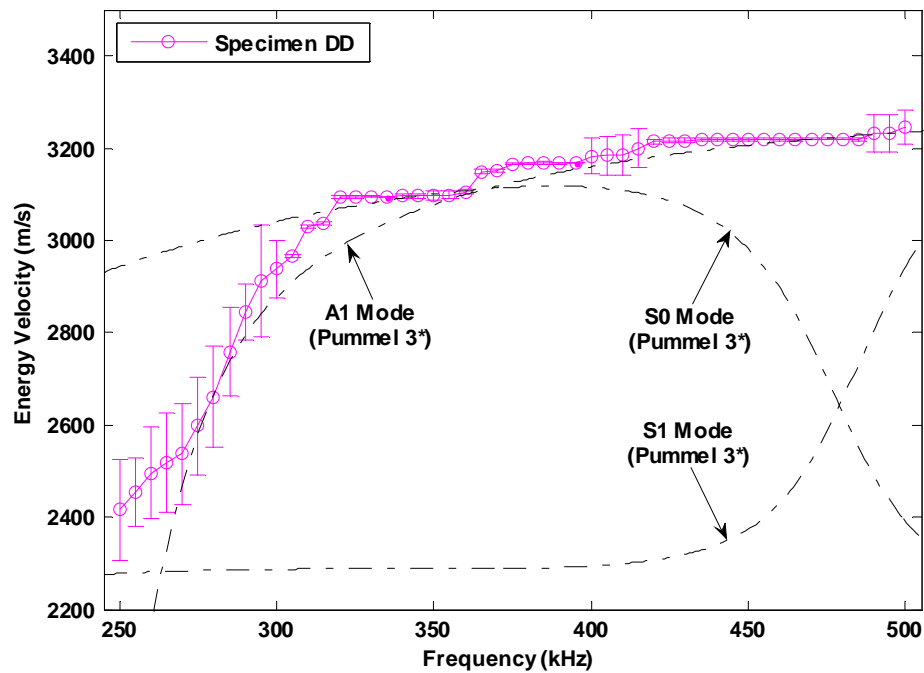
Figure 4.27: Experimental mean energy velocity measurements for laminated Specimen DD from specimen Group 2 superimposed with updated analytical dispersion curve model with 20% increase in PVB stiffness and corresponding pummel number 3* spring constants (See Tables 4.5 and 4.6 for material properties and spring constants). Error bars with 95% confidence are presented for each frequency.

79

Error bars representing two standard deviations (95% confidence) of five independent measurements are shown in Figure 4.27 for each frequency iteration. Energy velocity measurements exhibit nominal error at frequencies above 300 kHz. Greater error results at frequencies (< 300 kHz) where the A1 wave mode drops considerably in energy velocity. In this frequency range, the S0 and A1 wave modes interfere, and the resulting waveform is distorted by the superposition of the two partial waves.

The lamination process for architectural grade LSG requires fewer adhesion lowering salt additives than automotive grade laminates. Consequently, specimens in Group 2 were hypothesized to have increased levels of adhesion as a whole. Although the data from Group 2 specimens exhibits a noticeable shift toward higher frequencies, the adhesion level of the laminated specimens was very difficult to characterize definitively, as too many variables exist within the analytical models. Regardless, some significant findings are reported.

The energy velocity measurements on each specimen in this group produced very similar results. Therefore, the specimens in Group 2 are all believed to hold the same level of adhesion. The level of adhesion was more difficult to characterize for this group, as the stiffness of the PVB interlayer was increased by an unknown factor. Experimental results are presented with analytical dispersion curves for a 20% increase Young's modulus for the PVB interlayer, and the empirical data follows the new model reasonably well. A few conclusions can be made from this discovery. If the architectural grade PVB does in fact have a 20% increase in stiffness from the automotive grade PVB, the adhesion level of laminates from Group 1 and Group 2 is believed to be identical. On the contrary, if the architectural grade PVB has less than 20% increase in stiffness, a moderate increase in adhesion was observed. A 20% increase in stiffness seems somewhat large; therefore a slight increase in adhesive bond strength is estimated. Pummel tests were not performed on these laminates, giving minimal support to experimental findings. Although, the experimental results from Group 1 were encouraging and help uphold the conclusions made from Group 2 findings.

4.3   ATTENUATION MEASUREMENTS

In addition to energy velocity measurements, attenuation measurements were performed on both laminated specimen Groups. Details of lamination processing variables for each specimen in Groups 1 and 2 are presented in Tables 4.1 and 4.2, respectively. First, the analytical dispersion curve model developed in Section 4.2.2 is used to trace attenuation dispersion curves and select a wave mode for UT. Using a similar experimental setup as with energy velocity measurements, attenuation measurements are then performed, and attenuation coefficients are calculated for each laminated specimen. Correlations between measured attenuation coefficient measurements and those predicted by analytical dispersion curve models are discussed and adhesion levels are estimated for each laminated specimen.

4.3.1   ANALYTICAL ATTENUATION DISPERSION CURVE MODEL

In Chapter 3, the S2 wave mode was selected for UT, since significant energy loss occurs at a particular resonant frequency by pumping large amounts of energy into the attenuative PVB interlayer. Using the material properties and spring constants from Tables 4.3 and 4.4, respectively, attenuation dispersion curves of the S2 wave mode were traced for different pummel number models as seen in Figure 4.28.
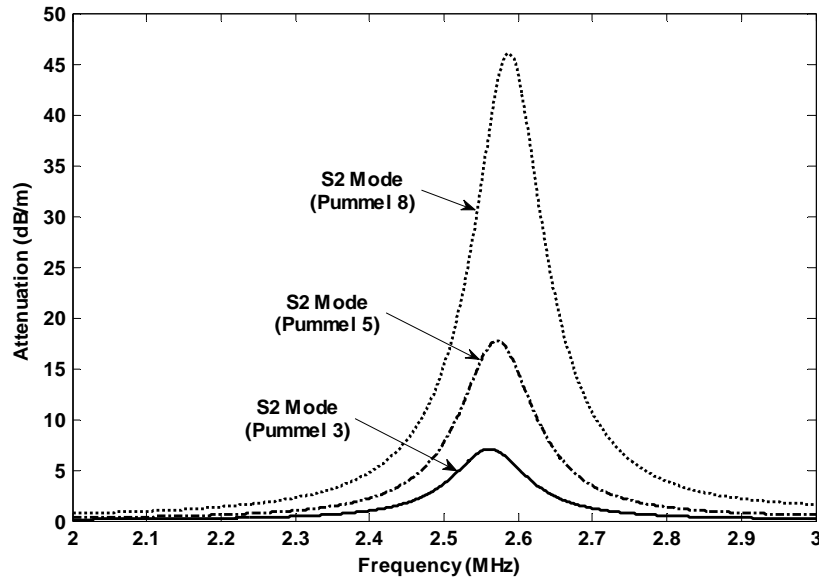
Figure 4.28: Attenuation dispersion curves of the S2 wave mode for pummel number 3 (solid curve), pummel number 5 (dashed curve) and pummel number 8 (dotted curve) models (See Tables 4.3 and 4.4 for material properties and spring constants).

81

Each model exhibits significant attenuation dominated by absorption in the PVB interlayer at a resonant frequency of approximately 2.55 MHz. Additional resonances exist at lower frequencies although less attenuation is attributed to absorption. Stiffer spring constants represent higher adhesion levels and therefore more contact exists at the interface of the glass and PVB layers. As a result, higher pummel number models experience greater attenuation since more energy is pumped into the PVB interlayer. The attenuation coefficients corresponding to dispersion curve models with pummel numbers 3, 5, and 8 are presented in Figure 4.29.
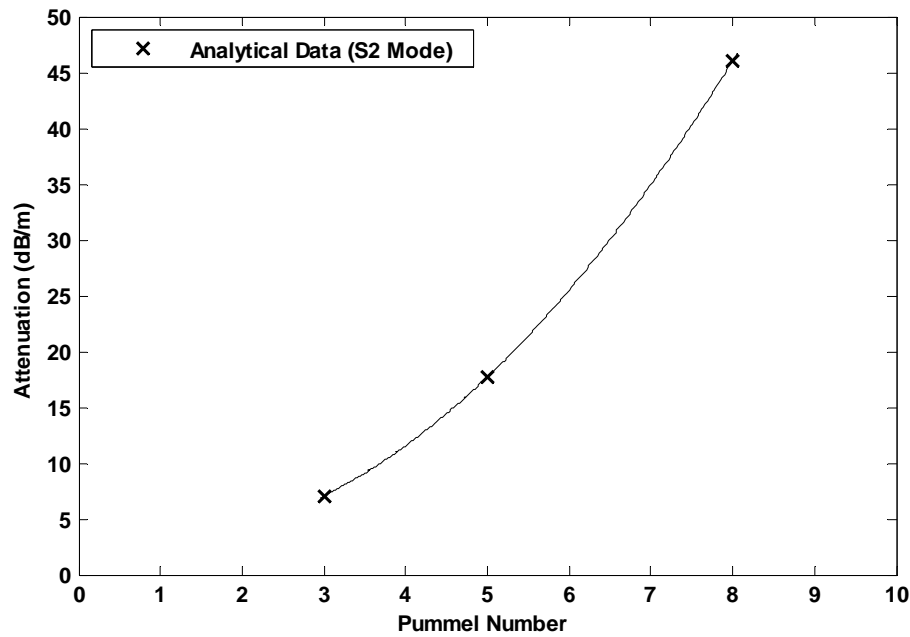
Figure 4.29: Expected attenuation coefficients extracted from analytical dispersion curve model for the S2 wave mode at 2.55 MHz with various pummel number spring constants (See Tables 4.3 and 4.4 for material properties and spring constants).

Although specimen Group 2 contains a higher PVB interlayer stiffness, the same attenuation dispersion model is assumed for both specimen groups, as several assumptions were made in the development of the analytical models. Laminates with an increase in PVB stiffness will have slightly higher resonant frequencies. Although, the excitation frequency used for experimental testing should excite these resonances. A fairly broad bandpass filter was applied to the output signal allowing slightly higher frequencies to be detected.

4.3.2   EXPERIMENTAL SETUP AND PROCEDURE

After reviewing the analytical dispersion model, the S2 wave mode with a resonant frequency of approximately 2.55 MHz was selected for UT attenuation measurements. The testing setup described for energy velocity measurements was used for attenuation measurements as well. Laminates were placed on a testing stand, and an indirect through transmission UT technique was utilized. The resonant frequency (peak) amplitude method in the time domain was employed for UT, where the attenuation coefficient was computed from the following equation,

$$\alpha = \frac{20}{L} \log \frac{A_o}{A_1} \quad \dots\dots\dots\dots\dots\dots\dots\dots\dots\dots\dots\dots\dots\dots\dots\dots\dots\dots\dots\dots\dots\dots(4.2)$$

A_o and A_1 are the amplitudes of reference and observed time signal waveforms, respectively, and L is defined as the difference between the reference and observed separation distances. The attenuation coefficient, α, is expressed in terms of Decibels/length. Details on ultrasonic attenuation measurements are provided in Appendix A. Two different separation distances between sending and receiving transducers were used for attenuation measurements. The first distance was set at 105 mm and was used to measure the reference wave amplitude. The observed wave amplitude was measured from a distance of 140 mm. Due to the moderately variable nature of UT attenuation measurements, ten independent measurements were taken (for each separation distance) on each laminate. A 50° angle of incidence was used to separate the S2 wave mode from additional partial waves. In order to stimulate the resonant frequency of the S2 wave mode, an excitation frequency of 2.55 MHz was used for each test. A 400 kHz Butterworth bandpass analog filter, centered about the excitation frequency, was applied to isolate the resonant frequency of the S2 wave mode. A sampling frequency of 50 MHz was used and 15,000 data points were collected for each measurement.

Figure 4.30 displays a typical normalized time signal for a reference and observed waveform. Peak amplitudes are labeled for each measurement. All resulting ultrasonic signals are normalized with respect to the maximum peak of the reference signal. Notice the observed waveform has a later arrival time and a reduction in amplitude. As a wave travels through a laminated specimen, energy is lost due to attenuation absorption in the PVB interlayer.
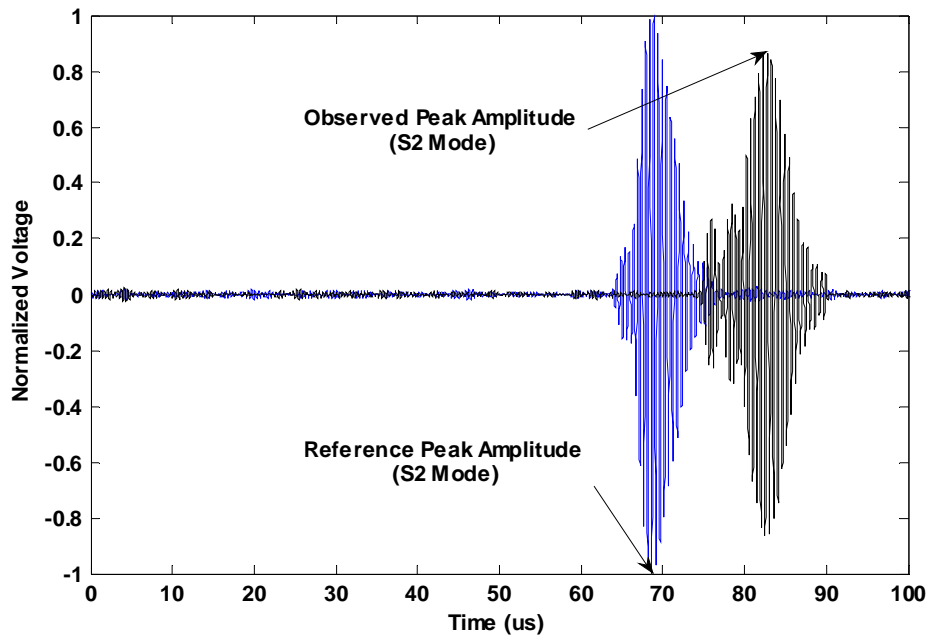
Figure 4.30: Typical normalized reference (blue waveform) and observed (black waveform) time signals used for attenuation measurements.

4.3.3   EXPERIMENTAL RESULTS

Ultrasonic waveforms were collected and attenuation coefficients were calculated for all laminates in specimen Groups 1 and 2. Experimental results are analyzed for each group and presented for discussion. The reference (blue waveform) and observed (black waveform) ultrasonic signals for Group 1 specimens are displayed in Figures 4.31 in the time and corresponding frequency domains. Ultrasonic signals are normalized with respect to the maximum peak of the reference waveform in both the time and frequency domain to illustrate more clearly the reductions in observed waveform amplitudes. Similar measurements were taken on Group 2 specimens, and resulting waveforms are displayed in Figure 4.32. The peak amplitudes of observed waveforms have noticeably attenuated for both specimen groups. Attenuation coefficients were calculated using Equation 4.2 for all laminated specimens. The experimental mean of ten independent attenuation coefficient measurements for each laminate are presented in Figures 4.33 and 4.34 for specimen Groups 1 and 2, respectively. Error bars corresponding to 90% confidence intervals are presented for each laminate as well.
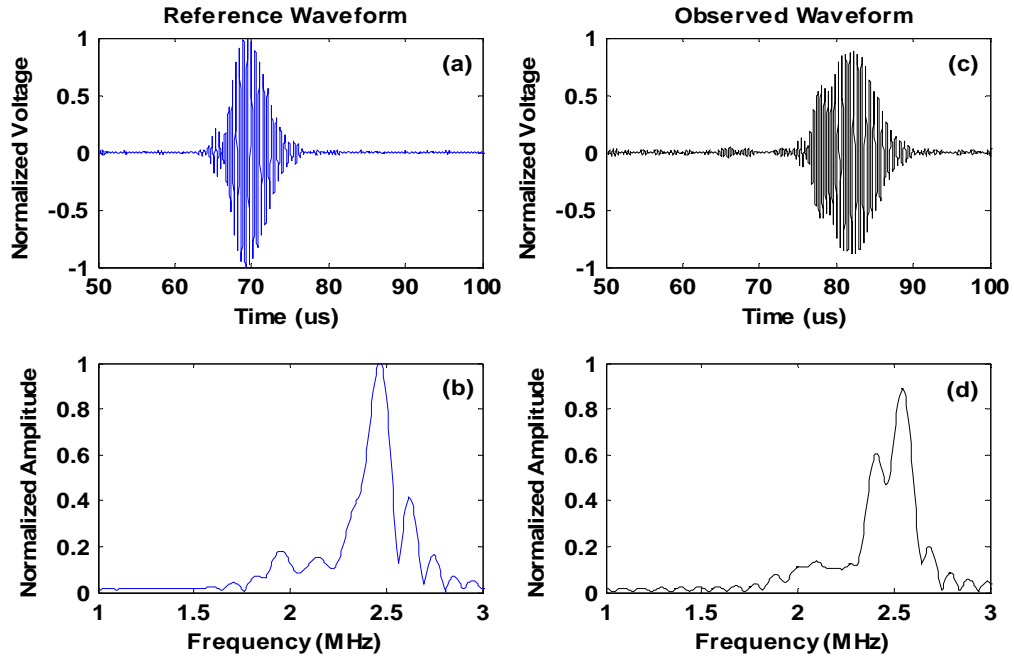
Figure 4.31: Resulting ultrasonic waveforms from Group 1 attenuation measurements: (a) reference time signal and corresponding (b) amplitude spectrum; (c) observed time signal and corresponding (d) amplitude spectrum.
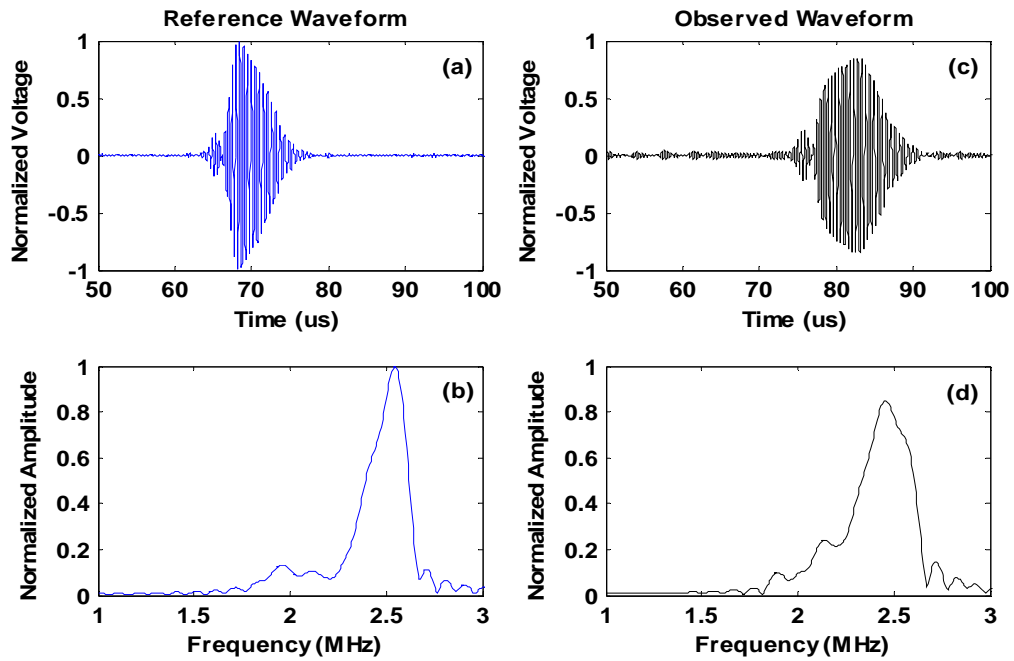
Figure 4.32: Resulting ultrasonic waveforms from Group 2 attenuation measurements: (a) reference time signal and corresponding (b) amplitude spectrum; (c) observed time signal and corresponding (d) amplitude spectrum.

85
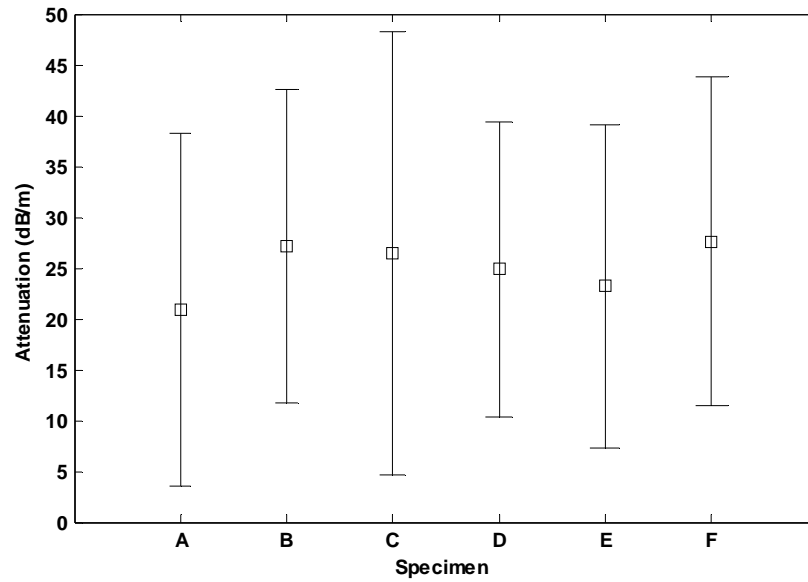
Figure 4.33: Experimental mean of ten independent attenuation coefficient measurements taken at 2.55 MHz with 90% confidence intervals for each laminate in specimen Group 1.
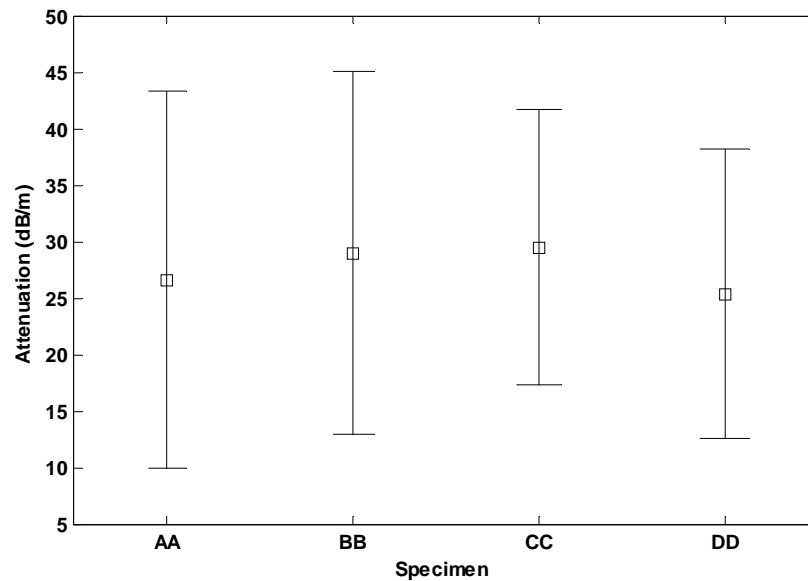
Figure 4.34: Experimental mean of ten independent attenuation coefficient measurements taken at 2.55 MHz with 90% confidence intervals for each laminate in specimen Group 2.

All laminated specimens from Group 1 show very similar experimental results with mean attenuation coefficients resulting between 21 -27 dB/m. Group 2 specimens exhibit slightly higher attenuation as a group with mean attenuation coefficients falling between 26 - 29 dB/m. Referring to Figure 4.29, all laminates in Group 1 correspond to approximately pummel number 5 – 6, while all laminates in Group 2 are somewhat higher, around pummel number 6.

Identical specimens from Group 1 were pummel tested to reveal actual adhesion levels of the laminated specimens. All laminates from Group 1 resulted in very low adhesion, between 1 and 2 pummel number. Experimental measurements support the conclusion that all laminates hold the same level of adhesion, but a fairly large overestimation in pummel number was observed. Overestimates in attenuation are believed to be related to additional sources of energy leakage and/or additional material absorption. The attenuation coefficients used in the analytical dispersion model were extracted from previous work, while the PVB interlayers used for LSG specimens in this study may have higher damping characteristics. As a result, the overall attenuation may be higher in reality. Additionally, a significant amount of error resulted between independent measurements for each laminate. Attenuation measurements are difficult to reproduce for the UT setup used in this study. First, the surface area of the Plexiglas wedges used to input oblique incident ultrasonic signals is very large. Consequently, consistent contact between the wedges and laminate surface was very difficult to control. Also, the ultrasonic wave path may have varied since the transducers (and wedges) may have been placed in slightly different locations for each independent test. In general, LSG specimens are assumed to have consistent adhesion throughout the laminate. Although with very low adhesion levels, the contact area between the glass and PVB layers is very sparse and regionally dispersed. Therefore, each measurement may have detected a different path with different adhesion characteristics.

Each laminate in specimen Group 2 revealed comparable results and exhibited slightly higher experimental attenuation coefficients than specimen Group 1. The increase in attenuation is believed to be attributed to an increase in laminate adhesion. Unfortunately, pummel tests were not performed on this set of laminates to confirm adhesion levels. Using specimen Group 1 experimental results as a reference, the pummel numbers predicted for specimen Group 2 are likely overestimated as well. In addition, considerable error between independent tests resulted from Group 2 measurements.

4.4   CONCLUSIONS

Guided wave behavior was investigated in LSG using analytical dispersion curve models and UT with the goal of characterizing the adhesive bond strength at the glass and PVB interface. Preliminary ultrasonic energy velocity measurements were performed to estimate material properties of glass and PVB constituents of the LSG specimens provided for UT. A revised analytical dispersion curve model was developed using the estimated material properties from initial energy velocity measurements. Energy velocity and attenuation dispersion curves were traced and used to compliment additional UT for the purpose of estimating adhesion levels in LSG specimens provided by Ceralink Inc..

Energy velocity measurements from laminates in experimental Groups 1 and 2 were compared with respective dispersion curve models. Adhesion levels for every specimen in Group 1 were estimated just under pummel number 3, while pummel tests revealed actual adhesion levels within the range of pummel number 1 to pummel number 2. All laminates in Group 2 are believed to hold identical adhesion levels, although the exact pummel number could not be determined definitively. Assuming that the lamination processing variables did contribute to significant differences in adhesion between specimen groups, laminates from Group 2 are believed to have slightly higher adhesion than Group 1 specimens.

Attenuation measurements in conjunction with analytical dispersion curve models shed some light on the estimation of adhesion levels in LSG. It was estimated that all laminates from specimen Group 1 contained adhesion levels between pummel number 5 and pummel number 6. Pummel tests were performed, and all specimens exhibited very low pummel numbers (between 1 and 2). Conclusions regarding similar adhesion as a group were supported, although the adhesion level was significantly overestimated. All specimens from Group 2 exhibited similar attenuation measurements as a group as well, and the adhesion level was approximated at pummel 6. Pummel tests were not performed, although a slight increase in adhesion was estimated. Overestimates in the adhesion level may be investigated with additional UT attenuation measurements on laminates with known material properties and an array of different adhesion levels. Subsequently, analytical dispersion curve models can be updated accordingly to

provide better estimates for attenuation coefficients. Current discrepancy is not likely attributed to poor estimate of attenuation coefficients for the PVB.

Overall, experimental energy velocity and attenuation measurements, complemented by analytical dispersion curve models, show potential for deciphering adhesion levels within LSG specimens. With sufficient information provided about laminate constituent properties and a group of specimens with a variety of adhesion levels, appropriate dispersion curve models could be traced and used to predict adhesion levels with greater confidence. Additional UT is recommended to help improve the analytical models presented in this thesis.

CHAPTER 5:

CONCLUDING REMARKS AND FUTURE WORK

Increased load bearing capacity, increased impact resistance, and reduced risk of injury make laminated safety glass (LSG) superior to monolithic glass. Since many major components are comprised of LSG (e.g. windshields, window panes, etc.), the significance in the automotive and architectural industries is unparalleled. It has been shown that impact resistance and delamination of glass shards post fracture are largely affected by the level of adhesion between the outer glass plates and copolymer interlayer. Surface characterization, a number of intermolecular interfacial forces, and various lamination processing variables all contribute to the complex nature of the adhesive bond in LSG. To date, an assortment of destructive testing methods have been employed to determine the strength of the adhesive bond, although no single test is generally used over the others. In recent years, more efficient adhesion monitoring methods have been investigated, using nondestructive testing (NDT) techniques.

In this study, experimental nondestructive ultrasonic testing (UT) was used in conjunction with analytical dispersion models to assess the integrity of a novel Fastfuse^{TM} RF lamination technology and to estimate the level of adhesion in automotive and architectural grade LSG specimens. An analytical sensitivity analysis was performed to observe the effect glass and PVB stiffness had on the guided wave behavior in LSG. Preliminary energy velocity measurements were compared to these models and were successful at determining the Rayleigh velocity of the LSG specimens. As a result, the stiffness of the plate glass layers was approximated at 67 GPa.

Revised dispersion curve models were constructed using updated material properties for glass and PVB. Additional ultrasonic energy velocity and attenuation measurements were performed and compared to revised dispersion curve models to help characterize the adhesive bond in LSG. The scope of results is limited, as all laminated specimens from both specimen groups tended toward lower adhesion levels. Additionally, knowledge of the laminate constituent material properties was incomplete, requiring a number of assumptions in the analytical models. It was encouraging to find that energy velocity and attenuation measurements predicted identical adhesion for all Group 1 specimens, which were then pummel tested and confirmed to hold similar (low) levels of adhesion.

It is likely the level of adhesion remained low in all specimens due to some deficient lamination processing variable. As noted in Chapter 1, the adhesion process for LSG is very complex and contains a number of variables that may reduce adhesion drastically if not performed precisely to specification. In addition, lamination processes are not fully standardized leaving a large amount of tacit knowledge throughout the LSG industry. The level of adhesion may be increased by altering a few lamination processing variables. Three essential processing parameters that control the adhesion level in LSG are pressure, heat and time. Although the novel Fastfuse[TM] RF lamination technology uses microwaves as opposed to conventional heating techniques to heat the PVB interlayer, the required amount of heat for proper lamination of high adhesion laminates is believed to be unchanged. Typical target lamination temperature and pressure have been reported in the range from 130 - 150 ^{o}C and 140 - 220 psi, respectively [1, 2, 33, 88]. The maximum lamination heat and pressure for any specimen from either experimental group reached approximately 150 ^{o}C and 100 psi, respectively. Therefore, the lamination temperature was sufficient, while the lamination pressure was much too low. Although adequate heat was provided to allow proper flow of the PVB interlayer, sufficient pressure was not applied in the lamination process to fill enough surface asperities permitting a strong chemical bond to form at the glass/PVB interface. The Fastfuse[TM] RF technology as a whole shows great potential for replacing conventional autoclaving lamination, once appropriate laminating parameters are discovered. Considerable time and energy could be saved using the new lamination technology.

Overall, UT using guided waves shows potential for adhesion level characterization in LSG. The experimental work presented in this thesis may be supplemented with additional UT on LSG specimens with higher adhesion levels. Further testing would allow a complete set of analytical dispersion models for various pummel numbers to be created, which could then be used to predict adhesion levels directly with UT. Once this method has been fine-tuned and developed further, it may be applied to more complicated LSG structures and geometry. Certain systems of interest may include LSG containing additional layers, LSG with different copolymer interlayers and LSG with curved surfaces.

APPENDIX A:
FUNDAMENTAL ULTRASONIC TESTING PRINCIPLES

Fundamental principles for nondestructive ultrasonic testing (UT) are described in this section for normal incident pulse-echo, direct normal incident through transmission and indirect oblique incident through transmission.

UT makes use of high frequency (20 kHz to 200 MHz) mechanical sound waves for material characterization without damaging the medium in any way [89]. Mechanical (acoustic) waves are generated using specialized transducers that contain an active element that converts electrical energy into mechanical energy (and vice versa) [90]. UT transducers contain polarized piezoelectric crystals, when submitted to alternate voltage, produce alternating strains, which initiates ultrasonic waves. Many other components exist within typical UT transducers as seen in Figure A.1. Two important components that help direct and constrain the active element are the backing and wear plate [89]. The backing is generally made of a highly attenuative material that reduces the mechanical vibration produced by the active element, directing most of the energy toward the wear plate and into the test specimen. The wear plate simply protects the active element and internal components of the transducer, and provides a smooth surface for optimal energy transmission (from active element to test specimen) [90].
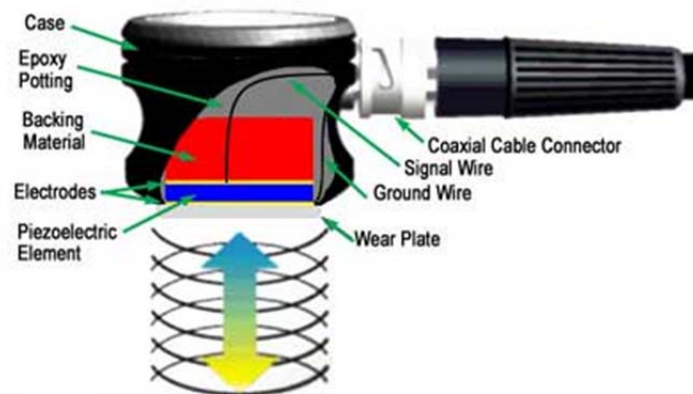
Figure A.1: Illustration of piezoelectric transducer components. Figure extracted from [69].

Depending on the application and the geometry of the testing specimen, different types of acoustic waves are utilized for UT such as longitudinal, shear, Rayleigh and lamb waves. Review Chapter 2 for details on acoustic wave propagation in solid media. In addition to various wave

types, two common testing setups are used for normal incident UT: pulse-echo and through transmission. Basic diagrams are presented in Figure A.2 for both pulse-echo and direct through transmission UT arrangements. For pulse-echo UT setup, one transducer is used to send and receive an ultrasonic signal, while through transmission uses one transducer to send a signal and one to receive the signal.

(a) Pulse-echo   **(b) Through Transmission**
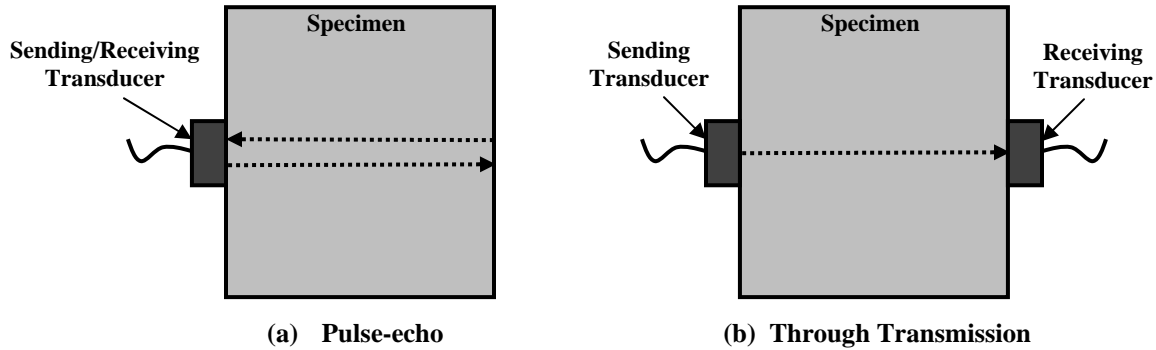
Figure A.2: Schematic diagram of typical normal incident UT setup for (a) pulse-echo and (b) through transmission.

In general, acoustic waves are generated with normal incidence for pulse-echo UT as seen in Figure A.2a. The transducer is fixed to a specimen with the wear plate parallel to the specimen surface using specialized ultrasonic couplant to ensure adequate transmission of acoustic wave energy [41]. Ultrasonic waves travel through the specimen and are reflected off the opposite side of the specimen and/or other inclusions or anomalies such as cracks or voids. The reflected signal is detected using the same transducer that sent the original signal. Specimen thickness and/or information regarding internal defects is collected and analyzed using two common principles: time of flight and signal amplitude [89]. The time of flight is measured directly as the time the sent signal takes to travel through the specimen and return. If the thickness of the specimen is known, the velocity of the material can be calculated from the following equation,

$$c = \frac{2d}{t} \dots\dots\dots\dots\dots\dots\dots\dots\dots\dots\dots\dots\dots\dots\dots\dots\dots\dots\dots\dots\dots\dots\dots\text{(A.1a)}$$

where d is the thickness of the specimen and t is the time the signal takes to travel to the opposite side of the specimen and back. Similarly, if the material velocity is known, the location of internal defects can be found by rewriting Equation A.1a in terms of d:

$$d = \frac{ct}{2} \dots\dots\dots\dots\dots\dots\dots\dots\dots\dots\dots\dots\dots\dots\dots\dots\dots\dots\dots\dots\dots\dots\dots\text{(A.1b)}$$

The through transmission UT technique is often utilized in highly attenuative materials where pulse-echo is less effective [91]. UT is performed similarly to pulse-echo, except an additional transducer is used to receive the signal on the opposite side of the specimen as seen in Figure A.2b. As a result, the velocity is calculated using only one trip through the specimen, which is shown by the following relation,

$$c = \frac{d}{t} \dots\dots\dots\dots\dots\dots\dots\dots\dots\dots\dots\dots\dots\dots\dots\dots\dots\dots\dots\dots\dots\dots (A.2)$$

where d is the separation distance between sending and receiving transducers and t is the arrival time of the ultrasonic wave packet.

Attenuation measurements can also be analyzed using either pulse-echo or through transmission arrangements by observing the relative change in amplitude from sent to received signals [92]. The attenuation is described in the following relation,

$$A_1 = A_o e^{-\alpha L} \dots\dots\dots\dots\dots\dots\dots\dots\dots\dots\dots\dots\dots\dots\dots\dots\dots\dots (A.3)$$

where A_o is a reference amplitude of an unattenuated wave at some location. After a wave has traveled a specified distance, the attenuated (observed) wave amplitude is given by A_1. The exponential function relates the attenuation coefficient, α, and the distance between the reference and observed waves, L, to the ratio of reference and observed wave amplitudes. Solving Equation A.3 for the attenuation coefficient, the following equations are used to describe energy loss due to absorption and leakage expressed in terms of Nepers/length and Decibels/length, respectively:

$$\alpha = \frac{1}{L} \ln \frac{A_o}{A_1} \dots\dots\dots\dots\dots\dots\dots\dots\dots\dots\dots\dots\dots\dots\dots\dots (A.4a)$$

and

$$\alpha = \frac{20}{L} \log \frac{A_o}{A_1} \dots\dots\dots\dots\dots\dots\dots\dots\dots\dots\dots\dots\dots\dots (A.4b)$$

An alternative indirect through transmission technique is often used in conjunction with oblique incidence UT. As seen in Figure A.3, both sending and receiving transducers are located on the same side of the specimen, and ultrasonic signals are sent and received at some specified oblique angle. Snell's law, which is covered in Appendix C, is often used to determine appropriate incident angles. This testing setup is beneficial when only one side of a specimen surface is available for UT and for defect characterization where normal beam UT is not effective [89].
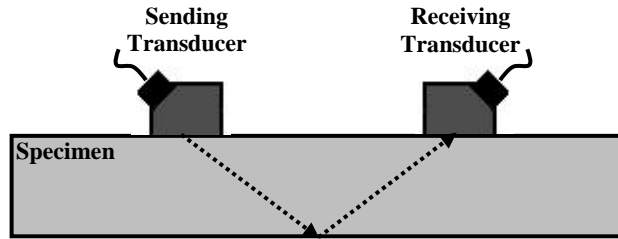
Figure A.3: Schematic diagram of typical oblique incident UT setup for through transmission.

For a more detailed analysis on UT principles, please see the following references [41, 89-93]. In addition, McGovern provides an extensive literature review of common ultrasonic velocity and attenuation techniques [39].

APPENDIX B:

POWER REGRESSION FOR ADDITIONAL SPRING CONSTANTS

Additional spring constants were approximated using a power regression curve fit to experimental data extracted from Huo [10]. Data for the normal and transverse (shear) spring constants with corresponding pummel numbers are presented in Figures B.1 and B.2, respectively. A power regression fit is plotted and used to estimate spring constants for pummel numbers not offered.
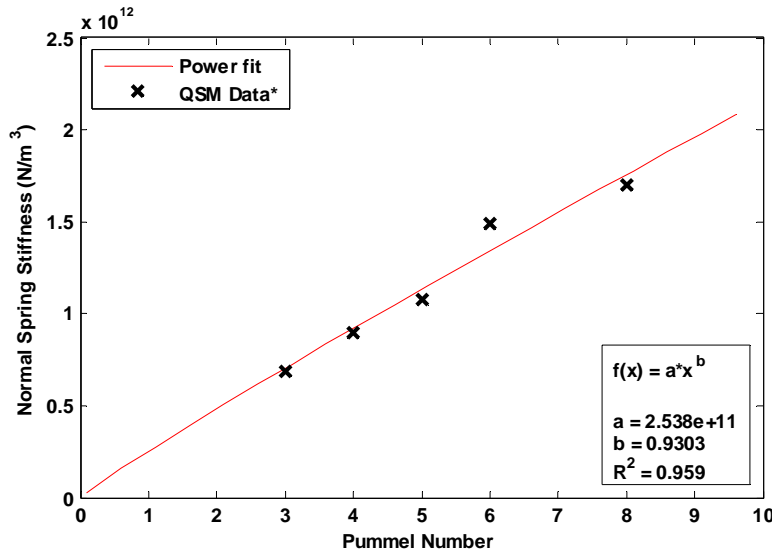
Figure B.1: Normal spring constants used for the QSM to simulate an adhesive layer between glass and PVB in laminated safety glass with different pummel numbers (spring constants extracted from [10]).
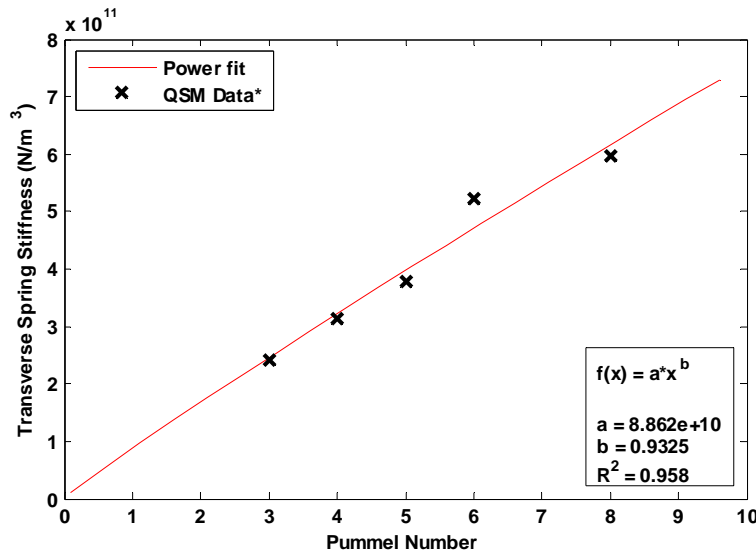
Figure B.2: Transverse spring constants used for the QSM to simulate an adhesive layer between glass and PVB in laminated safety glass with different pummel numbers (spring constants extracted from [10]).

APPENDIX C:

REVIEW OF SNELL'S LAW

Assuming continuity of pressure at a planar boundary between two materials with varying impedances, the transmitted energy from plane waves obliquely incident on the planar boundary refracts according to Snell's law,

$$\frac{\sin \theta_i}{c_1} = \frac{\sin \theta_t}{c_2}$$ ....(C.1)

where θ_i and θ_t correspond to the angle of incidence and angle of transmission, respectively [68]. The bulk velocities of material 1 and material 2 are denoted by c_1 and c_2, respectively. The relationship between incident and transmitted waves is depicted in Figure C1.
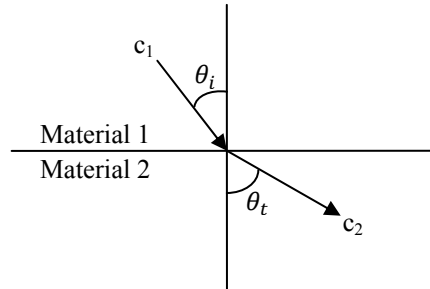
Figure C.1: Transmission of a plane wave obliquely incident on a planar boundary between two materials with different impedances.

When $c_1 < c_2$ and $\theta_i < \theta_t = 90^o$, a critical angle of incidence arises and the fastest wave mode will propagate along the surface boundary instead of transmitting energy into material 2. This occurrence is beneficial in ultrasonic testing when trying to eliminate specific wave modes. If the angle of incidence is increased further, additional wave modes will be terminated. See Graff for more details on Snell's law [70].

REFERENCES

1.   G.F. Savineau, "Fundamentals of Laminating Process and Quality Requirements," *Glass Processing Days,* pp.154-157, Sept. 13-15, 1997.

2.   D.P. Bourcier, F.A. Koran, J. Herbert, and L. Crommen. "Glass Lamination Process." U.S. Patent 7,704,342 B2. Nov. 15, 2002.

3.   T.A. Dear, "Acoustics for Glass and Laminates," *Glass Processing Days*, pp. 160-162, Sept. 13-15, 1997.

4.   U. Keller and H. Mortelmans, "Adhesion in Laminated Safety Glass – What Makes it Work?," *Glass Processing Days*, pp. 353-356, June 13-16, 1999.

5.   A.V. Duser, A. Jagota, and S.J. Bennison, "Analysis of Glass/Polyvinyl Butyral Laminates Subjected to Uniform Pressure," *Journal of Engineering Mechanics,* April, 1999, pp. 435-442.

6.   S.J. Bennison, C.A. Smith, A.V. Duser, and A. Jagota, "Strength of Laminated Safety Glass," *Glass Processing Days,* pp. 368-371, June 18-21, 2001.

7.   P.J. Scott and T. Hobson, "Foundations of Topological Characterization of Surface Texture," *International Journal of Machine Tools and Manufacture,* Vol. 38, No. 5-6, pp. 559-566, 1998.

8.   N. Tayebi and A.A. Polycarpou, "Adhesion and Contact Modeling and Experiments in Microelectromechanical Systems Including Roughness Effects," *Microsyst Technol,* Vol. 12, pp.854-869, 2006.

9.   M.R. Houston, R.T. Howe, and R. Maboudian, "Effect of Hydrogen Termination on the Work of Adhesion between Rough Polycrystalline Silicon Surfaces, " *J. Appl. Phys.,* Vol. 81, pp. 3474-3483, 1997.

10. S. Huo, "Estimation of Adhesive Bond Strength in Laminated Safety Glass Using Guided Mechanical Waves," Diss. University of Illinois at Urbana-Champaign, 2008. Print.

11. R.T. Nichols and R.M. Sowers, "Laminated Materials, Glass," *Kirk-Othmer Encyclopedia of Chemical Technology,* pp. 1-17, 2009.

12. G. Savineau and F. Serruys, "Durability and Postbreakage Behaviour of Laminated Safety Glass," *Glass Processing Days,* pp. 328-330, June 18-21, 2001.

13. G.E. DeJackome, "Moisture Induced Delaminations in Automotive Windscreens," *Glass Performance Days,* pp. 486-490, Sept. 13-15, 1997.

14. J.R. Huntsberger, "Adhesion of Plasticized Poly(vinyl Butyral) to Glass," *The Journal of Adhesion,* Vol. 13, No. 2, pp. 107-129, 1981.

15. R.D. Adams and B.W. Drinkwater, "Nondestructive Testing of Adhesively-Bonded Joints," *NDT&E International,* Vol. 20, No. 2, pp. 93-98, 1997.

16. T.P. Pialucha, "The Reflection Coefficient from Interface Layers in NDT of Adhesive Joints," Diss. University of Illinois at Urbana-Champaign, 1992. Print.

17. P. Cawley, "Ultrasonic Measurements for the Quantitative NDE of Adhesive Joints – Potential and Challenges," *IEEE: Ultrasonics Symposium,* pp. 767-772, 1992.

18. J.M. Allin, "Disbond Detection in Adhesive Joints Using Low-Frequency Ultrasound," Diss. University of London, 2002. *Dissertations and Theses.* Web. March 7, 2011.

19. S. Huo and H. Reis, "Estimation of Adhesive Bond Strength in Laminated Safety Glass Using Guided Mechanical Waves: Part 1. An Energy Velocity Approach," *INSIGHT,* Vol. 50, No. 3, pp. 146-152, 2008.

20. J. B. P. Williamson, "The Shape of Surfaces," *CRC Handbook of Lubrication,* E. R. Booser, Editor, Vol. 2, pp. 3-16, 1984.

21. W. Grzesik. *Advanced Machining Processes of Metallic Materials: Theory, Modeling and Applications.* Oxford, UK: Elsevier BV, 1st ed., 2008.

22. J. Lausmaa, B. Kasemo, and H. Mattsson, "Surface Spectroscopic Characterization of Titanium Implant Materials," *Applied Surface Science,* Vol. 44, pp. 133-146, 1990.

23. P. J. Caber, "Interferometric Profiler for Rough Surfaces," *Applied Optics,* Vol. 32, No. 19, pp. 3438-3441, July 01, 1993.

24. K. Miyoshi, "Surface Characterization Techniques: An Overview," *NASA TM-2002-211497,* July, 2002.

25. National Physical Laboratory. http://www.npl.co.uk/educate-explore/posters/length/

26. H. S. Jung, M.-S. Hong, S.-H Lee, J. H. Park, D. Kang, and M. G. Lee, "A Novel Stylus Profiler Without Nonlinearity and Parasitic Motion for FPD Inspection System," *Journal of Mechanical Science and Technology,* Vol. 21, No. 10, pp. 1491-1497, 2007.

27. M.A. Tshabalala. *Handbook of Wood Chemistry and Wood Composites.* Boca Raton, FL: CRC Press, pp. 187-211, 2005.

28. A.Y. Suh and A.A. Polycarpou, "Adhesive Contact Modeling for Sub-5-nm Ultralow Flying Magnetic Storage Head-Disk Interfaces Including Roughness Effects," *Journal of Applied Physics,* Vol. 97, No. 104328, pp. 1-11, 2005.

29. A.I. Lavrentyev and S.I. Rokhlin, "Ultrasonic Spectroscopy of Imperfect Contact Interfaces between a Layer and Two Solids," *J. Acoust. Soc. Am.,* Vol. 103, No. 2, pp. 657-663, Feb., 1998.

30.   H. Margenau, "Van der Waals Forces," *Reviews of Modern Physics,* Vol. 11, No. 1, pp. 1-35, Jan., 1939.

31.   J.C. Nugue, E. Nourry, and G. Sacineau, "Toughness, Resiliency and Adhesion of Polyvinylbutyral (PVB) Interlayers with Regards to Impact Resistance," *Glass Processing Days,* pp.437-440, 2003.

32.   B. Weller, J. Wünsch, and K. Härth, "Experimental Study on Different Interlayer Materials for Laminated Glass," *Glass Processing Days,* pp. 120-123, 2005.

33.   M. V. Russelt, "How to Make a Good Laminated Safety Glass for Windscreens," *Glass Processing Days,* Session 9, pp.475-479, Sept. 13-15, 1997.

34.   Ceralink, Inc. 2006-2010.

35.   F. Ensslen, "Influences of Laboratory and Natural Weathering on the Durability of Laminated Safety Glass," *Glass Performance Days,* pp. 584-590, 2007.

36.   A.I. Lavrentyev and S.I. Rokhlin, "Ultrasonic Study of Environmental Damage Initiation and Evolution in Adhesive Joints," *Res. Nondestr. Eval.,* Vol. 10, pp. 17-41, 1998.

37.   A. Jagota, S.J. Bennison, and C.A. Smith, "Analysis of a Compressive Shear Test for Adhesion between Elastomeric Polymers and Rigid Substrate," *International Journal of Fracture,* Vol. 104, pp. 105-130, 2000.

38.   Y. Sha, C.Y. Hui, E.J. Kramer, P.D. Garrett, and J.W. Knapczyk, "Analysis of Adhesion and Interface Debonding in Laminated Safety Glass," *J. Adhesion Sci. Technol.,* Vol. 11, No. 1, pp. 49-63, 1997.

39.   M. E. McGovern, "Assessment of Brown-Rot Decay Using X-Ray Computer Tomography and Ultrasonic Measurements," MS thesis University of Illinois at Urbana-Champaign, 2011. Print.

40.   H. Reis and A. Vary, "The Acousto-Ultrasonic Approach: Several Industry Applications," *World Forum on Smart Materials and Smart Structures Technology: Proc. SMSSST'07,* Ch. 201, pp. 22-27, May, 2007.

41.   J.L. Rose. *Ultrasonic Waves in Solid Media.* Cambridge, UK: Cambridge University Press, 1999. Print.

42.   D.N. Alleyne, "The Nondestructive Testing of Plates Using Ultrasonic Lamb Waves," Diss. University of London, 1991. *Dissertations and Theses.* Web. March 7, 2011.

43.   H.L.M. Reis, "Acousto-Ultrasonic Nondestructive Evaluation of Composite Flange Radii," *Technical Report, prepared for General Electric Aircraft Engines, Dec., 1990.*

44.   D.E. Chimenti, "Guided Waves in Plates and Their Use in Materials Characterization," *Appl. Mech. Rev.,* Vol. 50, No. 5, pp. 247-284, 1997.

45. A.I. Lavrentyev and S.I. Rokhlin, "Ultrasonic Spectroscopy of Imperfect Contact Interfaces between a Layer and Two Solids," *J. Acoust. Soc. Am.,* Vol. 103, No. 2, pp. 657-663, Feb., 1998.

46. H.G. Tattersall, "The Ultrasonic Pulse-Echo Technique as Applied to Adhesion Testing," *J. Phys. D: Appl. Phys.,* Vol. 6, pp. 819-831, 1973.

47. S.-C. Wooh and C. Wei, "A High-Fidelity Ultrasonic Pulse-Echo Scheme for Detecting Delaminations in Composite Laminates," *Composites,* Vol. 30, Part B, pp. 433-441, 1999.

48. A. Pilarski and J. L. Rose, "Ultrasonic Oblique Incidence for Improved Sensitivity in Interface Weakness Determination," *NDT International,* Vol. 21, No. 4, pp. 241-246, 1988.

49. A. Pilarski, J. L. Rose, and K. Balasubramian, "The Angular and Frequency Characteristics of Reflectivity from a Solid Layer Embedded Between Two Solids with Imperfect Boundary Conditions," *J. Acoust. Soc. Am.,* Vol. 87, No. 2, pp. 532-542, 1990.

50. S.I. Rokhlin and D. Marom, "Study of Adhesive Bonds Using Low-Frequency Obliquely Incident Ultrasonic Waves," *J. Acoust. Soc. Am.,* Vol. 80, No. 2, pp. 585-590, Aug., 1986.

51. K.J. Sun, "Application of Guided Acoustic Waves to Delamination Detection," *NASA NDTnet: 18th Review of Progress in Quantitative Nondestructive Evaluation,* Vol. 2, No. 3, pp. 1213-1219, 1991.

52. A. Pilarski and J.L. Rose, "Lamb Wave Mode Selection Concepts for Interfacial Weakness Analysis," *Journal of Nondestructive Evaluation,* Vol. 11, No. 3-4, pp. 237-249, 1992.

53. K. Vine, P. Cawley, and A.J. Kinloch, "Comparison of Normal and Oblique Incidence Ultrasonic Measurements for the Detection of Environmental Degradation of Adhesive Joints," *NDT&E International,* Vol. 35, pp.241-253, 2002.

54. M.J. Santos and P. Faia, "Propagation of Ultrasonic Lamb Waves in Aluminum Adhesively Bonded LAP Joints and in Single Plates," *Research in Nondestructive Evaluation,* Vol. 20, No. 3, pp. 178-191, 2009.

55. K. Heller, L.J. Jacobs, and J. Qu, "Characterization of Adhesive Bond Properties Using Lamb Waves," *NDT&E International,* Vol. 33, pp. 555-563, 2000.

56. T. Baenas, J. Ramis, J. Vera, and J. Alba, "Influence of the Polymeric Interlayer Shear Modulus in the Laminated Glass Panels Transmission Loss," *Glass Performance Days,* pp. 633-638, 2007.

57. R.F. Wegman and J.R. Mitchell, "Evaluation of Adhesive Bonds by Acousto-Ultrasonics," *The American Society for Nondestructive Testing, Inc., Second International Conference on Acousto-Ultrasonics,* pp.117-121, June 24-25, 1993.

58. H. Nayeb-Hashemi and J. N. Rossettos, "Nondestructive Evaluation of Adhesively Bonded Joints by Acousto-ultrasonic Techniques and Acoustic Emission," *The American Society for Nondestructive Testing, Inc., Second International Conference on Acousto-Ultrasonics,* pp. 203-233, June 24-25, 1993.

59. A. Fahr, Y. Youssef, and S. Tanary, "Adhesive Bond Evaluation Using Acousto-ultrasonics and Pattern Recognition Analysis," *The American Society for Nondestructive Testing, Inc., Second International Conference on Acousto-Ultrasonics,* pp. 235-254, June 24-25, 1993.

60. J. C. Duke Jr. and S. Karhnak, "Correlation of AU Evaluation and Acoustic Microscopy of Adhesively Bonded Joints," *The American Society for Nondestructive Testing, Inc., Second International Conference on Acousto-Ultrasonics,* pp. 255-272, June 24-25, 1993.

61. H.L.M. Reis and H.E. Krautz, "Nondestructive Evaluation of Adhesive Bond Strength Using the Stress Wave Factor Technique," *J. Acoustic Emission,* Vol. 5, No. 4, pp. 144-147, 1986.

62. A. Vary, "The Acousto-Ultrasonic Approach," *NASA and American Society for Nondestructive Testing,* Blacksburg, Virginia, July 12-15, 1987.

63. S. Hou and H. Reis, "Adhesive Bond Evaluation in Laminated Safety Glass Using Guided Wave Attenuation Measurements," *Advances in Ceramic Armor IV,* pp. 33-44, 2009.

64. D.J. David and T.N. Wittberg, "ESCA Studies of Laminated Safety Glass and Correlations with Measured Adhesive Forces," *The Journal of Adheison,* Vol. 17, No. 3, pp. 231-242, 1984.

65. M.J. Chica, "Nondestructive Evaluation of the Adhesive Bond Strength of Laminated Wood Finger Joints and Laminated Safety Glass," MS thesis University of Illinois at Urbana-Champaign, 1988. Print.

66. D.N. Slowinski, "Nondestructive Evaluation of the Adhesive Bond Strength in Laminated Safety Glass," MS thesis University of Illinois at Urbana-Champaign, 1989. Print.

67. H.L.M. Reis and M. Chung, "Nondestructive Evaluation/Identification of the Plastic Interlayer in Laminated Safety Glass," *Technical Report GE 98-01, prepared for Solutia, Inc.,* May, 1998.

68. L.E. Kinsler, A.R. Frey, A.B. Coppens, and J.V. Sanders. *Fundamentals of Acoustics, 4th edition.* Hoboken, NJ: John Wiley & Sons, Inc., 1976. Print.

69. NDT Education Resource Center, Brian Larson, Editor, The Collaboration for NDT Education, and Iowa State University, www.ndt-ed.org.

70. K.F. Graff. *Wave Motion in Elastic Solids.* Mineola, NY: Dover Publications, Inc., 1975.

71.   J.L. Borgerson, "Monitoring Early Age Cementitious Materials Using Ultrasonic Guided Waves," Diss. University of Illinois at Urbana-Champaign, 2007. Print.

72.   A.D. Pierce. *Acoustics: An Introduction to its Physical Principles and Applications*. Woodbury, NY: Acoustical Society of America, 1989. Print.

73.   F. Simonetti, "Sound Propagation in Lossless Waveguides Coated with Attenuative Materials," Diss. University of Illinois at Urbana-Champaign, 2003. Print.

74.   V. Dayal and V.K. Kinra, "Leaky Lamb Waves in an Anisotropic Plate. I: An Exact Solution and Experiments," *J. Acoust. Soc. Am.,* Vol. 85, No. 6, pp. 2268-2276, June, 1989.

75.   H. Lamb, "On Waves in an Elastic Plate," *Proc. R. Soc. A,* Vol. 93, No. 648, pp. 114-128, March, 1917.

76.   A. Bernard and M.J.S. Lowe, "Guided Waves Energy Velocity in Absorbing and Non-Absorbing Plates," *J. Acoust. Soc. Am.,* Vol. 110, No. 1, pp. 186-196, July, 2001.

77.   V. Pagneux and A. Maurel, "Lamb Wave Propagation in Elastic Waveguides with Variable Thickness," *Proc. R. Soc. A,* Vol. 462, pp. 1315-1339, 2006.

78.   B.L. Ervin, "Monitoring of Rebar Embedded in Mortar Using Guided Ultrasonic Waves," Diss. University of Illinois at Urbana-Champaign, 2007. Print

79.   R. Stonely, "Elastic Waves at the Surfaces of Separation of Two Solids," *Proc. R. Soc.*, Vol. A106, pp. 416-428, 1924.

80.   Lamit Company. Copyright 2004-2010.

81.   B. Pavlakovic and M.J.S. Lowe, *Disperse User's Manual*. Imperial College, University of London, 2001.

82.   L. Knopoff, "A Matrix Method for Elastic Wave Problems," *Bulletin of the Seismological Society of America,* Vol. 54, No. 1, pp. 431-438, Feb., 1964.

83.   M.J. Randall, "Fast Programs for Layered Half-Space Problems," *Bulletin of the Seismological Society of America,* Vol. 57, No. 6, pp. 1299-1315, Dec., 1967.

84.   H. Schmidt and F.B. Jensen, "A Full Wave Solution for Propagation in Multilayered Viscoelastic Media with Application to Gaussian Beam Reflection at Fluid-Solid Interfaces," *J. Acoust. Soc. Am.,* Vol. 77, No. 3, pp. 813-825, March, 1985.

85.   J. Baik and R.B. Thompson, "Ultrasonic Scattering from Imperfect Interfaces: A Quasi-Static Model," *Journal of Nondestructive Evaluation,* Vol. 4, No. 3-4, pp. 177-196, 1984.

86.   D.N. Alleyne and P. Cawley, "Optimization of Lamb Wave Inspection Techniques," *NDT & E International,* Vol. 25, No. 1, pp. 11-22, 1992.

87. P.-C. Xu and S.K. Datta, "Guided Waves in a Bonded Plate: A Parametric Study," *J. Appl. Phys.,* Vol. 67, No. 11, pp. 6779-6786, June 1, 1990.

88. J.R. Moran. "No Autoclave Process for Forming a Safety Glass Laminate." U.S. Patent 5,536,347. Sept. 22, 1994.

89. D. E. Bray and R. K. Stanley. *Nondestructive Evaluation: A Tool in Design, Manufacturing, and Service.* Revised ed. CRC Press. Inc., Boca Raton, Florida, 1997. Print.

90. Ultrasonic Transducer Technical Notes, *Olympus NDT: www.olympusNDT.com,* 2006.

91. D. Birchon,[revised] R. Halmshaw. *Non-Destructive Testing for Engineering Design.* Northampton, UK: The British Institute of Non-Destructive Testing, 1988.

92. J. Krautkrämer and H. Krautkrämer. *Ultrasonic Testing of Materials.* 3rd ed. Springer-Verlag, University of California, 1983. Print.

93. J. Szilard. *Physical Principles of Ultrasonic Testing.* In: Ultrasonic Testing: Non-conventional Testing Techniques. Chichester, Sussex, England and New York, Wiley-Interscience, pp. 1-23, 1982.